A new apparatus to simulate fundamental interactions with ultracold atoms

Giacomo Colzi

PhD Thesis submitted to the
Dipartimento di Fisica
Università degli Studi di Trento

In fulfilment of the requirements for the Degree of
Philosophiæ Doctor in Physics

Under the Supervision of
Dr. Gabriele Ferrari
Dr. Giacomo Lamporesi

Dottorato di Ricerca XXX Ciclo
April 20th, 2018

PhD Supervisor:

Dr. Gabriele Ferrari

PhD Co-supervisor:

Dr. Giacomo Lamporesi

Members of the Committee:

Dr. Thomas Bourdel

Prof. Leonardo Fallani

Prof. Leonardo Ricci

Contents

***

Thesis Abstract

***

In this thesis I present the construction of a new apparatus aimed at studying two-component Bose-Einstein condensates (BECs) in the presence of a Rabi coupling, where the two-components correspond to internal states of sodium atoms. The coherent mixture, in the miscible regime, also exhibits a metastable excitation consisting in a domain wall of relative phase connecting vortices of different components. Due to the peculiar energy dependence of such a configuration, an attractive force, independent of the vortex distance, is expected, making this system a candidate for mimicking features of quark confinement in QCD. The surface tension of the domain wall structure can be experimentally controlled via the strength of the coupling, allowing to study the system dynamics in different regimes. These include a predicted regime in which, for sufficient high coupling strength, the domain wall breaks and new vortex couples nucleate, providing by itself an interesting experimental realization of spin counterflow dynamical instabilities in a superfluid system, as well as a phenomenon analogous to string breaking in QCD. The choice of sodium as atomic species is motivated by its collisional properties that allow to obtain a perfect spatial superposition between the two miscible components $|F = \pm 1\rangle$ if trapped by a spin-independent potential, avoiding the known phenomenon of 'buoyancy'.

Studying the dynamics of such systems for sufficiently long times, with a mixture subject to Zeeman differential energy shifts, requires a specific effort to remove magnetic field fluctuations: a rough estimate suggests that in order to maintain the system coherence for a sufficiently long time to study its dynamics, magnetic field fluctuations should be reduced by at least three orders of magnitude compared to typical values observed in laboratory environment. Such attenuations can be obtained by means of multiple layers of µ-metal, that is incompatible with the use of ordinary magnetic traps, characterized by large magnetic field gradients on the atoms, due to residual magnetization and saturation of the shielding material. To avoid such effects it is required to either evaporatively cool atoms into an optical dipole trap loaded from a molasses stage, or a hybrid approach by means of which atoms are transferred to a low-gradient quadrupole trap superimposed to the optical trap.

Producing BECs with such protocols greatly benefits from an efficient optical molasses cooling stage to prepare the sample in the best conditions of temperature and density before loading atoms into the trap. With this regard, the main limitation of ordinary laser cooling techniques is their reliance on absorption and spontaneous

emission cycles, which limits the lowest temperature and highest density that can be reached as a consequence of residual heating effects and photon-reabsorption. An important resource to cope with these limits are dark states. In a broader sense a dark state is a state which does not interact with the exciting light field, and an atom in such a state would be neither subject to the beneficial cooling effects nor to the detrimental effects of light scattering. It is possible, however, to exploit the phenomenon of electromagnetically induced transparency (EIT) to induce a velocity-selective cooling mechanism for which slower atoms, that do not need further cooling, are trapped in a dark state corresponding to a coherent superposition of atomic levels whose excitation probabilities interfere destructively, while the cooling mechanism still applies to the fastest atoms. Among these techniques, gray molasses cooling allows to reach temperatures as low as a few recoil temperatures, while retaining atomic densities useful to reach quantum degeneracy in the subsequent stages of the experiment. In order to exploit this technique, an additional laser source had to be implemented during my thesis. To realize a gray molasses on the sample only $|F\rangle \rightarrow |F-1\rangle$ or $|F\rangle \rightarrow |F\rangle$ transitions can be chosen, requiring blue-detuned laser, in contrast to ordinary (sub)Doppler laser cooling techniques. Both these requirements rule out the use of the D2 transition ($3^2S_{1/2} \rightarrow 3^2P_{3/2}$ at 589 nm) used for ordinary laser cooling techniques, due to its finely-spaced hyperfine structure. On the other hand, the D1 transition ($3^2S_{1/2} \rightarrow 3^2P_{1/2}$ 590 nm) is characterized by a broader level spacing in the hyperfine structure and the absence of higher energy states on the blue side of the $|F_\mathrm{g}=2\rangle \rightarrow |F_\mathrm{e}=2\rangle$ transition. As part of the work for this thesis, I successfully implemented and characterized gray molasses cooling on the D1 optical line of sodium.

The buildup of the new apparatus includes the assembly of a new laser source for laser trapping and cooling on the D2 line, the assembly of the optical table devoted to the frequency and amplitude control of all the laser beams involved in the optical laser cooling procedures as well as the electronic control system. Design and assembly of the UHV and baking procedures for the stainless steel vacuum chamber are also described as well as the laser cooling techniques employed to load the atoms in a Dark-Spot MOT.

Regarding the production of BEC, various strategies were attempted for different dipole beam configurations. Dipole traps typically suffer from the tradeoff between capture volume and trap depth at a given power, while hybrid traps usually take advantage of a magnetic trap stage that would not be compatible with the µ-metal shielding. Preliminary attempts to reach quantum degeneracy after directly loading the dipole trap from molasses were unsuccessful due to spurious effects. An alternative approach based on a magnetic-shield compatible hybrid trap protocol, in the absence of magnetic trap compression, was successfully implemented.

The thesis is structured as follows:

- In the first introductory Chapter, I discuss the main topic to be addressed in the experimental apparatus that I assembled, that is the dynamics of defects in the experimentally unexplored regime involving Rabi-coupled BEC mixture. In particular, I underline the favorable interaction and response properties of the sodium mixture involving the $|F, m_\mathrm{F}\rangle$ states $|1, \pm 1\rangle$, in the context of defect

dynamics in multicomponent condensates. After, I discuss the effect of an additional Rabi coupling between the states composing the mixture, for which exotic defect structures emerge.

- In the second Chapter I describe the buildup of the experimental apparatus, including the vacuum chamber, the electronic control system, the laser sources for atom cooling and trapping, as well as the experimental means to produce controlled magnetic fields. Particular relevance is given to design strategies aimed to the reduction of magnetic field perturbations on the atoms. The Chapter is concluded by the experimental characterization of the atom source and the magneto-optical trap loading.

- In the third chapter I describe the implementation and characterization in sodium atoms of gray molasses cooling

- In the fourth chapter I describe the novel protocol that allowed the production of quantum-degenerate samples and fulfilling the constraints of the magnetic-shield. In particular, I give a general description of the attempted protocols to load atoms directly into an optical dipole from gray molasses, discussing the motivation that led to the choice of a hybrid trap protocol. Then I describe the calibration of the trapping potential and the optimization steps, before characterizing the optimized sequence.

- In the fifth chapter I summarize the results obtained and discuss the perspectives opened by my work

Chapter 1

Introduction

***

In this chapter I discuss the main properties of the binary Bose-Condensed mixture involving two Rabi-coupled internal states of sodium, giving particular relevance to the study of defect dynamics in this regime. During the chapter I underline the analogies that can be drawn between such a system and fundamental interactions, and account for the specific advantages related with the particular choice of mixture. In the first section, I focus on binary mixtures in the absence of coherent coupling, underlining the specific interaction properties exhibited by sodium. In the same section I also discuss the results concerning the linear response properties of such a mixture that we accomplished on another experimental apparatus similar to the one described in Chapter 2, during the buildup of the new apparatus, confirming the expected behavior of the mixture in terms of stability and enhanced magnetic susceptibility. The section is concluded with an overview on important experimental results, reported in literature, concerning the dynamics of defects in binary mixtures underlining the role of inter-component interactions in the enrichment of the observed phenomena. In the last section I move to the main focus for the experiment I assembled, i.e. discussing the effect of an additional coherent coupling between the states composing the mixture. In particular, the additional phase-dependent coupling between the mixture components

introduces novel and exotic defect configurations, whose dynamics is predicted to show interesting analogies with quark-confinement in QCD.

1.1 Two-component mixtures

In nature, there are many examples of systems which exhibit intricate macroscopic characteristics and exotic defect structures emerging from the interplay between quantum coherence and nontrivial internal degrees of freedom. Examples of this kind of systems include superfluid ^{3}He [1], unconventional superconductors [2, 3], quantum Hall systems [4] and Josephson Junctions [5]. In this respect, multicomponent degenerate quantum gases provide an easily accessible and controllable class of systems for the investigation of unconventional topological defects [6]. While it is impossible for heteronuclear mixtures, mixtures made of two spin states of a given atom can give us the possibility to coherently couple the two components. Spinor condensates, where the atoms occupy an entire hyperfine F manifold, are of particular interest to produce intricate topological defects [7–10]. While N-components mixtures can always be described by a fictitious $(N-1)/2$ components pseudo-spinor system, they do not posses the rotational symmetry in spin space and may lack some internal dynamics phenomena, which are present spinor condensates [11].

Not all the mixtures of individually-stable elements are experimentally accessible as a consequence of collisional incompatibility. As the number of components increases, so increases the number of possible loss mechanisms connected to the presence of new collisional channels. Mixtures of quantum-degenerate components produced in experiments include different elements and isotopes, eventually giving access to different quantum statistics (see for instance [12–16]), different internal states of the same hyperfine manifold in Rb [17–19], Na [20, 21] and K [22, 23]. Mixtures of Rb, involving both ground state manifolds were also studied [24–28].

1.1.1 Mean-field description

The mean-field description of a two-component Bose-Einstein condensate at zero temperature follows from a simple generalization of the single component case (see for instance [29]). The two-component many-body Hamiltonian, assuming equal masses for the two components $m_\mathrm{a} = m_\mathrm{b} = m$, in second-quantized form is

$$\hat{\mathcal{H}} = \sum_{i=a,b} \int \mathrm{d}\mathbf{x} \hat{\Psi}_\mathrm{i}^\dagger(\mathbf{x},t) \left[-\frac{\hbar^2}{2m}\nabla^2 + V_\mathrm{i}(\mathbf{x}) \right] \hat{\Psi}_\mathrm{i}(\mathbf{x},t) + \\ + \frac{1}{2} \sum_{i,j=a,b} \int \mathrm{d}\mathbf{x}\mathrm{d}\mathbf{x}' \hat{\Psi}_\mathrm{i}^\dagger(\mathbf{x},t) \hat{\Psi}_\mathrm{j}^\dagger(\mathbf{x}',t) V_\mathrm{int}(|\mathbf{x}-\mathbf{x}'|) \hat{\Psi}_\mathrm{j}(\mathbf{x}',t) \hat{\Psi}_\mathrm{i}(\mathbf{x},t), \quad (1.1)$$

where V_i is an external potential, that in principle can be different for each component. In the hypothesis of diluteness of the gas ($nr_0^3 \ll 1$, where r_0 designates the interatomic potential range and n the density), the effect of quantum depletion is negligible, and the second-quantized field operators describing the condensate can be approximated

through the Bogoliubov prescription, as complex scalars

$$\Psi_{\mathrm{i}}(\mathbf{x}) = \sqrt{n_{\mathrm{i}}(\mathbf{x})}e^{i\phi_{\mathrm{i}}(\mathbf{x})}. \tag{1.2}$$

The order parameter $\Psi_{\mathrm{i}}(\mathbf{x})$ is readily interpretable, in phenomenological terms, as the macroscopic wavefunction of the condensate in the i-th component, being proportional in squared modulus to the density $n_{\mathrm{i}}(\mathbf{x})$. Spatial variations of the phase $\phi_{\mathrm{i}}(\mathbf{x})$ are related to the presence of currents

$$\mathbf{v}_{\mathrm{i}} = \frac{\hbar}{m}\nabla\phi_{\mathrm{i}}(\mathbf{x}), \tag{1.3}$$

and are of fundamental importance in the description of defects in this kind of systems. For the given hypotheses of diluteness and low-energy collisions, and in the absence of long-range interactions (e.g. dipolar interactions), the interatomic interaction potential can be approximated as:

$$V_{\mathrm{ij}}(|\mathbf{x}_1 - \mathbf{x}_2|) = g_{\mathrm{ij}}\delta(\mathbf{x}_1 - \mathbf{x}_2), \tag{1.4}$$

where the i, j subscripts refer to the different atomic species or internal states composing the mixtures, labeled a and b. The interaction parameters g_{ij} can be expressed in terms of the s-wave scattering lengths

$$g_{\mathrm{ij}} = \frac{4\pi\hbar^2 a_{\mathrm{ij}}}{m}. \tag{1.5}$$

The binary mixture is then described by the energy functional

$$E = \sum_{i=a,b}\int \mathrm{d}\mathbf{x}\left[\frac{\hbar^2}{2m}\left|\nabla\Psi_{\mathrm{i}}\right|^2 + V_{\mathrm{i}}\left|\Psi_{\mathrm{i}}\right|^2\right] + \frac{1}{2}\sum_{i,j=a,b}\int \mathrm{d}\mathbf{x} g_{\mathrm{ij}}\left|\Psi_{\mathrm{i}}\right|^2\left|\Psi_{\mathrm{j}}\right|^2. \tag{1.6}$$

Note that this energy functional, valid in the absence of coherent coupling, does not account for coupling effects between current fields, which lead to phenomena such as the Andreev-Bashkin effect [30, 31]. By applying the variational principle $i\hbar\partial_{\mathrm{t}}\Psi_{\mathrm{i}} = \delta E/\delta\Psi_{\mathrm{i}}^*$ to (1.6), the coupled *Gross-Pitaevskii Equations* (GPEs) determining the system dynamics are obtained:

$$\begin{aligned} i\hbar\frac{\partial}{\partial t}\Psi_{\mathrm{a}}(\mathbf{x},t) &= \left(-\frac{\hbar^2}{2m}\nabla^2 + V_{\mathrm{a}}(\mathbf{x}) + g_{\mathrm{aa}}\left|\Psi_{\mathrm{a}}\right|^2 + g_{\mathrm{ab}}\left|\Psi_{\mathrm{b}}\right|^2\right)\Psi_{\mathrm{a}}(\mathbf{x},t). \\ i\hbar\frac{\partial}{\partial t}\Psi_{\mathrm{b}}(\mathbf{x},t) &= \left(-\frac{\hbar^2}{2m}\nabla^2 + V_{\mathrm{b}}(\mathbf{x}) + g_{\mathrm{ab}}\left|\Psi_{\mathrm{a}}\right|^2 + g_{\mathrm{bb}}\left|\Psi_{\mathrm{b}}\right|^2\right)\Psi_{\mathrm{b}}(\mathbf{x},t), \end{aligned} \tag{1.7}$$

that can be cast in the time-independent form in the same way as the single component case

$$\Psi_{\mathrm{i}}(\mathbf{x},t) = \Psi_{\mathrm{i}}(\mathbf{x})\exp\left[-i\frac{\mu_{\mathrm{i}}}{\hbar}t\right], \tag{1.8}$$

where μ_i is the chemical potential fixed by the normalization condition for each component $N_\mathrm{i} = \int \mathrm{d}\mathbf{x}\, |\Psi_\mathrm{i}(\mathbf{x})|^2$.

$$\begin{aligned}
\mu_\mathrm{a}\Psi_\mathrm{a}(\mathbf{x},t) &= \left(-\frac{\hbar^2}{2m}\nabla^2 + V_\mathrm{a}(\mathbf{x}) + g_\mathrm{aa}\,|\Psi_\mathrm{a}|^2 + g_\mathrm{ab}\,|\Psi_\mathrm{b}|^2\right)\Psi_\mathrm{a}(\mathbf{x},t). \\
\mu_\mathrm{b}\Psi_\mathrm{b}(\mathbf{x},t) &= \left(-\frac{\hbar^2}{2m}\nabla^2 + V_\mathrm{b}(\mathbf{x}) + g_\mathrm{ab}\,|\Psi_\mathrm{a}|^2 + g_\mathrm{bb}\,|\Psi_\mathrm{b}|^2\right)\Psi_\mathrm{b}(\mathbf{x},t),
\end{aligned} \tag{1.9}$$

While the mean-field description of the binary mixture appears as a simple extension of the single component case, the addition of the second component enriches the system with new features. Only in the particular limit $g_\mathrm{ab} = 0$, the two equations (1.7) decouple, and the system behaves as an overlap of two independent condensates. In general, for $g_\mathrm{ab} \neq 0$, the two components exhibit mutual mean field interactions which affects both the static (ground state) and the dynamic (sound and collective excitation) properties of the system, as explained in the following. Since the interaction energy depends only on the densities, it brings no information on the relative phase between the components. Terms depending on the relative phase emerge in the presence of coherent coupling, as is discussed subsection 1.2.

1.1.2 Static and dynamic properties

Interactions play a decisive role in defining the ground state of the mixture. The stability of the binary system requires to have both intra-component interactions repulsive ($g_\mathrm{ii} > 0$), while g_ab can assume negative values, to a certain extent. Depending on the interplay between different interaction terms, the system arranges either in a mixed state or in a phase-separated configuration. If repulsive inter-component interactions (g_ab) overcome, then the system reduces the associated energy by separating the two components in distinct domains. In the opposite case they overlap, each occupying all the available volume. A quantitative miscibility criterion can be easily established for a homogeneous system, from the energy functional (1.6), neglecting the kinetic energy term [29]:

$$|g_\mathrm{ab}| < \sqrt{g_\mathrm{a} g_\mathrm{b}}, \tag{1.10}$$

where the absolute value on the left hand side of the inequality forces a lower bound for negative (attractive) interspecies interaction parameters, ensuring the stability of the mixture against collapse [32]. If such a condition is fulfilled, the system is miscible.

In the presence of a trapping potential, the system behavior is less trivial, and the miscibility criterion does not fully account for the system properties [33]. Evaluating the density profiles requires, in this case, to solve the stationary coupled GPEs (1.9). An analytical solution can be easily found if the interaction energy dominates over the system kinetic energy (Thomas-Fermi approximation). For a state-independent

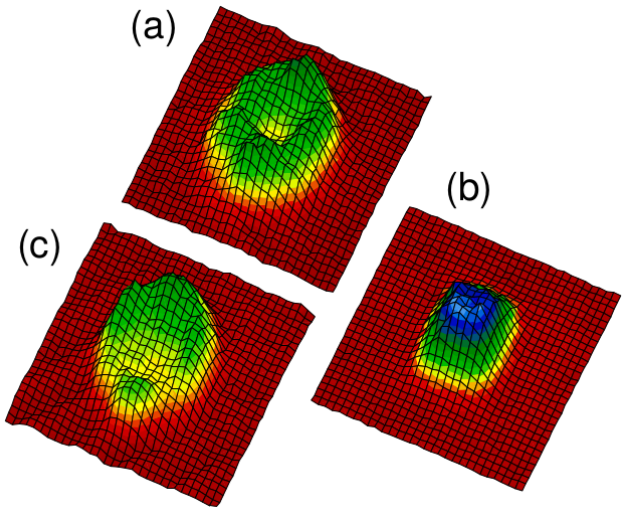

Figure 1.1: In-trap equilibrium configurations for the ^{87}Rb mixture in the states $|1,-1\rangle$ **(a)** and $|2,1\rangle$ **(b)**. New position of the $|1,-1\rangle$ component in the presence of a relative potential sag **(c)**. Image taken from [25]

trapping potential $V_{\mathrm{a}}(\mathbf{x}) = V_{\mathrm{b}}(\mathbf{x})$, the resulting profiles for miscible states are:

$$\begin{aligned} n_{\mathrm{a}}(\mathbf{x}) &= \frac{1}{g_{\mathrm{aa}}\,(1-\Delta)}\left[\mu_{\mathrm{a}} - V(\mathbf{x}) - \frac{g_{\mathrm{ab}}}{g_{\mathrm{bb}}}\,(\mu_{\mathrm{b}} - V(\mathbf{x}))\right] \\ n_{\mathrm{b}}(\mathbf{x}) &= \frac{1}{g_{\mathrm{bb}}\,(1-\Delta)}\left[\mu_{\mathrm{b}} - V(\mathbf{x}) - \frac{g_{\mathrm{ab}}}{g_{\mathrm{aa}}}\,(\mu_{\mathrm{a}} - V(\mathbf{x}))\right] \end{aligned} \tag{1.11}$$

where $\Delta = g_{\mathrm{ab}}^2/(g_{\mathrm{aa}}g_{\mathrm{bb}}) < 1$. Such a result clearly shows that, satisfying the miscibility condition in a state-independent trap is not sufficient to ensure a perfect overlap between the two density profiles, unless $g_{\mathrm{aa}} = g_{\mathrm{bb}}$. This phenomenon is known as *buoyancy*. Even in the absence of mutual interactions ($g_{\mathrm{ab}} = 0$), equations (1.11) decouple and each component, assuming harmonic confinement, independently arranges to an inverted parabola density profile. Peak density and Thomas-Fermi radius rates are set by the interaction parameters [34]

$$\frac{n_{\mathrm{a}}(0)}{n_{\mathrm{b}}(0)} \propto \left(\frac{g_{\mathrm{bb}}}{g_{\mathrm{aa}}}\right)^{3/5} \qquad \frac{R_{\mathrm{a}}}{R_{\mathrm{b}}} \propto \left(\frac{g_{\mathrm{aa}}}{g_{\mathrm{bb}}}\right)^{1/5}, \tag{1.12}$$

with the more repulsive component showing a reduced peak density and occupying a wider volume of the trap, compared to the other. In the presence of mutual interactions the situation is complicated as each component exerts an effective potential on the other depending on the mutual interaction parameter, leading to a rearrangement of the density profiles. In particular, the mixture involving the states $|1,-1\rangle$ and $|2,1\rangle$ of ^{87}Rb, that is at the boundary of the phase-separation transition, shows the equilibrium configuration reported in Fig.1.1, with one of the components shrunk towards the trap

center and the other pushed outwards. The presence of such a phenomenon is especially undesirable in our experiment, aimed to study the dynamics of spin-related defects, as it introduces complex dynamical behavior, nonlinearities, and instability against perturbations.

Also, the dynamical properties of the mixture are critically affected by the presence of an additional component, and by interactions. An additional excitation branch emerges [32], connected with spin excitations. It is characterized by the linear phonon-inc spectrum at large wavelength $\omega_k = c_\mathrm{s}\,|\mathbf{k}|$, and describes oscillation of the two components in anti-phase (spin sound waves). The corresponding density and spin propagation velocities, for an unpolarized state $n_\mathrm{a} = n_\mathrm{b} = n/2$ and in the simplifying assumption $g_\mathrm{aa} = g_\mathrm{bb} = g$ are

$$c_{\mathrm{d,s}} = \sqrt{\frac{n(g \pm g_\mathrm{ab})}{2m}}, \tag{1.13}$$

where the plus and minus refer to the density (+) and spin velocity (-), respectively. At the miscibility transition point, the speed of sound vanishes, and the system exhibits critical behavior and spin fluctuations [32, 35, 36].

Two important length scales, that are used throughout the chapter, can be defined for the system. The density healing length ξ_d, that analogously to the single component case represents the distance necessary to restore the equilibrium value of the density to n, from zero, and the spin healing length ξ_s, defined respectively as

$$\xi_\mathrm{d} = \frac{\hbar}{\sqrt{2mng}} \qquad\qquad \xi_\mathrm{s} = \frac{\hbar}{\sqrt{2mn\delta g}}, \tag{1.14}$$

where $\delta g = g - g_\mathrm{ab}$.

Sodium, in particular, has two miscible states in the lower hyperfine manifold $|1,-1\rangle$ and $|1,1\rangle$ (hereby $|-1\rangle$ and $|1\rangle$). In the zero magnetic field limit, the corresponding s-wave scattering lengths are [37]:

$$a_{1,1} = a_{\text{-}1,\text{-}1} = 54.54(20)\,a_0 \qquad\qquad a_{\text{-}1,1} = 50.78(40)\,a_0, \tag{1.15}$$

given in units of the Bohr radius a_0. In the pseudo-spin representation [6–8, 38], sodium is characterized by anti-ferromagnetic interactions, while typically employed mixtures of internal states of ^{87}Rb and ^{41}K show ferromagnetic interactions. The symmetry in the intra-species interaction parameter $g_{11} = g_{\text{-}1,\text{-}1} = g$, leads for this mixture to the absence of buoyancy, hence allowing for perfect density overlap between the two components of a trapped mixture. The other peculiarity is its closeness to the miscible-immiscible phase transition, with a relative difference between the interaction parameters of $g - g_{\text{-}1,1} = \delta g \simeq 0.07\,g$. This, in fact, leads to a ratio of roughly 5 between density and spin sound velocity. Remarkably, a sizable effect of the same order is experimentally observed on the linear response properties of this stable mixture, as discussed in next subsection.

1.1.3 Spin dipole oscillation and polarizability at zero and finite temperature

Simultaneously to the buildup of the new apparatus, we accomplished two studies of static and dynamic linear response properties of the sodium mixture composed of the $|-1\rangle$ and $|1\rangle$ states, in another sodium-based experiment. In particular, we investigated the *spin dipole* (SD) polarizability and oscillation frequency, both in the limit of low temperature [20], and at finite temperature [39] . Here I briefly describe the results of these studies, while a complete treatment can be found in [40].

In the zero temperature limit thermally excited atoms are absent and only the two Bose-condensed components are relevant. The linear dipole perturbation is accomplished by a small relative displacement $2x_0$ of the trap minima, for the two components, in the limit of small displacement [41]

$$V_{1,\text{-}1} = \frac{1}{2}m\omega^2 \left(x \pm x_0\right)^2 \simeq \frac{1}{2}m\omega^2 x^2 \pm m\omega^2 x_0 x. \tag{1.16}$$

The *spin dipole* (SD) polarizability $\mathcal{P}$, defined by the adimensional ratio $\mathcal{P}(x_0) = d(x_0)/2x_0$, quantifies the separation d between the two interacting mixture components, induced by the perturbation. In particular, d is quantified by the distance of the two distributions centers of mass. For two mutually non-interacting components ($g_{\text{ab}} = 0$), the separation d would correspond exactly to the displacement of the trapping potential minima $2x_0$, and the corresponding polarizability would be $\mathcal{P} = 1$. Conversely, near the miscible-immiscible phase transition, the interactions are expected to enhance dramatically the intercomponent displacement [42]. Within the *local density approximation* (LDA) an analytic expression for the static polarizability in the linear regime is given as

$$\mathcal{P}(x_0 \to 0) = \frac{g + g_{\text{-}1,1}}{\delta g}. \tag{1.17}$$

The LDA also predicts a connection between the SD oscillation frequency and the static polarizability

$$\omega_{\text{SD}} = \omega_{\text{x}}\sqrt{\frac{\delta g}{g + g_{\text{-}1,1}}} = \frac{\omega_x}{\sqrt{\mathcal{P}(x_0 \to 0)}}, \tag{1.18}$$

where $\omega_x/(2\pi)$ is the harmonic oscillator frequency. The SD oscillation mode is the simplest spin collective mode, and corresponds to the two components oscillating in anti-phase, ideally with a stationary profile of the total density. The relation (1.18) predicts a reduction of the SD frequency as the miscibility phase transition is approached. The experimental results show polarizabilities larger than 20, and measurements of the SD frequency of the order of $0.2\omega_{\text{x}}$, in good agreement with the both the LDA predictions, and the more accurate numerical GPE simulations made in Trento by Chunlei Qu [20].

In a second set of measurements [39], the behavior of the SD polarizability and SD oscillation frequency were investigated at finite temperature, where each component of

the mixture is composed of both a condensed and a thermal fraction, and the system can be described with a four-fluid model. Using two different trap configurations, the system was prepared either in the collisional or in the collisionless regime [43]. The results of this set of measurements, compared to the ones previously obtained in the low temperature regime, showed a further enhancement of the polarizability associated to the condensed fraction, with a negative polarizability associated to the thermal fraction, while the total polarizability of the system remains unchanged compared to the low temperature case. The dynamical behavior of the thermal fraction, instead, differs in the two collisional regimes. A counter-phase oscillation, driven by mean-field interaction with the condensates, is observed in the collisionless regime, while in the collisional one the thermal part oscillation relaxes on the order of one trap period. In particular, the occurrence of undamped oscillations of the condensed fraction, in the presence of strong collisions, is interpreted as a definitive signature of spin superfluidity.

In the perspective of my project, these measurements provided an early confirmation of the expected properties of the sodium mixture, both in terms of stability against spin perturbations, and of a sizable enhancement on the spin-response of the system, as a consequence of the vicinity to the miscible-immiscible phase transition.

1.1.4 Defect dynamics in multicomponent BECs

In the previous subsection I discussed a few basic properties of two-component quantum degenerate Bose mixtures, with emphasis on the peculiar properties of the sodium mixture $|1,-1\rangle$ and $|1,1\rangle$. Here I focus on the dynamics of topological defects in multicomponent BECs, underlining some of the interesting aspects that emerged in recent studies, in comparison to the single-component case.

Quantized vortices and vortex lattices in BEC mixtures

Quantized vortices have been an important topic in low temperature physics. Superfluid vortices were first studied in the context of liquid superfluid helium, and exhibit a direct correspondence with magnetic flux lines in Type II superconductivity. Analogies with other fields can also be established, such as optics [44], while other studies highlight the connections between superfluidity and global vortices in relativistic field theories [45, 46]. Early experimental realizations of one or a few vortices in trapped BECs were accomplished with ^{87}Rb, both in a one component condensate [47, 48] and in a binary mixture [38]. Vortices in single component BECs are topologically stable defects that consist in a linear (in three spatial dimensions) or point-like (in two dimensions) vortex core of vanishing density (whose spatial extent is of the order of the healing length ξ), and an extended phase pattern, consisting of a quantized winding of $\pm 2\pi$ along any closed path encircling the vortex core. Their precession dynamics in trap and interaction properties, both driven by currents, were extensively studied (for a review, see for instance [49]). While a multiply quantized vortex satisfies the single-valueness condition for the order parameter phase, such a configuration is energetically unfavorable and leads to the proliferation of singly quantized vortices, which allowed to experimentally generate a large number of vortices [50]. Vortices with the same

winding exert on each other a repulsive force $F(r) \propto 1/r$, where r is the inter-vortex distance, leading to regular triangular vortex lattices (Abrikosov lattice), analogous to the ones of quantized magnetic flux lines observed in Type II superconductors [51]. The predicted Tkachenko oscillation modes were also observed [52].

The structure and dynamics of vortices and vortex lattices is further enriched in multicomponent systems. The increased dimensionality of the order parameter given by the additional component, compared to the single component case, can be regarded as an analogous comparison between fermionic ^{3}He, where rich topological structures emerge, and ^{4}He [1]. The vortex state in the mixture differs from the single-component case in the fact that the hollow core of the rotating component is filled by the nonrotating component, with intercomponent interactions determining the core structure. In particular, effects related to buoyancy in both the in-trap motion and the vortex stability have been observed with ^{87}Rb [38]. The pivotal role of interactions and population inbalance in determining the stability of the vortex configuration are discussed in detail in [6, 53, 54]. Notably, for the sodium mixture that we plan to use, vortices in both components are stable against dynamical instabilities. Mean-field interactions also determine the interaction between vortices in different components [55] which is independent of the winding direction $F(r) \propto g_{\mathrm{ab}}/r^3$. The interplay between same- and different-component vortex interactions produces interesting vortex lattice configurations. Studies on ^{87}Rb mixtures [56] showed a structural transition between the Abrikosov lattice structure, in the single component condensate, to a structure of interleaced square lattices, as soon as the second component was added. Such a structure shows analogies to other systems, such as the two-dimensional electron gas [57]. A rich phase diagram, involving both the aforementioned triangular and square lattice structure, as well as additional unconventional vortex structures, is predicted to emerge as different values of interaction parameters and rotation speeds are considered [6, 58].

Solitons in binary mixtures

A one-dimensional system cannot host quantized vortices. Conversely, stable solitons can be observed. These defects, characterized by a steady density profile in their co-moving reference frame, were extensively studied in different fields. They emerge from the interplay between dispersion and nonlinearities, and in particular as a solution of nonlinear Schrödinger equations, such as the GPE. Solitons in single components BECs manifest themselves as either *bright* and *dark*(or *gray*) solitons, for attractive [59] and repulsive [60, 61] interactions, respectively, where the density profile is accompanied by a phase discontinuity of π in the order parameter for dark solitons. Solitons in BEC mixtures, come in a rich variety of structures, such as dark-dark and dark-bright solitons [62, 63], that were first observed in nonlinear optics experiments [64]. In a different setting, the magnetic soliton was recently proposed [65]. Such a configuration is characterized by a localized magnetization profile ($n_1 - n_2 \neq 0$) in an otherwise unpolarized medium ($n_1 = n_2$) and can be observed in a regime of interactions compatible with the $|-1\rangle - |1\rangle$ ^{23}Na mixture. Another advantage of this mixture relates to the expected increased stability against snaking instabilities, as the spin healing length ξ_{s} is larger than the density healing length [66]. A very similar configuration, with a

polarized background, was recently reported with ^{87}Rb [67].

1.2 Rabi-Coupled binary mixtures

As discussed previously, multicomponent BECs are characterized by intricate phenomena emerging from inter-component mean field interactions. The components of the order parameter interact with each other through their density, in particular with consequences on the structure of defects, such as vortices and solitons, that were studied in recent years, as discussed in the previous section. Now I focus on the possibility to induce coherent coupling between such components. This allows to coherently transfer the population from one state to the other producing the mixture in the desired state, as in [38], or to exploit the nonlinearities, induced by the interactions in the evolution of coherent internal states, to devise quantum-enhanced interferometers [68]. However, in the presence of a steady coupling, the relevant parameter of the coupled two-component system is the relative phase. This, as explained in the following subsections, allows for interesting phenomena and novel structures of defects, and is the main scope of the new experiment that I primarily contributed to assemble. Outside the study of defect dynamics, recent proposals pointed out the advantage of using Rabi coupled mixtures in different applications, such as to devise analog models of gravitational physics [69], or to tune the stability of self-bound droplets [70].

In the presence of a stationary Rabi coupling, the energy functional (1.6) comprises an additional term

$$E_{\mathrm{R}} = -\frac{\hbar\Omega}{2}\int \mathrm{d}\mathbf{x}\,(\Psi_{\mathrm{a}}^{*}\Psi_{\mathrm{b}} + \Psi_{\mathrm{b}}^{*}\Psi_{\mathrm{a}}) = -\hbar\Omega\int \mathrm{d}\mathbf{x}\,|\Psi_{\mathrm{a}}|\,|\Psi_{\mathrm{b}}|\cos(\phi_{\mathrm{b}} - \phi_{\mathrm{a}}), \tag{1.19}$$

where Ω, the Rabi frequency, quantifies the strength of the coupling, and the coupling time dependence was removed by switching to a co-rotating reference frame. This term clearly shows that the energy density of two overlapped components is reduced when they have the same phase value. Analogously to section 1.1.1, the evolution is described by coupled GPE, with an additional coupling term

$$\begin{aligned} i\hbar\frac{\partial}{\partial t}\Psi_{\mathrm{a}} &= \left(-\frac{\hbar}{2m}\nabla^2 + V_{\mathrm{a}} + g_{\mathrm{aa}}\,|\Psi_{\mathrm{a}}|^2 + g_{\mathrm{ab}}\,|\Psi_{\mathrm{b}}|^2\right)\Psi_{\mathrm{a}} - \frac{\hbar\Omega}{2}\Psi_{\mathrm{b}} \\ i\hbar\frac{\partial}{\partial t}\Psi_{\mathrm{b}} &= \left(-\frac{\hbar}{2m}\nabla^2 + V_{\mathrm{b}} + g_{\mathrm{ab}}\,|\Psi_{\mathrm{a}}|^2 + g_{\mathrm{bb}}\,|\Psi_{\mathrm{b}}|^2\right)\Psi_{\mathrm{b}} - \frac{\hbar\Omega}{2}\Psi_{\mathrm{a}} \end{aligned} \tag{1.20}$$

As the coupling term introduces interconversion between the atomic states, a global value of the chemical potential μ, defined by the conservation of the total number of atoms, appears in the stationary solutions.

1.2.1 Static and dynamic properties

The system ground state in the presence of Rabi coupling is different from the one previously stated, as a consequence of both the relative phase, and the possibility of interconversion between the states. In this case, it is identified with the one that

minimizes the energy density of the system, that can be easily calculated from the total energy functional in the case $g_{aa} = g_{bb} = g$, as [32]

$$e(n_a, n_b) = \frac{1}{2} g \left(n_a^2 + n_b^2\right) + 2 n_a n_b g_{ab} + 2 |\Omega| \sqrt{n_a n_b} \cos(\phi_1 - \phi_2) - \mu(n_a + n_b) \quad (1.21)$$

This predicts, analogously with the previous case, two possible configurations, depending both on interactions and on the strength of Rabi coupling. For dominating intra-component repulsive interactions and/or Rabi coupling

$$g_{ab} < g + \frac{2\Omega}{n}, \quad (1.22)$$

that is analogous to the miscible phase case of the binary mixture, the ground state of the system is an unpolarized ($n_a = n_b$) and phase-locked ($\phi_a = \phi_b$). This state is referred to as *paramagnetic phase*. For arbitrary initial conditions, the coupling induces an internal Josephson dynamics on the system population and relative phase [71], for which the unpolarized state is a fixed point, and the system can be experimentally prepared in the minimum energy state with a proper protocol. Note that a system which satisfies the miscibility condition satisfies, by default, also the condition (1.22). The reverse is not true, and can be exploited to explore coupling-induced mixing-demixing dynamics. Note, however, that the in presence of strong Rabi coupling, the correct base in which the miscibility condition should be evaluated is the dressed states eigenbasis [27]. On the other hand we are mainly interested in the low-coupling regime, as is explained in the next subsection, and we expect that the sodium mixture involving the $|-1\rangle$ and $|1\rangle$ internal state will access to the paramagnetic regime. If, on the contrary, the condition (1.22) is not satisfied, the solution minimizing the energy of the system is a polarized configuration (ferromagnetic phase), leading to a population dynamics analogous the Josephson self-trapping regime [32]. The presence of the additional coupling term also has direct consequences on the spin excitation spectrum [32], on the stability criteria for persistent currents [72], and on the linear response properties that we studied in the absence of Rabi coupling [41] (described in subsection 1.1.3).

1.2.2 Domain wall of relative phase

An effective description of the system can be obtained on a length scale larger than the spin healing length ξ_s, by assuming uniform densities for the two components. In this approximation, the relevant degrees of freedom of the system are only the order parameter phases, and the system energy functional can be cast in the simple form [73]

$$E[\phi_a, \phi_b] = \int \mathrm{d}^3 x \left\{ -\frac{\hbar^2}{2m} \left[n_a \left(\nabla \phi_a\right)^2 + n_b \left(\nabla \phi_b\right)^2 \right] - \hbar\Omega \sqrt{n_a n_b} \cos\left(\phi_a - \phi_b\right) \right\}. \quad (1.23)$$

The first term on the right-hand side of the equation accounts for the kinetic energy cost associated to currents in each component, while the second is a direct consequence

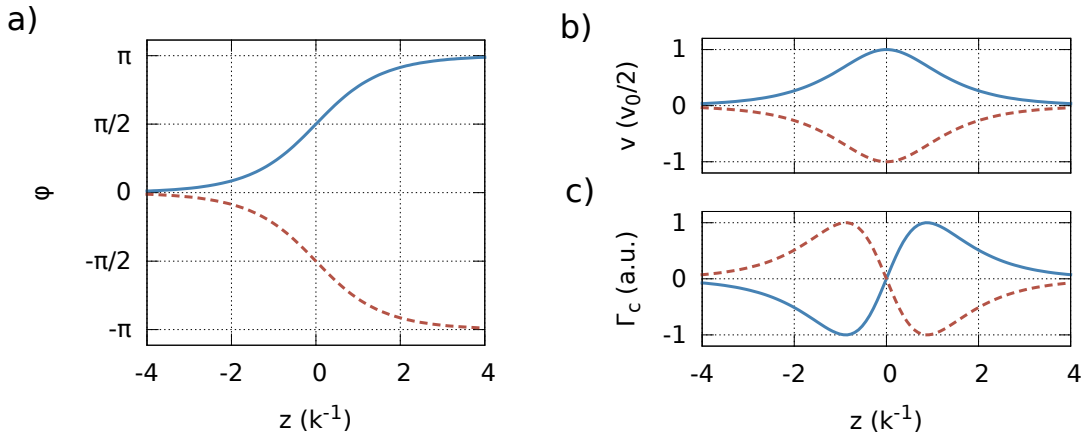

Figure 1.2: Values of the phase $\phi_{\rm i}(z)$ **(a)**, velocity $v_{\rm i}(z)$ **(b)**, and interconversion rates **(c)**, as a function of the coordinate z across the domain wall (centered at $z = 0$), for the a (blue, solid) and b (red, dashed) components.

of the presence of Rabi coupling, promoting a phase-locked state. The trivial system ground state is phase locked, $\phi_{\rm a} = \phi_{\rm b}$. In the same hypotheses on the interaction parameters $g_{\rm aa} = g_{\rm bb} = g$ introduced in the previous section and suitable to describe our sodium mixture, the state can also be assumed unpolarized $n_{\rm a} = n_{\rm b} = n/2$. The interplay between currents and coupling allows for a localized excitation consisting in the appearance of a domain wall configuration, that is a local minimum of the energy functional (1.23). By varying such a functional with respect to the phases $\phi_{\rm i}$, the following conditions are obtained

$$\frac{\hbar^2}{2m}\nabla^2\phi_{\rm a} = -\frac{\hbar^2}{2m}\nabla^2\phi_{\rm b} = \hbar\Omega\cos\left(\phi_{\rm a} - \phi_{\rm b}\right). \tag{1.24}$$

For a domain wall configuration, where the phase varies only along one direction (z)

$$\phi_{\rm a} = 2\arctan\left(e^{kz}\right) \qquad\qquad \phi_{\rm b} = -\phi_{\rm a}, \tag{1.25}$$

where k^{-1} defines the domain wall width

$$k^{-1} = \sqrt{\frac{\hbar}{2m\Omega}}. \tag{1.26}$$

Such a configuration is plotted in Fig.1.2(a). Differentiating the phase values in (1.25), with respect to the z coordinate, both the current density and its divergence are easily obtained, and are plotted in Fig.1.2(b,c). This allows to give a phyiscal interpretation in terms of a symmetric current counterflow in the two different species, or equivalently as a pure spin-current, with no mass current component. The peak counterflow velocity increases with the coupling strength, as

$$v_0 = 2\sqrt{\frac{\hbar\Omega}{m}}. \tag{1.27}$$

Since the configuration has stationary density values, the divergence value of the current directly accounts for Rabi-induced particle interconversion, which maintains the density balance in spite of the spin current. The domain wall has an energy cost that is proportional to its extention, and the corresponding tension is

$$\sigma = n\sqrt{8\frac{\hbar^3\Omega}{m}}. \tag{1.28}$$

The domain wall configuration is experimentally controlled through the coupling strength Ω. Larger values lead to an increase of the wall tension and the counterflow velocity of the two components, and to the reduction of the wall width. As argued in [73], above a critical coupling strength $\Omega_{\rm crit}$ the wall is expected to be unstable. Density fluctuations, neglected in the derivation of (1.23), become important as the domain wall gets as thin as the spin healing length. In this case, they can lead to one component vanishing, with the consequent loss of the relative phase. The critical value of coupling for which $k^{-1} \simeq \xi_{\rm s}$ is $\hbar\Omega_{\rm crit} \simeq n\delta g$. This condition corresponds to having the peak counterflow velocity of the same order of the spin sound velocity. Such instabilities show interesting features, as discussed in next subsection.

1.2.3 Defect dynamics in Rabi-coupled binary mixtures

Magnetic soliton

The above described domain wall configuration, corresponds to a static magnetic soliton configuration, predicted in the presence of Rabi coupling [74]. The moving soliton differs from the static domain wall in the finite magnetization profile, in correspondence to the phase jump. It differs also from magnetic solitons in the absence of coupling [65], by the relative phase jump of 2π, rather than π, which ensures that the system is in the ground state far from the soliton, and by the fact that its energy and magnetization increase with its velocity, instead of decreasing. These characteristics are in stark contrast with the ones exhibited by typical solitons, and should lead to interesting dynamical phenomena, such as an increasing velocity in the presence of dissipation [75,76], and recursive configurational transitions [74] during in-trap evolution.

Vortex molecules

As argued in [73], and confirmed by simulations [77,78], a pair of vortices in the two different components, with the same orbital momentum, provide the natural boundary for the domain wall between the two cores. Indeed, while the relative phase must vary by 2π along a closed path around the domain wall boundary, the phase variation along a closed path encircling a vortex in one of the two components is 2π for the rotating component, and zero for the other component (See fig. 1.3(a,b)). On the other hand, in the presence of Rabi coupling, the domain wall configuration is energetically favored compared to the bare-vortex phase winding. Turning on the coupling in a system where bare vortices are already present, results in the formation of domain walls that

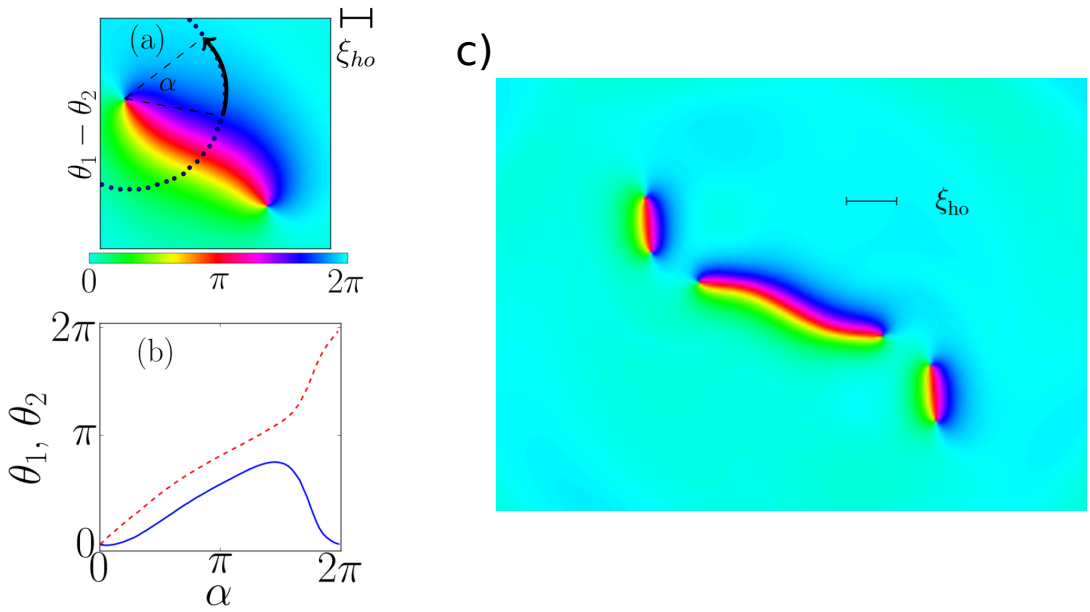

Figure 1.3: Simulation results taken from [77]. **a)** Relative phase near a vortex pair and in the presence of a Rabi coupling, showing a domain wall profile. **b)** Phase profiles of the two components along the dotted path shown in the top panel. The component whose phase is represented with the red dashed curve, is the same as the vortex enclosed in the path. **c)** Result of the domain wall fragmentation for a Rabi coupling strength above the critical value.

connect each vortex either to another vortex in the other component, or to the system boundary. The domain wall tension dominates over the inter-vortex repulsive force at large distances, causing an attractive force, which is independent of distance when the vortices are far apart. This brings an interesting analogy with quark confinement in QCD [79], and also with similar composite defects that were observed in $^3\mathrm{He} - \mathrm{B}$ [80]. As Rabi coupling is increased beyond the critical value the wall breaks and new vortex couples form as boundaries of the wall fragments. Such a dynamics was also reproduced in simulations [81] (see Fig. 1.3(c)), and shows analogies with the phenomenon of string breaking in QCD. An in-depth study of these analogies can also be found in [82]. At the distance for which the intra-vortex interaction, which is repulsive for $g_{12} > 0$, is balanced by the domain wall tension, the configuration forms a vortex molecule whose structure depend on mean-field interactions [78]. Also vortex motion inside the trap is modified by the presence of the domain wall, as discussed in [77, 83]. A rich dynamical evolution is predicted also for the single vortex, including coherent transfer of vorticity between the two components in the absence of net population transfer [83], that is analogous to an effect previously predicted for coherently-coupled mixtures in annular BECs [84].

The interplay between interactions, rotation and the effect of coherent coupling is

also predicted to enrich the possible vortex-lattice configurations. As vortices are bound in couples that interact non-trivially with each other, different intricate multi-dimer bound states and complex dynamics can emerge for different values of the parameters [85–88].

1.2.4 Magnetic field stabilization

As the relative phase between the states composing the mixture explicitly determines the system dynamics, the mixture must be stabilized against dephasing-inducing effects. Phase decoherence is accumulated during the evolution of the system, as a consequence of differential energy drifts between the internal states of the mixture, with fluctuations of the magnetic field being the major contributor. The two ^{87}Rb mixtures, involving the $|1,-1\rangle$ and $|2,1\rangle$ [89–91], or the $|1,0\rangle$ and $|2,0\rangle$ [92] hyperfine states, are characterized by insensitivity to magnetic field perturbations (at first Zeeman order), which allows to circumvent the problem of magnetic field fluctuations in several experiments, allowing to observe coherent behavior on a scale of seconds, but, as mentioned earlier, they are subject to buoyancy. The stable mixture of sodium in the hyperfine states $|1,\pm1\rangle$, on the other hand, is characterized by the other desirable properties described in this chapter, namely the absence of buoyancy, a stable superposition against small spin-dependent perturbations, and a large ξ_s. These features, favorable for observing defect evolution induced by mean-field interactions, come at the cost of a more technically difficult to access coherence due the sensitivity of the mixture to external magnetic field fluctuations, requiring a specific effort to deal with magnetic field fluctuations. More quantitatively, the differential energy shift induced on the two states by a weak magnetic field perturbation is $\Delta E = 2\pi\hbar \times 1.4$ MHz/G. In order to observe a coherent in phase evolution of the system on a timescale of the order of 100 ms, a cancellation of spurious magnetic field fluctuations to better than 10 µG is required. The novel apparatus was specifically designed to operate in this regime of high magnetic field stability, ensuring coherent phase evolution in a mixture which is subject to Zeeman differential energy shifts, by employing a suitable µ-metal shield, that was designed in the context of another Ph.D. thesis [40], while I focused on the production of quantum-degenerate samples with a protocol compatible with the saturation limits of the magnetic shield. This topic is discussed in Chapter 4.

An additional magnetic field noise source are the current fluctuations in the magnetic coils placed inside the shield, induced by the corresponding power supplies. The necessary magnetic field stability can be obtained by means of high-stability current generators. In particular, commercial laser diode drivers (e.g. SRS-LD500) allow for a relative current stability of 10^{-5}. Using such devices to produce magnetic fields of the order of 0.1 G fulfills the magnetic field stability requirement, and results in a Zeeman splitting of the order of few tens of kHz, sufficient to efficiently control the coherent coupling between the two components.

Chapter 2

Buildup of the experimental apparatus

***

In this chapter I describe the construction of the experimental apparatus, that was one of the main objectives of this thesis work. I gave a main contribution to the assembly and implementation of all that is described in this chapter.

In the first five sections I describe the hardware of the experimental apparatus. In the first section the Vacuum chamber assembly is described accounting for specific material and design choices. In the second section I briefly describe the electronic control system by means of which we are able to execute time-resolved experimental sequences. The third section deals with the production of the near-resonant laser

radiation necessary for laser cooling and magneto-optical trapping. The fourth section deals with magnetic-field generating elements and, in the context of mgnetic trapping, RF-generating elements. The compatibility of such elements with µ-metal magnetic shielding is discussed. In the fifth section I describe the optical dipole trap system. The sixth section of the chapter deals with the operation and optimization of the atomic source and *dark-spot magneto-optical trap* (DS-MOT), while in the last section a description of the imaging system and procedures is given.

2.1 Vacuum chamber

2.1.1 Design overview

Vacuum chambers designed to host ultracold-atom experiments must comply with a few yet crucial requirements. The first is to ensure a top-quality vacuum where quantum degenerate samples are produced and studied. Collisions with hot background atoms contribute with a density-indpendent term to the collisional loss rate, limiting the atomic sample lifetime. Increasing such a lifetime is especially critical to reach quantum degeneracy, since its ratio with the average elastic collisional time is one of the main figures of merit of evaporative cooling. A longer sample lifetime is also particularly desirable in our experiment, allowing to observe for longer times the dynamical evolution of two-component BECs in the presence of Rabi coupling. The other important requisite for the vacuum apparatus is to ensure the needed optical access for laser-based cooling, trapping and imaging techniques through optically transparent vacuum-compatible components.

Materials composing all the needed elements must be chosen accordingly. Such materials must have low outgassing properties and tolerance to the high (about $250 - 300\,^{\circ}\mathrm{C}$) temperatures commonly reached during bake-out procedures. Another requirement is to have magnetic and electrical properties that minimize magnetizations and eddy currents in the chamber, that could affect the atomic sample in an uncontrolled way. As stated earlier in Chapter 1, particular care must be taken to avoid such spurious effects in our experiment. AISI 316L, a stainless steel alloy characterized by a relatively low magnetic permeability, typical of austenitic alloys, and low electrical conductivity, was chosen as bulk material for the chamber.

The chamber, as shown in Fig. 2.1, is composed of two sections, connected by a *differential pumping* (DP) channel (2 mm diameter and 22.8 mm length). Such connection can be sealed by means of an all-metal gate valve and allows for a maximum pressure ratio of about 10^2 between the sections. In order to avoid mechanical strains that may be caused by manufacturing imperfections, imperfect alignment of the components during assembly or thermal gradients, the two sections are mechanically connected through a flexible bellow. The *High Vacuum* (HV) section hosts the atomic source, and is filled with high-temperature atoms during normal operation. The *ultra-high vacuum* (UHV) side in contrast offers a cleaner environment and hosts the octagonal quartz cell where the experiment takes place. Each section hosts a vacuum pump, as described in more detail in next subsection.

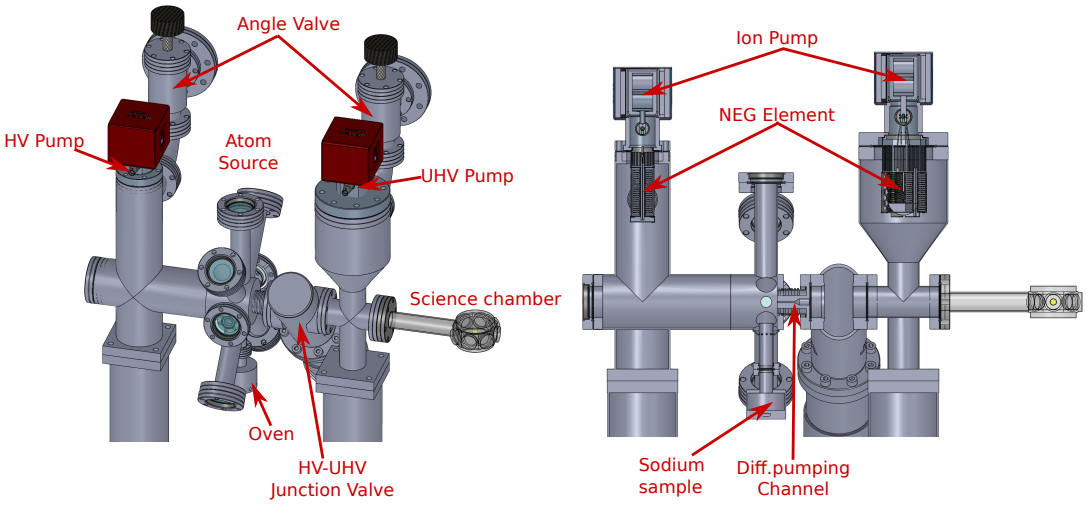

Figure 2.1: Rendering of the vacuum chamber, showing the position of the various elements discussed in the text.

2.1.2 Description of the individual chamber elements

Pumping apparatus

The pumps used in the two chambers are NEXTorr D200-5 (for the HV side) and NEXTorr D500-5 (for the UHV side). Each of them consists into a *Non Evaporable Getter* (NEG) acting as the main pump for active gases, and a *Ionic Pump* (IP) that primarily removes noble gases and methane, which are not pumped by the NEG elements. Pumping speeds for the D200 NEG element range from 200 l/s for molecular oxygen and hydrogen to 80 l/s for molecular nitrogen, while the same values for the D500 NEG element amount to 500 l/s and 200 l/s respectively. NEGs are chemically activated by heating them at 500 °C for 1 hour by means of a built-in heating element. Such procedure must be repeated every time the vacuum chamber is opened. The pumps are provided with µ-metal layered covers in order to attenuate the magnetic field generated by the IP magnets. Since the magnetic field characterizations supplied us by the company show that such residual field is not perfectly isotropic, care was taken to orient the pumps in order to minimize such spurious field in the direction of the octagonal cell.

Atomic source

The atomic source main body consists of eight connection tubes protruding orthogonally to the DP channel axis. As shown in Fig. 2.1, all the tubes, with the exception of the bottom one connected to the oven, are sealed with a window. Such windows provide optical access for atomic source operation, as explained in subsection 2.6.1.

The windows consist of Kodial borosilicate glass mounted on a CF40 stainless steel flange. Anti-reflection coating treatments for 589/850 nm wavelengths were applied on the windows by a specialized company. The top window is not coated on the

internal side that is directly exposed to the atom flux evaporated from the oven, to avert chemical reactions with the coating material, and is constantly heated to a temperature of 230 °C to prevent such atoms from depositing on the surface. All the other windows employed in the apparatus are AR-coated on both sides. The coating was explicitly required to be compatible with UHV conditions and temperatures up to 300 °C.

The oven connection to the chamber body is sealed by means of a zinc gasket, and embedded in layers of glass wool and aluminium foils. Temperature is actively stabilized by means of heating cartridges, a type K thermocouple and an industrial-grade digital PID controller.

Science chamber

The science chamber is a custom-made UHV-compatible octagonal quartz cell. Double-side AR treated fused-silica windows seal seven out of the eight circular apertures on the side faces (19 mm diameter optical access), as well as both apertures on the top and bottom faces (50.8 mm diameter optical access). The remaining side is connected to the UHV section of the chamber through a 65 mm long connection tube. The external size of the cell, taking into account the windows thickness, is 38.1 mm height and 35.5 mm inradius.

AR treatment is required not only in order to avoid the power loss on light transmitted through uncoated surfaces, but also to prevent other spurious effects caused by uncontrolled reflections, such as imaging aberrations, etalon effects and lattice-like optical potentials on the condensate. Wavelengths of interest for the experiment in addition to the $589 - 590$ nm resonant wavelength are the far-off resonance 1064 nm and 532 nm wavelengths used to produce attractive and repulsive optical potentials, respectively.

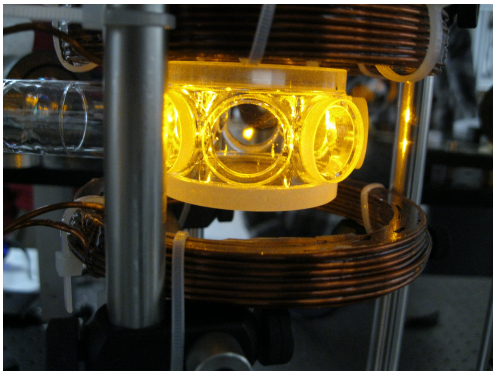

Figure 2.2: The science chamber during 3DMOT operation, showing the fluorescence of trapped sodium atoms.

Including all the frequencies of interest in a broadband AR coating would have reduced the efficiency of the treatment; the only other possibility was to require an AR-coating specific for visible light for some of the windows, and one specific for infrared light on the others. In both cases the possible choices for the coating material would have been limited to the ones that can withstand the high temperatures needed for cell assembly via molecular bonding, of the order of 1000 °C. Accounting for this, a *Random-type anti-reflection* (RAR) treatment was chosen. Such a treatment consists in random nano-textures etched directly on the window surfaces, allowing to devise high temperature resistant and high-efficiency broadband AR treatments compared to thin-film coating treatments. For 589 nm laser light we measured a relative power loss as low

as 10^{-4} per surface, while for 1064 nm radiation we measured a single-surface reflection below 0.06%, at an incidence angle of roughly 10°. These measurements confirm the spectra provided by the supplier, reported in Fig.2.3, which report similar performances for 532 nm wavelength.

a)

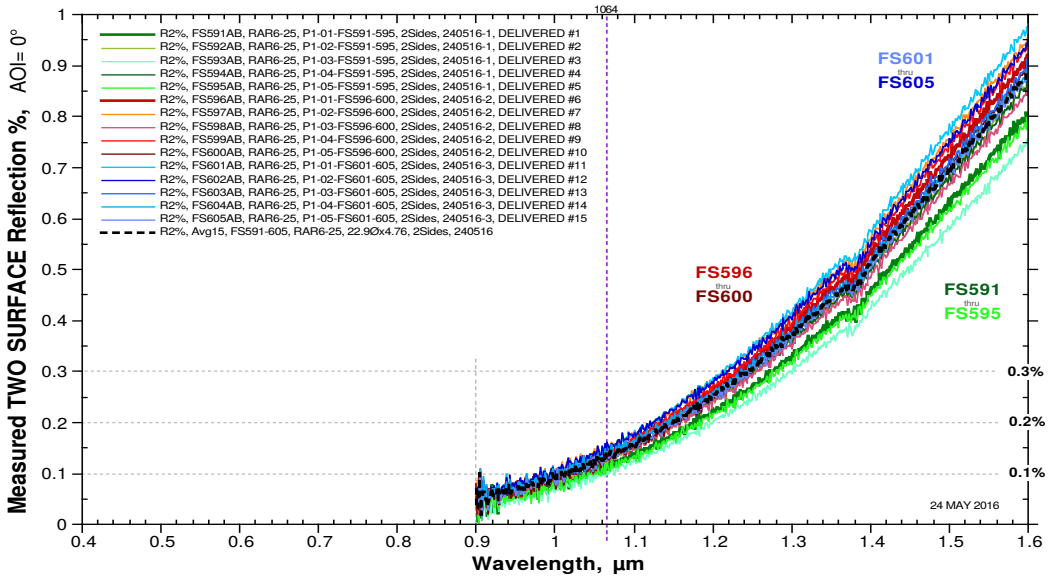

b)

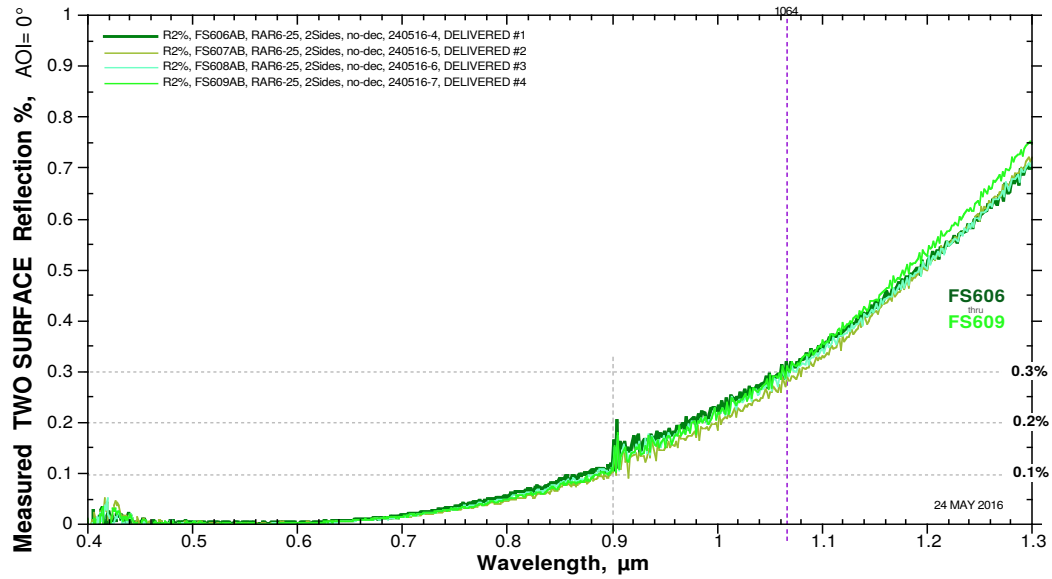

Figure 2.3: Two-surface reflection spectra for a batch of windows, including ours. Shown data in the top graph **(a)** refers to side windows, while the bottom graph **(b)** refers to top and bottom windows. Courtesy of TelAztec.

2.1.3 Baking of the vacuum chamber and pump activation

In order to obtain pressures below 10^{-7} mbar, the vacuum components must be baked to remove impurities that would otherwise degas under vacuum, limiting the lowest attainable pressures. Temperatures of at least 250 °C are needed during the first baking procedure to remove contaminants accumulated during steel components manufacturing process, such as hydrocarbons and hydrogen. A lower temperature baking ($100 - 150$ °C) is sufficient to remove condensed water from the components internal surfaces. Condensed water accumulates as a consequence of air exposure, hence this lower-temperature baking procedure is repeated each time the vacuum chamber internal surfaces are exposed to air.

IPs and NEGs activation and operation are not compatible with atmosphere pressure. In order reach an acceptable vacuum level inside the chamber (*primary vacuum*) required to activate the pumps, as well as to physically remove outgassed contaminants from the chamber during baking procedures, the chamber is temporary connected to a turbomolecular pump. The pump is connected to each section of the chamber through a pair of angle valves (VAT 54132-GE02) sealing the chamber during normal operation.

The vacuum chamber was first assembled without the octagonal cell. The empty oven was baked for three days at about 300 °C, while the rest of the chamber was heated at relatively low temperatures ($120 - 150$ °C). After this procedure, the chamber was opened in inert (Ar) atmosphere and a 5 g metallic sodium sample was loaded into the oven. Performing such operation in inert atmosphere was necessary since metallic sodium is flammable in air. The chamber was then baked at temperatures between 250 and 300 °C for five days. IP magnets, that are not compatible with such temperatures, were temporary removed during the bake-out procedure. Sodium was activated heating the oven to 340 °C. NEG elements and IP were activated after this procedure.

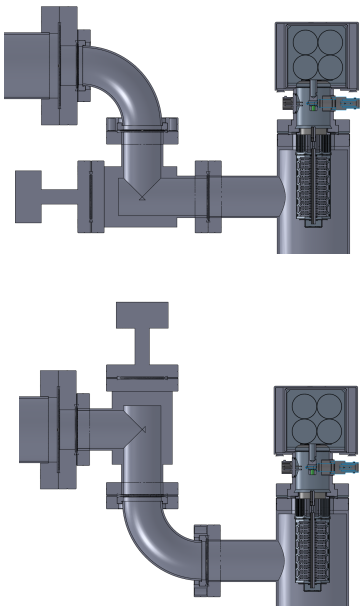

Figure 2.4: First (upper image) and final (lower) configuration of elbow and angle valve.

After sealing the angle valves both IPs reported pressure values below 10^{-10} mbar when the oven was not operated. As the turbomolecular pump was turned off the vacuum inside the chamber degraded, signaling that at least one of the angle valves was leaking. We sent the valves back to the company, which reported a contamination of the vacuum seals. After reparation, considering the possibility that the contaminating material might have been expelled by the NEG element during the activation phase, the assembly geometry was changed as sketched in Fig. 2.4. In this way direct exposure of the valve blades to the NEG element was avoided. Further precaution was taken during baking and NEG activation procedures. Instead of

keeping the valves always open with the turbomolecular pump operating, I kept them sealed when impurities were expected to be expelled (for instance during temperature transients); even when the temperatures stabilized I opened the valves every 20-30 minutes for a few minutes, again minimizing the exposure of the valve blade edges to the degassed elements.

This time, no leak from the valves was observed. Eventually, after the removal of the Turbo pump, both IPs report pressure values below 10^{-10} mbar when the sodium oven is not operated. As the oven is activated and sodium vapor fills the HV section, the corresponding pressure reading stabilizes to about 2×10^{-10} mbar after an initial transient, while no pressure change is observed in the UHV side. As soon as the quartz cell was shipped the chamber assembly was completed, and the cell was baked at $120 - 150°$C for 3 days.

2.2 Experiment control system

The experimental process to produce, manipulate and probe ultracold atomic samples requires some means to dynamically control the experimental variables with a timing precision of 1 µs or better. Perfect reproducibility of the experimental sequence must also be ensured. Such a degree of control over timing is guaranteed by incorporating *field-programmable gate arrays* (FPGAs , Xilinx Spartan XC3S250E, clocked at 10 MHz), in a unified digital control system adapted from the one originally developed by Prof. Marco Prevedelli. A list of time-ordered instructions in human-readable form is given as an input to a specifically designed control application written in Python. After receiving the time-ordered digital instruction list, from the control application, through a USB connection cable, the FPGAs addresses them to specific slave boards by means of a custom 24-channel bus. Each slave board is unequivocally identified by a 7-bit address. The timing resolution and maximum instruction rate of the FPGAs are 100 ns and 2.5 MHz, respectively. Three kinds of slave boards execute the digital instructions received through the bus cable:

- **Digital Boards:** each digital board can provide 16 logical (TTL) output channels. These signals are used as fast switches to perform operation such as trigger image acquisition, control mechanical shutters, pulse-modulate generator outputs, and fast switching of magnetic fields and gradients through IGBTs.

- **Analog Boards:** each board contains two *digital-to-analog converters* (DACs). Analog voltage signals are used to program generator outputs, to tune RF signal amplitudes through mixers and to control the voltage setpoint for dipole trap power stabilization.

- **RF Boards:** boards based on a DDS chip (Analog Devices AD9958), with two independent output channels, capable of generating frequencies between 200 kHz and 140 MHz. Each channel can provide up to 13 dBm output power. These boards are used to drive the AOMs as well as the antenna used to control the depth of the magnetic quadrupole trap potential.

The bus cable length would easily exceed a couple of meters in order to accommodate all the slave boards needed for the experiment. For such long unscreened cables abnormal functioning can be observed as a consequence of cross-talk between neighboring channels, noise pickup, and effects of capacitive load. For this reason the control system is distributed among two different board groups, each controlled by a different FPGA and located in different parts of the laboratory. The FPGAs share the same clock signal, and time synchronization between them is managed by an external microcontroller (Arduino Uno). In the absence of such synchronization, time jitters up to tens of ms in the instruction execution time are observed between the two groups.

2.3 Laser cooling system

Doppler laser cooling techniques exploit the interaction of close-to-resonance laser light with moving atoms to exert on them an effective friction-like force. Such effective force is caused by the prevalence of momentum transfer in the direction opposite to the atom motion during absorption-spontaneous emission cycles (see, for instance, [93,94]). With proper implementation, these techniques can be used to reduce an atomic sample temperature from the hundreds of K of a thermally evaporated sample, down to the so-called Doppler limit, corresponding to $T_{\mathrm{D}} = 235$ µK for sodium atoms. For this atomic species, the stronger available closed transition to take advantage of is the $|F_{\mathrm{g}} = 2\rangle \rightarrow |F_{\mathrm{e}} = 3\rangle$ of the D2 line ($3^2\mathrm{S}_{1/2} \rightarrow 3^2\mathrm{P}_{3/2}$ at 589.2 nm), referred to as *cooling* transition. During the cooling, as a consequence of the dense hyperfine structure of the D2 transition excited state, atoms are optically pumped to the $|F_{\mathrm{g}} = 1\rangle$ manifold through off-resonance excitations to the $|F_{\mathrm{e}} = 2\rangle$ state, ceasing to interact with the cooling radiation. To compensate for this effect the $|F_{\mathrm{g}} = 2\rangle$ manifold must be repopulated by exploiting an additional *repumper* transition ($|F_{\mathrm{g}} = 1\rangle \rightarrow |F_{\mathrm{e}} = 2\rangle$). In addition to laser cooling techniques, (near-)resonant laser light is needed for absorption imaging techniques (described in Section 2.7).

In addition to the D2 laser system, I assembled another laser system whose source is frequency-stabilized on the D1 ($3^2\mathrm{S}_{1/2} \rightarrow 3^2\mathrm{P}_{1/2}$ at 589.8 nm) cooling transition ($|F_{\mathrm{g}} = 2\rangle \rightarrow |F_{\mathrm{e}} = 2\rangle$). This was necessary to implement an efficient dark-state-enhanced sub-Doppler cooling technique, known as *Gray Molasses* (GM) cooling. Such a technique, requiring blue detuned light, allows for deep cooling of the atomic sample, and shows reduced density-dependent heating effects. Both laser systems are described in the present chapter, while the experimental implementation and the results concerning GM cooling protocol are discussed in Chapter 3. Both D1 and D2 laser systems are composed of a suitable frequency-stabilized laser source and an optical system by means of which laser light, controlled in frequency, polarization, and amplitude, is distributed to the various parts of the experiment.

2.3.1 Light sources

Sodium optical transitions are not directly accessible with diode lasers. Although there are alternative choices, such as dye lasers, in order to retain the advantages of solid-state based technology, the chosen approach is to frequency-double an infrared

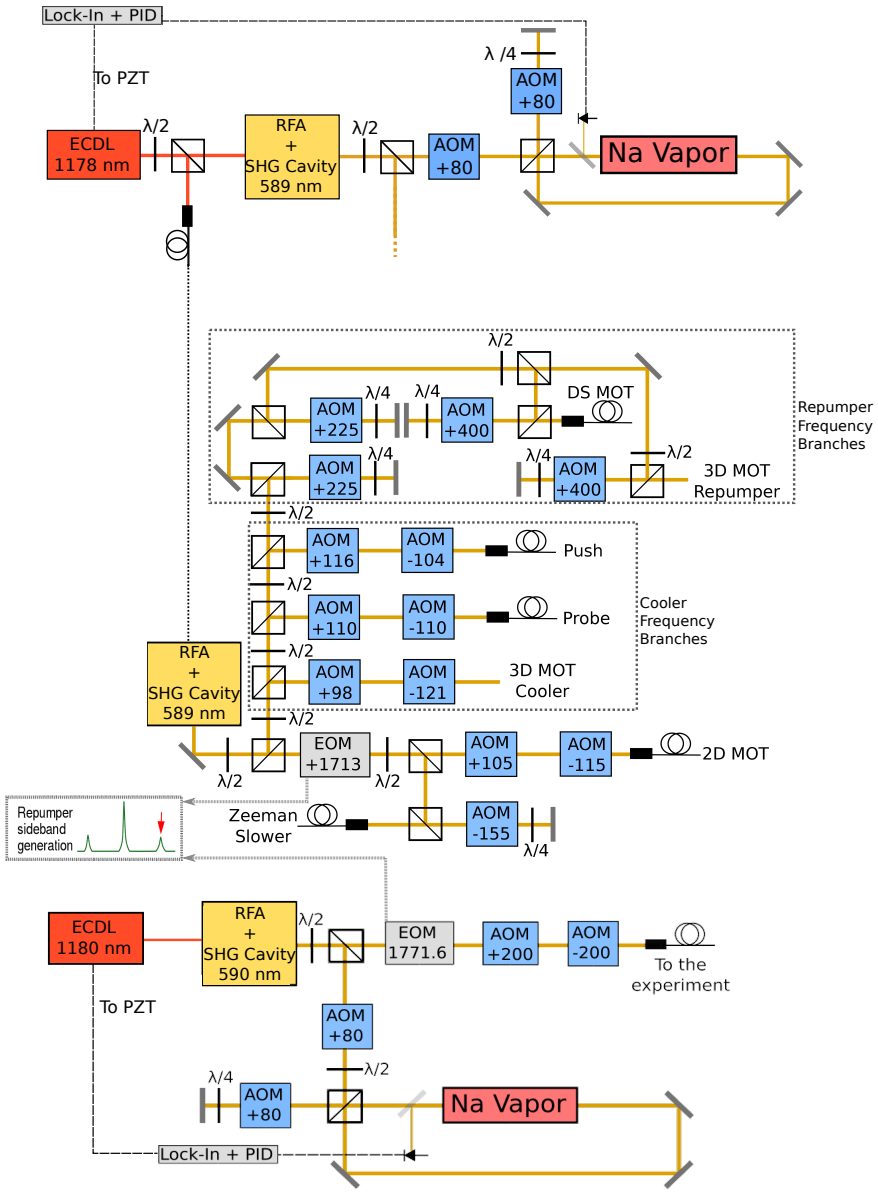

Figure 2.5: Sketch of the complete laser cooling system.

1178 nm laser signal, that is available through solid-state-based technology. Our composite laser source then consists of a homemade frequency-tunable *External-cavity diode laser* (ECDL), referred to as *master laser*, amplified by means of a commercial *Raman fiber amplifier* (abbreviated RFA, model RFA-P-8-1178-SF) sending up to 8 W of power in a second harmonic generation stage. Such a frequency doubling stage consists of a 15 mm LiB_3O_5 nonlinear crystal located in a bow-tie cavity, which is stabilized by means of polarization spectroscopy [95]. Output powers as high as 4.5 W can be generated in this configuration operating the RFA at full power.

The source output frequency is defined by the emission frequency of the master ECDL laser. Such a device is based on the design proposed in [96]. The active element is provided by an Innolume GC-1178-TO-200 gain chip. The output facet of the diode is anti-reflection coated to avoid double cavity effects. The diode emission is collimated by means of an aspheric lens (Thorlabs C340TME-B) and propagates to a reflective holographic grating in Littrow configuration, which also acts as cavity output coupler. Polarization is purified inside the cavity by means of a polarizing element. The emission frequency is controlled acting on the grating position: tuning on a large scale is achieved by means of a screw fixing the grating position while a finer scale tuning by acting on the operating current and temperature of the diode. Precision control, necessary for frequency stabilization, is achieved by applying a voltage to a piezoelectric crystal on which the grating is mounted.

2.3.2 Optical setup

Both D1 and D2 laser systems are located on dedicated optical tables separated from the experiment table hosting the vacuum chamber, as sketched in Fig. 2.5. Both sources are frequency-stabilized on the respective cooler transition by means of FM saturated absorption spectroscopy applied on a heatpipe containing sodium. The source outputs are split in secondary beams, independently controlled in frequency and amplitude through RF-driven *acousto-optic modulators* (AOMs), before being sent onto the experiment table hosting the vacuum chamber through polarization maintaining optical fibers (Schäfter + Kirchhoff PMC-630-4.2-NA12-3-APC-). Fiber injection can be completely inhibited via electronically-controlled mechanical shutters. This allows for the complete suppression of stray resonant laser light in the science chamber during the later stages of the experiment, that would otherwise induce additional heating and losses on the atomic sample. The ground state hyperfine splitting of sodium is $h \times 1771.6$ MHz. As a consequence of this, repumper signals can be efficiently generated as frequency sidebands through phase-modulation using micro-wave driven *electro-optic modulators*. The driving signal for each EOM is generated by means of a Marconi Instruments 2024 generator, then amplified. Less efficient double-pass configuration AOMs in cascade are used instead where independent manipulation of repumper laser light is required. Usually, AOMs operating at lower frequencies are characterized by a larger active area. Therefore, whenever one needs to use several of them in cascade, it is more convenient to use lower frequency AOMs first followed by higher frequency ones. In this way it is possible to avoid too high intensities. This was taken into account in the optical setup, as shown in Fig. 2.5

2.4 Magnetic fields and RF antenna

Control of the magnetic field environment is of pivotal importance in ultracold atoms experiments. Low intensity magnetic fields induce on the atoms an m_{F}-dependent Zeeman energy perturbation $\Delta E = g_{\mathrm{F}} \mu_{\mathrm{B}} m_{\mathrm{F}} |\vec{B}|$, where g_{F} is the Landé g factor and μ_{B} is the Bohr magneton. As discussed in Chapter 1 with reference to coherently coupled

two-component BECs, and in Chapter 3 with reference to GM cooling, stray magnetic fields induce decoherence in Rabi-coupled internal states. On the other hand properly implemented space-dependent magnetic fields are necessary both for laser cooling techniques, such as ZS and MOTs, where they induce a position dependence on to the near-resonance photon scattering rate, and for conservative magnetic trapping. In the experiment I am describing, magnetic field intensities generated in close proximity of the μ-metal shield are bounded by its saturation limit. Such limit is compatible with MOT operation and bias magnetic field control due to the relatively low required values of magnetic fields and gradients. On the other hand such limit relegates conservative magnetic trapping to a support role with regards to production of quantum-degenerate samples. Taking this into account, we opted for the simplest possible magnetic coils configuration, as described in next subsections. The test configuration here described favors flexibility and the preservation of full optical access, over the compactness required for fitting all the elements inside the magnetic shield. A permanent configuration, geometrically compatible with the shield, will be designed according to the results presented in this thesis work as well as on the simulations concerning the magnetic shield saturation limits shown in [40]. Two kinds of elements produce magnetic fields necessary for the experiment:

- **Permanent Magnets** Magnetic field gradients to operate the atomic source, are obtained by means of four stacks of permanent neodymium bar magnets (Eclipse N750-RB). Their configuration in the context of atomic source operation is described in 2.6.1. Each stack is made of 9 magnets measuring 10x25x3 mm^3 each. The magnetization of a single magnet amounts to $8.7(1) \times 10^5$ A/m along the shortest direction. Since the magnets are relatively far from the science chamber and the generated magnetic field intensity falls off rapidly with distance, no compatibility issue with the magnetic shield is expected.

- **Magnetic Coils** The simplest configuration to produce either quadrupole field gradients or a homogeneous magnetic field in a given direction consists of a pair of coaxial twin coils. In Helmholtz configuration (with currents flowing in the same direction rotation-wise) constant magnetic fields proportional to the current are produced. In the anti-Helmholtz configuration (currents flowing in opposite directions), a quadrupole magnetic field is generated instead. Control over the bias field is necessary to compensate for external magnetic fields during GM cooling, keep the atomic sample polarized, and to translate the quadrupole magnetic trap potential. Quadrupole field gradients are needed to operate the MOT and for weak magnetic trapping. The magnetic coil configuration is described in next (2.4.1) subsection.

2.4.1 Magnetic coils description

Quadrupole Magnetic Coils The pair of coils (represented in blue, see Fig.2.6), that are used to produce magnetic field gradients, are operated in anti-Helmholtz configuration. The coils are distanced by 43 mm, and each is made of 49 windings of 0.8 mm

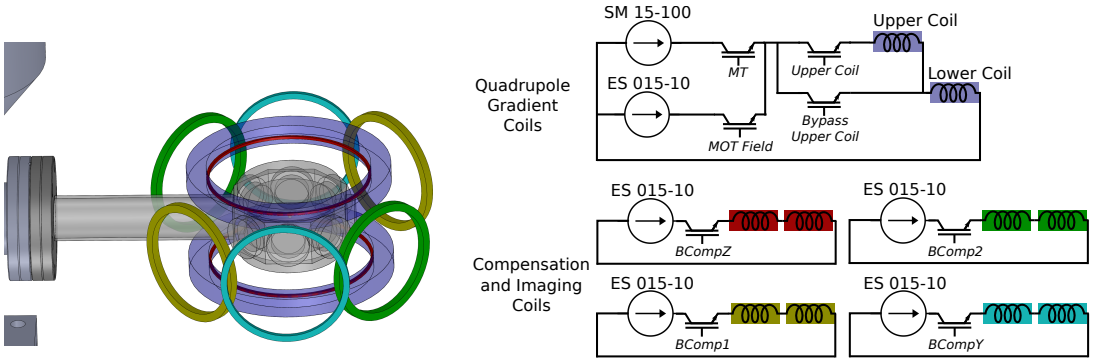

Figure 2.6: Magnetic coils configuration (left image) and relative control circuit (right image). Coils are color-coded according to their function.

radius copper wire. The coils inner radius is about 46 mm. Three different configurations can be set by TTL-controlled IGBT switches (Semikron SKM150GAL12T4 and SKM400GAL12E4):

- **MOT:** during MOT operation, both coils are supplied by a Delta Elektronika ES 015-10 power supply, capable of supplying up to 10 A. The current output is externally programmed through a DAC-controlled voltage.
- **Quadrupole Magnetic Trap:** the configuration for magnetic trapping is analogous to the MOT configuration, but the coils supply switches to a Delta Elektronika SM 15-100 power supply, capable of up to 100 A current and 15 V output. The maximum current output is limited to about 25 A by the voltage drop on the IGBTs and on the circuit resistive load. Such value is above the operative value required for BEC production in our hybrid trap, of the order of 10 A. Both current and voltage output values are externally programmed. Adjusting the voltage limit is useful to minimize the switch-on time of the MT, while avoiding current overshots, when switching on abruptly the trapping potential at a given current value.
- **Levitation:** in order to compensate the gravitational force (for atoms in the $m_F = -1$ state) without inducing trapping effects on the sample, the upper coil is bypassed and the lower coil is operated at about 9.2 A. A magnetic field of the order of 4.6 G/A is produced at the atoms location, in this configuration.

The magnetic field gradients per current unit generated on the atoms, in MOT and MT configurations, is 2.21 G/(cm A) along the symmetry axis of the coils system. Such value was estimated through levitation trajectories, assuming coil symmetry and taking into account Breit-Rabi second-order contributions.

Compensation and Imaging coils These coil pairs are operated in Helmholtz current configuration to control the magnetic field value on the atoms.

- **Compensation/Bias** Three pairs of coils are used to control a bias constant field on three orthogonal axes. Coils are oriented as in Figure 2.6. Coils to generate the compensation field in the vertical direction consists of 6 windings of 0.54 mm radius copper wire. They are distanced roughly 50 mm and have a radius of about 45 mm. Compensation coils for horizontal field components are realized by 42 windings of 0.54 mm radius copper wire, are distanced about 150 mm and have a diameter of roughly 60 mm.

- **Imaging coils** A pair of coils to generate a field component in the propagation direction of the σ-polarized horizontal probe beam. Such 65 mm diameter coils consist of 10 windings of 0.54 mm diameter copper wire, distanced about 150 mm.

2.4.2 RF antenna

Magnetic traps, in contrast to ODTs, are characterized by an intrinsically large capture volume and a significant trap depth, of the order of the mK. An atomic sample with a temperature of the order of 50 µK typically explores only a small fraction of such a volume. Limiting the trap depth of such a potential in an experimentally controlled way is necessary to remove high-energy atoms, either to perform evaporative cooling on the sample, or to simply stabilize its temperature against heating effects. Such a result is achieved by RF-induced magnetic dipole transitions to untrapped Zeeman states. Atoms crossing the equipotential surface defined by the RF transition resonance condition can in this way be expelled in an energy-selective way. The RF signal is generated by means of an antenna made of copper wire of radius 0.8 mm, winded in a single loop of 40 mm diameter. The antenna is located in close proximity to the octagonal cell upper window. It is driven by an amplified RF signal, generated through an RF slave board. Mode-matching in the frequency region of interest (below 10 MHz) is improved by means of a capacitor in series with a 50 Ω resistor. The value of the capacity was chosen to minimize the reflected RF power, probed by means of an RF coupler.

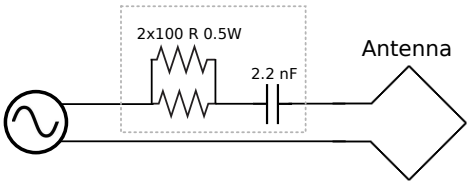

Figure 2.7: Scheme of the mode-matching circuit (boxed in the gray dashed line) connected to the antenna.

2.5 Optical Dipole Trap

Production and study of multicomponent condensates in different Zeeman internal states requires an m_{F}-independent trapping potential. Magnetic trapping is clearly unsuitable for this application, while *optical dipole traps* (ODTs) fulfill such a requirement. Quantum-degenerate atomic samples can be either directly produced in such kind of trap with an all-optical protocol, or transferred to a pure optical trap

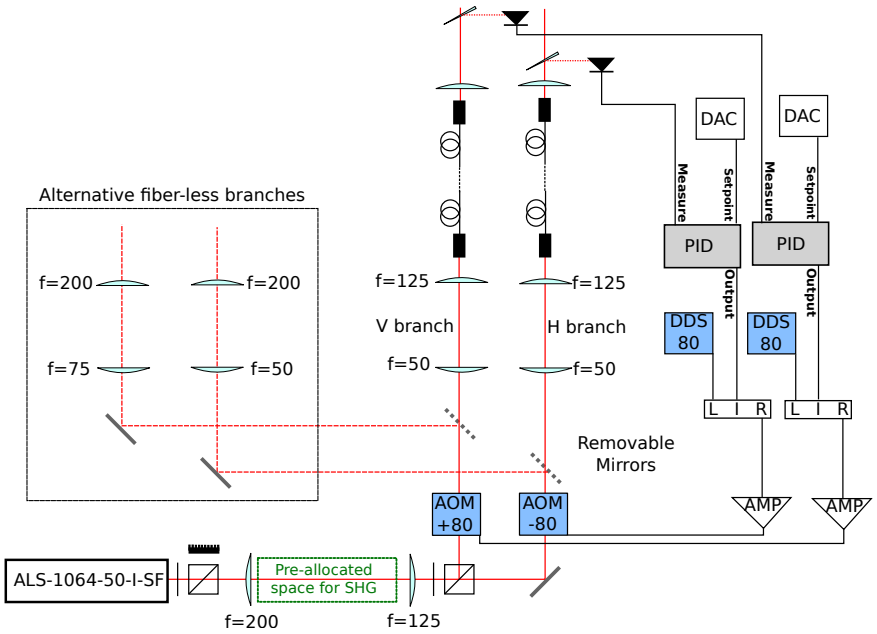

Figure 2.8: Sketch of the ODT apparatus and power stabilization loop.

afterwards, after reaching quantum degeneracy in a magnetic or hybrid trap. While magnetic trapping has several advantages, the experiment is limited by design to low magnetic field gradients, which are unsuitable to provide acceptable thermalization rates during RF evaporation. Initially, all-optical production of BECs was attempted, but directly loading the ODT from GM was found to be inefficient. On the other hand, a hybrid trap in such conditions proved to be a valid and easy-to implement alternative, as discussed in Chapter 4.

A functional sketch of the ODT laser apparatus and its power stabilization loop is given in Figure 2.8. The far-off resonance laser light is produced by means of an Azur Light System laser (ALS-1064-50-I-SF) capable of emitting up to 40 W at a wavelength of $\lambda = 1064$ nm a rather good spatial mode ($M^2 < 1.1$). Its output is collimated to a waist of 0.5 mm by means of a telescope. The beam inside the telescope is focused in the middle of a single-pass 30 mm long SHG crystal (Oxide-PPMgSLT), to a waist of about 60 µm. A preliminary test showed that we are able to generate about 6.5 W of power at 532 nm with such a configuration. After the SHG telescope the beam is split into two branches, labeled *horizontal* (H) and *vertical* (V), and pass through two AOMs, driven at 80 MHz and aligned on opposite diffraction orders. The frequency difference introduced in this way between the two branches prevents interference effects in crossed dipole trap configurations. The AOMs also act as fast switches, as well as actuators in the power stabilization feedback loop.

After magnifying the spot size by a factor 2.5, the beams are injected in photonic crystal high-power optical fibers (NKT-Photonics LMA-PM-10) through $f = 20$ mm lenses acting as fiber collimators. Each branch can be rerouted to a fiber-less path, directed to the atoms. Such branches were used to test several temporary trap configu-

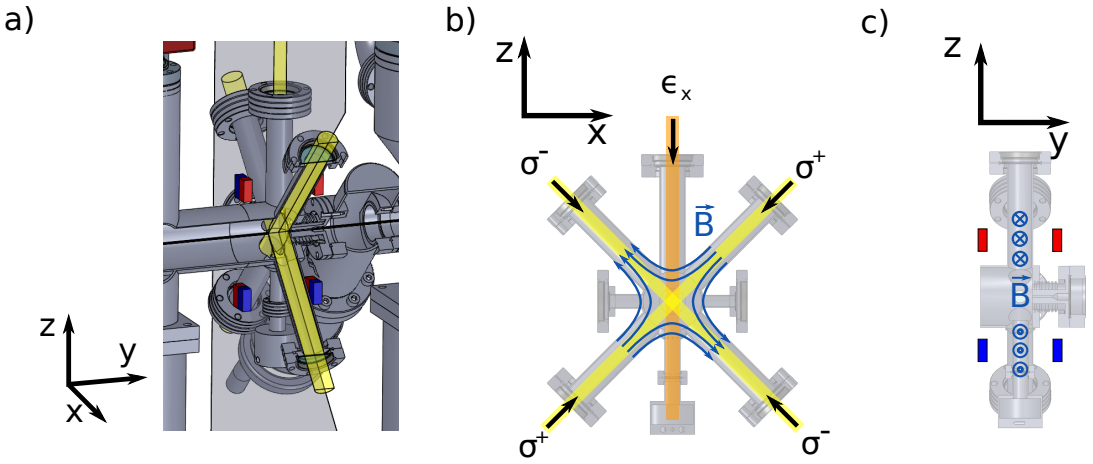

Figure 2.9: **a)**Section view of the atomic source, showing the permanent magnets position and orientation (N:red, S:blue) **b)** Sketch of the atomic source plane, showing polarizations of the 2DMOT beams (yellow) and ZS(orange), as well as the in-plane 2DMOT quadrupole magnetic field configuration (light blue) **c)** Magnets orientation and corresponding magnetic field configuration along the ZS beam propagation axis.

rations without being limited in the total amount of power by the fibers injection loss, as discussed in Chapter 4. A small fraction (about 0.25%) of the power of each branch is reflected by a round wedge prism (Thorlabs PS810-B) on a photodiode (Thorlabs DET36A/M). The measured photocurrent is compared to the DAC-controlled setpoint by means of a commercial PID, whose output modulates in amplitude the RF signal driving the AOM through an RF mixer (Minicircuits ZLW-1-1+).

The H branch is currently used in the final hybrid trap configuration, described in Chapter 4. At the fiber output, after being collimated to an approximate waist value of about 3.2 mm, the beam is focused on the atoms through an $f = 200$ mm achromatic lens, to a waist of 23 µm.

2.6 Atomic source and MOT operation

2.6.1 Atomic source

The atomic source design is based on the one originally proposed in [97], and already implemented with sodium [98] and strontium atoms [99]. As sketched in Fig. 2.9, atoms evaporating from the oven (operated at 243 °C, about 145 °C above sodium melting point) are slowed by a compact (12 cm long) ZS stage after which atoms are transversely loaded in a 2DMOT. The 2DMOT free axis coincides with the DP axis, and captured atoms are pushed through the DP channel by means of a dedicated push laser beam. Such a configuration, other than being geometrically compact, prevents direct exposure of the UHV side of the chamber to the atoms

effusing from the oven. In addition to this, two-dimensional trapping reduces collisional losses of trapped atoms, contributing to increase the source output flux. The permanent magnet stacks described in 2.4 are fixed as shown in Fig. 2.9, with centers at a vertical distance of about 97 mm and a horizontal one of about 67 mm .

The ZS laser beam is a linearly polarized 2.5 cm diameter beam, propagating against the flow of hot atoms evaporated from the oven. Its frequency is red-detuned from the D2 cooling transition by $34\,\Gamma$, where $\Gamma = 2\pi \times 9.795$ MHz is the D2 transition natural linewidth (taken as $\Gamma = 2\pi \times 10$ MHz for simplicity). Its total intensity is $25.2\,I_{\rm sat}$ in units of the D_2 saturation intensity for $\sigma^{\pm}$ polarized light $I_{\rm sat} = 6.26$ mW/cm^2. Such intensity is distributed in frequency between the cooler carrier (about 50%), the repumper(upper) sideband generated by the EOM (about 25%), and a non resonant (lower) sideband (about 25%). It must be also taken into account that the ZS magnetic field, is aligned along the horizontal direction and is perpendicular to both the DP axis and the propagation direction of the ZS laser beam. This reduces the effective ZS beam intensity by a factor 2, in the best case, corresponding to the σ-polarized fraction of the radiation.

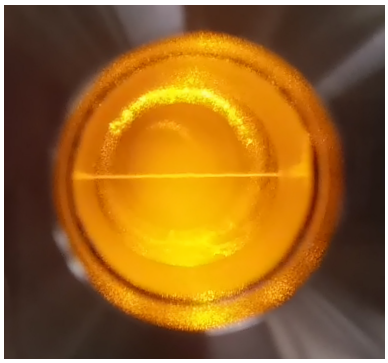

Figure 2.10: Sodium atoms captured in the 2DMOT, as observed from a side viewport of the atomic source.

Two retro-reflected 2.5 cm diameter wide laser beams are used to operate the 2DMOT. Counter-propagating beams are $\sigma^{\pm}$-polarized in opposite directions according to the local magnetic field direction, as shown in Fig. 2.9. Such laser beams are red-detuned from the cooling transition by 1.3 Γ and a total average intensity of about 1.4 $I_{\rm sat}$ per beam is sent on the atoms. Their spectral composition is the same as the ZS beam one. The push laser beam propagates along the chamber main axis and is collimated, in the 2DMOT region, to a waist of the order of 115 µm by means of a long focal length lens ($f = 500$ mm). Atoms, accelerated through the DP channel travel past the cell connection tube and are collected by the 3D DS-MOT.

2.6.2 Dark-spot MOT

DS-MOT configuration was introduced in [100] as a method to improve the density of magneto-optically trapped atoms. Density limiting effects are caused both by two-body collisions involving atoms in the excited states [101, 102], and by re-absorption of spontaneously emitted photons inside the sample, which gives rise to an effective atom-atom repulsive force [103]. To cope with such effects while retaining a functioning cooling protocol, atoms are repumped from the $|F_g = 1\rangle$ manifold by means of a hollow-profile beam. In this way colder atoms, accumulating in the central region of the MOT, are optically pumped in the $|F_g = 1\rangle$ manifold, which is a dark state for the cooling light. Such a hollow beam profile is obtained, as shown in Fig.2.11, by sending a

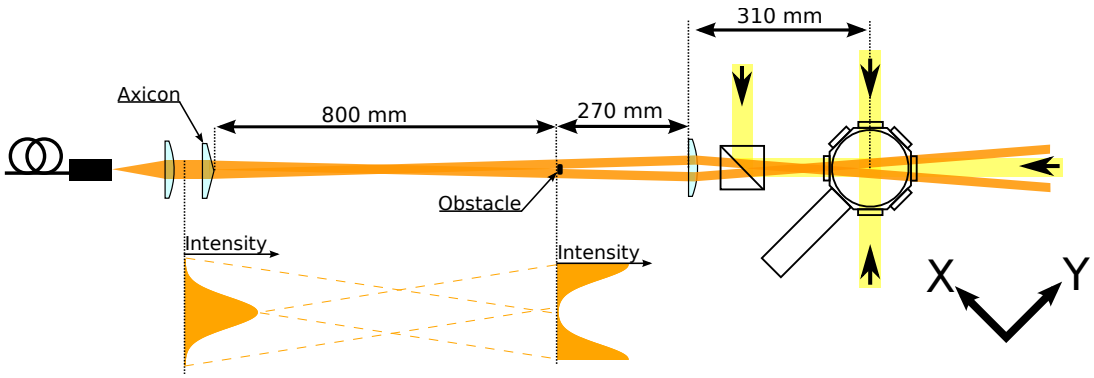

Figure 2.11: Schematic representation of the optical apparatus, that is to produce the hollow repumper beam needed to operate the MOT in dark spot configuration. MOT cooler beams are represented in yellow, the repumper DS beam in orange.

collimated Gaussian beam through an axicon lens (Thorlabs AX252-A) to invert the inner (higher intensity) and the outer (low intensity tails) parts of the beam profile. After 800 mm of propagation, the beam profile presents itself as a bright annular band with intensity increasing in the outward direction, with a dark circular region (about 6 mm diameter) at the center. Residual light in this region is blocked by means of a disk-shaped obstacle before imaging such beam profile on the atoms. The cooler MOT beams consist of six uniform intensity beams with a diameter of about 19 mm. These beams counter-propagate in pairs orthogonal to each other on the atoms, with opposite $\sigma^{\pm}$ polarization. The horizontal propagation axes are rotated by 45° compared to the main (push beam) axis of the chamber. The DS repumper beam is superimposed to one of these beams by means of a polarizing beamsplitter cube. The quadrupole magnetic coils in MOT configuration are operated with a current value of 6 A, generating a gradient of 13.3 G/cm on the atoms.

2.6.3 Parameter optimization

Optimization of the atomic source experimental parameters was carried out with the aim to optimize the flux of atoms effectively captured by the MOT. Such quantity is a fraction of the total flux from the atomic source, roughly corresponding to an intermediate velocity interval - slower than the maximum capture velocity of the MOT, faster than the minimum velocity required not to fall outside the MOT region while passing through the cell connection tube. The growth rate of the MOT fluorescence signal, during the initial 0.25 s of loading, is used to quantify such flux, and is collected by means of a Thorlabs PDA-100A-EC photodiode. Taking advantage of earlier characterizations reported in an analogous sodium experiment [98], I first set the experimental parameters to values suitable for observing a loading signal, then I optimized the permanent magnets position and the geometrical beams alignment. After this, I turned to the optimization of the parameter values. Values of the fluorescence

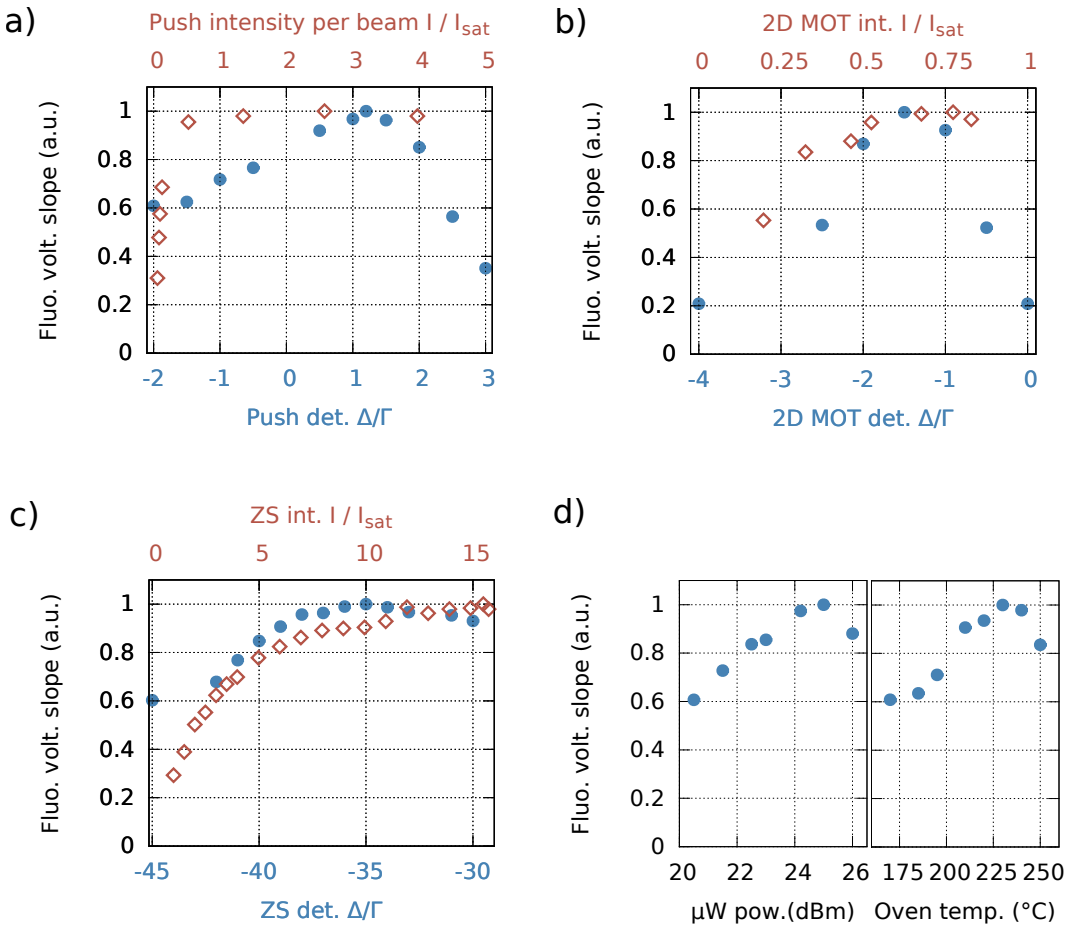

Figure 2.12: Optimization steps for the fluorescence growth rate, as a function of push **(a)**, 2DMOT **(b)** and ZS **(c)** detuning (blue filled circles) and intensity (red empty diamonds), and as a function of EOM driving power and oven temperature **(d)**. Both fluorescence growth rate and atom number values are given in arbitrary units to compare the qualitative behaviors.

slope are shown in Fig. 2.12(a-d) as a function of the atomic source parameters. Such values were taken during a first optimization cycle and are given in arbitrary units for better comparison. Then I maximized the saturated number of atoms loaded in the DSMOT (Fig. 2.13(a,b)) changing the MOT parameters. The atom number was quantified by means of absorption imaging (see Section 2.7). The final set of values, obtained after iterating the optimization cycle, is reported in Table 2.1. Figure 2.13(c) shows the number of captured atoms in the DSMOT as a function of loading time with such optimal values. More than 5×10^9 atoms are loaded in 13 s. The temperature estimated by *time of flight* (TOF) characterization is of the order of 300 μK. The corresponding loading rate is quantified by the leading slope during the first $1-2$ s, as 0.6×10^9 atoms/s. No effort was made to optimize the MOT final temperature since

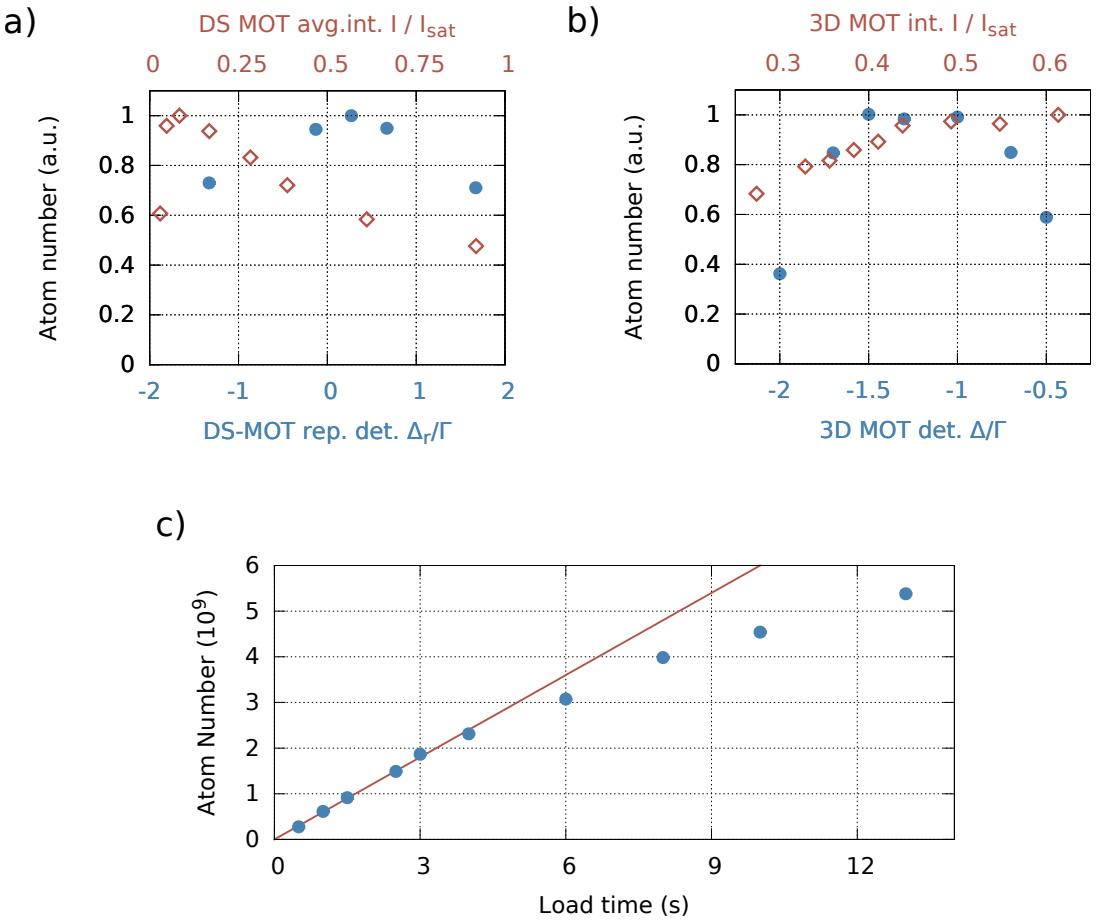

Figure 2.13: Number of atoms (in arbitrary units) loaded in in DS-MOT , as a function of the DSMOT **(a)** and 3DMOT **(b)** beams detuning (blue filled circles) and intensity (red empty diamonds). The average intensity of the DSMOT is estimated dividing the total power by the the annular surface of of the beam (4 cm^2). **(c)** Number of atoms captured in the 3DMOT as a function of time (blue dots), with optimal parameter values. After a time of 13 s the number saturates to more than 5×10^9 atoms. The dark-red line corresponds to a constant loading rate of 0.6×10^9 atoms/s.

further cooling is efficiently achieved by means of GM.

2.7 Imaging system and procedures

The imaging system is based on absorption imaging (see for instance [104]). In near-resonant conditions (where refractive contributions can be neglected), a weak ($I_p \ll I_{sat}$) probe laser beam propagates through a dilute atomic sample, whose integrated

	$I/I_{\rm sat}$	Δ/Γ	$B'_{\rm z}$(G/cm)
ZS cooler	12.6(*)	-34	-
ZS repumper	6.3 (*)	(**)	-
2DMOT cooler	0.7	-1.3	-
2DMOT repumper	0.35	(**)	-
Push	3.3	1.2	-
3DMOT cooler	0.37	-1.7	-
DS	0.07(***)	-0.15	-
MOT coils gradient	-	-	13.3

Table 2.1: Final set of operation parameters for the 2DMOT and DS-MOT. Average intensity per beam in unit of the D2 cooling transition saturation intensity $I_{\rm sat} = 6.26$ mW/cm^2, and detunings Δ from the relevant transition (cooler or repumper) in units of the sodium natural linewidth $\Gamma \simeq 2\pi \times 10$ MHz
(*) Effective intensity, corresponding to the σ polarization component of the beam, is expected to be half of the reported total value.
(**) Repumper sideband shifted by +1713 MHz from the cooler frequency
(***)Average intensity estimated as 1.8 mW total power divided by the annular surface of 4 cm^2.

column density is $\bar{n}(y,z)$, with a decaying exponential law:

$$I(y,z) = I_{\rm p}(y,z)e^{-\mathcal{O}(y,z)} = I_{\rm p}(y,z){\rm Exp}\left[-\bar{n}(y,z)\frac{\sigma_0}{1+4(\Delta_{\rm p}/\Gamma)^2}\right], \tag{2.1}$$

where $\Delta_{\rm p} = \omega_{\rm L} - \omega_{\rm eg}$ is the probe detuning from resonance and $\sigma_0 = 3\lambda^2/(2\pi)$ is the resonant absorption cross-section. The imaging procedure consists into transferring all the atoms occupying the $F_{\rm g} = 1$ manifold to the $F_{\rm g} = 2$ ground state by shining a repumper light pulse along the six MOT beam directions. A pulse of 40 µs duration, applied 170µs before the probe pulse, is usually sufficient to transfer all the atoms, except for large and optically thick clouds, in which case the repumper pulse duration is increased as necessary. The atomic sample is then illuminated with probe light, whose profile is then imaged on the detector camera, while TTL signal triggers the data acquisition and defines the integration time of the camera. An image of the probe beam profile in absence of atoms and a background image without probe nor atoms are then acquired, from which the optical density $\mathcal{O}$ (hence, the atom column density) can be extracted by means of a dedicated software as:

$$\mathcal{O}(y,z) = -\ln\left[\frac{I_{\rm p}(y,z) - I_{\rm bg}(y,z)}{I(y,z) - I_{\rm bg}(y,z)}\right]. \tag{2.2}$$

Two different cameras can be used to simultaneously take pictures along the horizontal and vertical imaging directions. The horizontal imaging can be switched, by means of a removable mirror, to a higher magnification imaging branch that was recently implement for preliminary tests on a *dark-ground* (DG) imaging protocol. Cameras used for image acquisition are *charged-coupled device* (CCD) cameras (Stingray F-201B), which offer a resolution of 1624×1234 pixels and 4.4×4.4 µm pixel size. Magnification values are 1/2.6 and 1/2.5 for the horizontal and vertical de-magnifying imaging respectively. The alternative horizontal imaging magnification is 2.

TOF imaging is performed by releasing the atoms in free fall, and taking an image after a given ballistic expansion time. Such expansion time is limited either by the time required by the falling sample to exit from the region sampled by the horizontal probe beam, that is less than 30ms, or by the time needed to reach the bottom of the cell (roughly of the same order of magnitude), relevant for vertical imaging. Fitting is then performed by means of a suitable Python software (adapted from a version originally written by Dr. Gregor Thalhammer), by which relevant parameters of the distribution are extracted. For high values of the optical density ($\mathcal{O} \sim 2-3$) the signal from the camera saturates and little information can be extracted. When dealing with large thermal clouds such saturation effects can be dealt with by increasing the probe light detuning to reduce atom-light interaction (equation 2.2). As mentioned before, in case of optically thick clouds the repumper pulse duration or intensity could be insufficient to repump all the atoms before imaging. In this case, instead of a saturated density profile as observed in the case of saturated probe absorption, the column density profile appears hollow for short expansion times. This happens as a consequence of repumping taking place only in the external shell of the cloud.

The temperature of a freely expanding thermal cloud can be estimated by measuring the cloud size at different times:

$$\sigma^2_{\mathrm{x,y,z}}(t) = \sigma^2_{\mathrm{x,y,z}}(0) + \frac{k_{\mathrm{B}}T}{m}t^2, \tag{2.3}$$

where $\sigma_{\mathrm{x,y,z}}$ and $\sqrt{k_{\mathrm{B}}T/m}$ are the r.m.s. size and velocity of the sample, respectively.

From TOF measurements in free fall we can extract little information on Bose-condensed samples, owing to their low expansion velocity and high optical density. Reducing image saturation effects by increasing the probe light detuning, when dealing with small and dense samples, results in strongly degraded images due to refractive lensing effects [105].

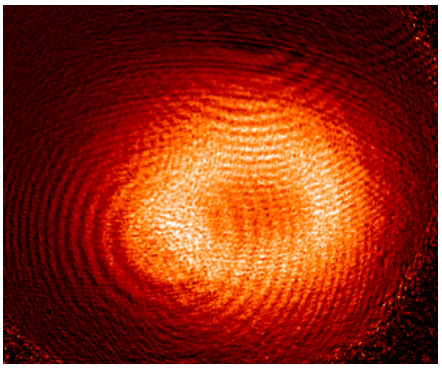

Figure 2.14: Imaged profile in the case of saturated repumper light.

In order to increase the possible expansion time of the sample up to hundreds of ms, the quadrupole magnetic coils are switched to the levitation configuration, as discussed in section 2.4. After a suitable levitation time, resonant absorption images are taken with the same procedure described for the free-fall case. As described in Chapter 1, mean-field interactions considerably alters both the expansion dynamics

and the in-trap distribution compared to thermal samples [106].

Chapter 3

Sub-Doppler cooling of Sodium atoms in Gray Molasses

***

In this chapter I describe the successful implementation and characterization of *gray molasses* (GM) cooling of sodium atoms. After a general introduction, which is given in the first section, the experimental results [107] concerning such implementation of GM cooling are discussed in the second section. These results were obtained in another sodium-based experimental apparatus [98], that can be regarded as equivalent to the one described in Chapter 2 in the context of this chapter. It was used as a testbed for the cooling protocol while the buildup of the new apparatus was at a premature stage. Implementing GM cooling in the new apparatus was straightforward relying on the previous characterizations.

3.1 Introduction

3.1.1 Brief remainder on sub-Doppler cooling

Sub-Doppler laser cooling techniques, [108], are based on a combination of polarization-gradient induced light shifts with optical pumping in order to induce an efficient cooling

mechanism [109, 110] on an atomic sample, allowing to reach temperatures below the Doppler limit $T_{\mathrm{D}} = \hbar\Gamma/2k_{\mathrm{B}}$, where $\hbar$ is the reduced Planck constant, Γ is the natural linewidth and k_{B} is the Boltzmann constant. Two possible field configurations (lin$\perp$lin or $\sigma^+ - \sigma^-$) allow for such cooling effects. Regardless of the different specific cooling mechanism in the two cases, as discussed in the given references, quantities of practical interest scale in a similar way with the experimental parameters and allow to reach comparable results.

Sub-Doppler cooling is effective in a limited velocity capture range, and usually follows a suitable Doppler pre-cooling stage. The interaction strength with the light field determines such a capture range, that results proportional to the laser intensity I, and reduces for higher values of the radiation detuning Δ. Ordinary techniques require degenerate Zeeman sublevels and red-detuned laser light ($\Delta < 0$) to optically pump the atoms in lower energy states (reducing their kinetic energy), enabling to combine Doppler and sub-Doppler cooling in an optical molasses scheme.

The lowest kinetic energies that can be reached by means of sub-Doppler cooling are of the same order of the light energy shifts induced by the polarization gradients, $\propto I/\Delta$ in the simple two-level approximation, to a minimum value which is set, in principle, by the single photon recoil energy. The corresponding temperature is $T_{\mathrm{rec}} = \hbar^2 k_{\mathrm{L}}^2/mk_{\mathrm{B}}$ (where k_{L} is the wavenumber and m is the atomic mass). Such a value amounts to $T_{\mathrm{rec}} = 2.4\ \mu$K for sodium atoms. Techniques relying on different mechanisms, such as Raman cooling [111], are required to achieve sub-recoil temperatures. Temperature values that can be reached in practical situations by polarization gradient cooling, however, are as high as tens of T_{rec}. The first limiting factor are heating effects caused by photon scattering, which are an intrinsic feature of laser cooling mechanism itself. In addition to this, the cooling efficiency can be limited by the specific level structure of the considered atomic species. In the case of sodium, the dense hyperfine structure of the D2 transition and the requirement of red-detuned radiation, introduces spurious off-resonant coupling to the lower energy hyperfine states and an effective limit to acceptable values of the detuning, which may result in worse performances, especially for optically thick samples.

3.1.2 Dark states and velocity-selective coherent population trapping

Dark states, that in the broader sense refer to states which do not couple with the radiation field, are a well-known resource to cope with the heating and density-limiting effects related to light scattering. Taking advantage of open transitions, atoms can be optically pumped to a dark atomic state, where they are protected from such effects, while retaining a functional cooling protocol. Examples of this approach include the already mentioned DS-MOT [100], and schemes where such pumping is dynamically controlled in time, as in [112]. Cooling techniques based on the phenomenon of *coherent population trapping* (CPT) [113, 114], on the other hand, exploit dark states which are characterized by quantum interference effects. The additional advantage of such kind of states is that they allow to devise cooling protocols which are intrinsically velocity-selective. For a proper laser field configuration, each atom remains trapped in a dark state, where it is preserved from light scattering, only if its own velocity is in a narrow

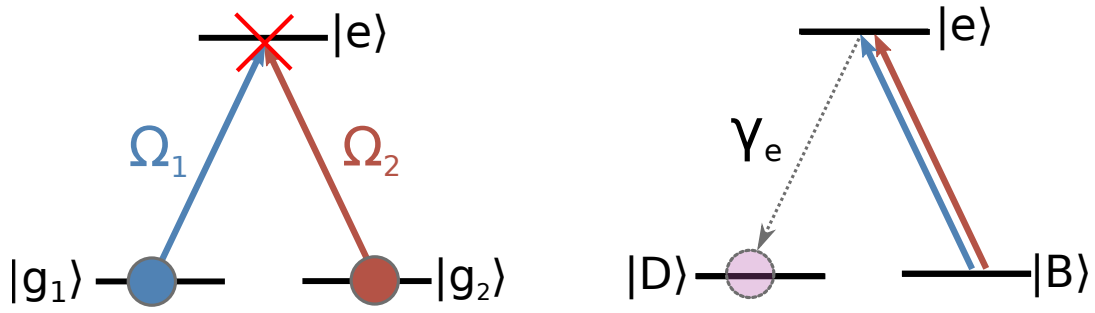

Figure 3.1: Minimal three level structure exhibiting CPT. Atoms in the coherent superposition of atomic states defining the dark state (left figure), are uncoupled to the excited state. The dark state is an eigenstate of the system Hamiltonian (right figure) and is populated by spontaneous emission.

region (e.g. steady in the laboratory frame), while atoms outside such a velocity interval keep interacting with light.

The relevant physics of CPT is captured in the semiclassical framework by a three-level atomic model with a Λ level structure. Neglecting atomic motion, when both ground states of such a system are Rabi coupled with the excited atomic state (as in Figure 3.1), the new eigenstates of the system Hamiltonian are given by coherent superpositions of the three bare atomic states [115]. Remarkably, if the two-photon (Raman) resonance condition between the two driving fields is fulfilled, ($\Delta_1 - \Delta_2 = \delta = 0$), one of such states

$$|D\rangle = \frac{\Omega_2}{\sqrt{\Omega_1^2 + \Omega_2^2}} |g_1\rangle - \frac{\Omega_1}{\sqrt{\Omega_1^2 + \Omega_2^2}} |g_2\rangle , \tag{3.1}$$

is completely decoupled from the excited state $|e\rangle$, such that $\langle e| \hat{\mathcal{H}}_{\text{int}} |D\rangle = 0$. Such a state is referred to as the dark state. The other two eigenstates of the Hamiltonian are given by coupling-induced superpositions of the bright ground state $|B\rangle \perp |D\rangle$ with the excited state. $|D\rangle$ is a stationary state for the system, and is populated by spontaneous emission after a few excitation cycles. As a consequence of this, absorption and refractive properties of the medium are suppressed. Such a mechanism is also referred to as *electromagnetically induced transparency* (EIT).

The atomic motion was neglected in the derivation of $|D\rangle$. Velocity-dependent coupling with the bright state is induced by the kinetic term of the Hamiltonian, which in general is not diagonal in the atom-light Hamiltonian eigenbasis, $\langle B| \hat{\mathcal{H}}_{\text{kin}} |D\rangle \neq 0$. Such a coupling term is proportional to the atomic momentum [116]:

$$\langle B| \hat{\mathcal{H}}_{\text{kin}} |D\rangle = -\hbar k \frac{\Omega_1 \Omega_2}{\Omega_1^2 + \Omega_2^2} \frac{p}{m}, \tag{3.2}$$

where p and m are the atom momentum and mass, and k is the laser wavevector. The transition rate to the bright state (Fermi golden rule), is thus proportional to the square

of the velocity $\Gamma_{D\to B} \propto (kv)^2$, and only atoms with $v = 0$ are completely decoupled from the light field. The first successful implementation of VSCPT cooling [117] allowed to achieve temperatures even below the recoil limit. Such a technique, however, is limited by its reliance on the random diffusion process in momentum space to trap the atoms in the dark state, allowing to cool only a relatively small number of atoms.

3.1.3 Gray Molasses cooling

GM cooling [118–120], combines the advantages related to VSCPT with the efficiency of sub-Doppler cooling mechanisms in terms of cooling efficiency and retained number of atoms. As in ordinary sub-Doppler cooling techniques, atoms move in polarization standing wave field configurations while being optically pumped to a lower energy state. Here, however, such a state is a non-coupling state, ideally unperturbed by light shifts and motionally coupled to the bright states. In contrast with ordinary sub-Doppler cooling, blue-detuned light is required to induce a friction mechanism on the moving atoms. Motional coupling, as discussed before, provides the velocity-selective mechanism: faster atoms in dark states have a higher transition probability to bright states from which the cooling cycle reiterates. Transitions on which GM should be operated, allowing for the existence of dark states, are $|F\rangle \to |F-1\rangle$ or $|F\rangle \to |F\rangle$.

This requirement, in the case of sodium, together with the one of blue-detuned laser radiation, rules out the possibility to exploit the D2 optical transitions for GM cooling. Off-resonant couplings to the $|F_\mathrm{e}\rangle = 3$ manifold would introduce decoherence in the dark states. In contrast, the D1 transition offers a well-resolved level structure with no additional states on the blue side of the cooling transition ($|F_g = 2\rangle \to |F_e = 2\rangle$). For this reason, in order to successfully implement this technique in our experiment, the assembly of the additional D1 laser source described in 2.3.1 was required.

A particularly important point for practical implementation of GM cooling is the $\delta = 0$ Raman condition. For GM operating on the cooler transition, dark states correspond to a superposition of Zeeman degenerate states in the ground hyperfine manifold $F_\mathrm{g} = 2$. Differential energy shifts between these levels, caused by spurious magnetic fields, must be avoided. GM cooling, as VSCPT [117], is extremely susceptible to the presence of such fields. The lowest attainable temperature scales as $T_\mathrm{min} \propto B^2$. This point requires, as discussed in Chapter 2, both to compensate the background magnetic field and to provide some means to switch off MOT magnetic field gradients on the hundreds µs scale. Supposedly, after adding the magnetic shield in the new apparatus, lower and more stable temperature values will be observed.

In the presence of magnetic fields also a different cooling and trapping technique can be devised, if a proper light field configuration is used. Such a technique is referred to as *dark optical lattice* (DOL), [119, 121]. In the presence of a weak magnetic field, the state $|D\rangle$ weakly couples with the excited state, giving rise to a periodic potential ground state structure with minimal light scattering rate in the potential minima. A similar effect is obtained in the regime for which the Zeeman energy shift is higher than the polarization gradient [122]. In such a strong-field regime, the Zeeman degeneracy is lifted such that dark states correspond to m_F eigenstates uncoupled to the light

field due to its local polarization.

Experimental realizations of GM cooling operating on the D2 transition line include ^{133}Cs [123–126] and on ^{87}Rb ([127] and recently [128]) atoms. Cooling of a ^{52}Cr atomic beam in the transverse directions [129] was also reported. In the context of DOLs, early experiments taking advantage of the D_1 transition ($nS_{1/2} \rightarrow nP_{1/2}$) include works with ^{87}Rb [122], and ^{85}Rb [130]. More recent realizations include ^{85}Rb [131], ^{40}K [132,133], ^{7}Li [134], ^{39}K [135,136] and ^{6}Li [133,137], ^{23}Na [107] operating on the D_1 transition. Another realization includes metastable ^{4}He [138].

3.2 Experimental characterization of GM cooling

In this section, the optimization and experimental characterization of GM cooling procedure is discussed. The laser source stabilized on the D1 optical transition is described in 2.3.1. Such a configuration allows to control all the experimental parameters which are relevant to GM cooling (see Fig. 3.2): the total intensity $I_C + I_{rep}$ (cooler and repumper sideband intensity, respectively) and the frequency detuning Δ of the cooler carrier from the corresponding transition ($|F_g = 2\rangle \rightarrow |F_e = 2\rangle$) are directly controlled through the AOMs. Blue detuned light corresponds to positive values of the detuning Δ, in the adopted convention. Relative intensity I_{rep}/I_C and Raman detuning δ of the repumper transition ($|F_g = 1\rangle \rightarrow |F_e = 2\rangle$) sideband signal to the cooler are fixed by the phase modulation signal sent on the EOM. Detuning parameters are given in units of the transition natural linewidth, which amounts to $2\pi \times 9.765$ MHz (here assumed $2\pi \times 10$ MHz for simplicity)

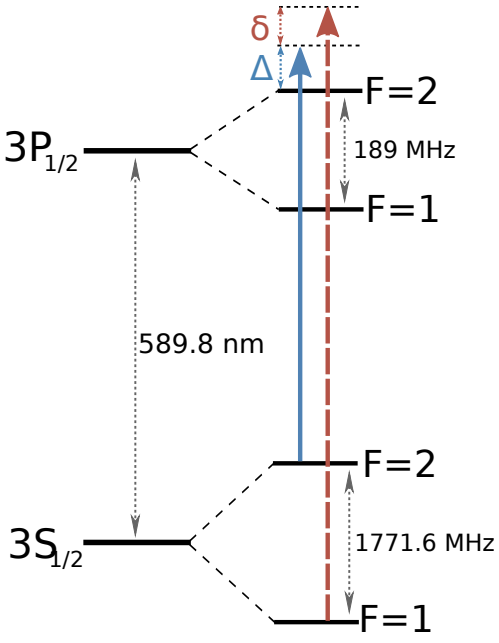

Figure 3.2: Cooler (blue) and repumper (red) of the D1 transition. Detuning parameters Δ and δ, that are used throughout the chapter are shown.

The following characterization was carried out with as much as 200 mW of total power at disposal on the atoms (taking into account power losses on the optical paths). Such amount is split in six beams of 2.3 mm waist (e^{-2} radius) counter-propagating on the atoms in pairs with $\sigma^+ - \sigma^-$ polarizations and directed along three orthogonal directions. The resulting peak intensity on the atoms is about 400 mW/cm^2 per beam.

Before applying GM cooling, 3×10^9 atoms are loaded in a DS-MOT at a temperature of the order of 350 μK. After loading, the atoms are released by switching off the

laser light beams and magnetic fields necessary for MOT operation. Fast switch-off (in approximately 200 µs) of magnetic fields is achieved by means of TTL-controlled IGBT switches. GM cooling sequence is applied right afterwards. External magnetic fields are compensated during the entire procedure with a resolution of roughly 20 mG by means of three pairs of coils in Helmholtz configuration.

Once the GM sequence is completed, absorption imaging is performed in order to estimate atom number and temperature, as described in section 2.7.

An important figure of merit of optical molasses cooling, in addition to the final temperature, is the capture efficiency. Such a value is quantified by normalizing the atom number after optical molasses to the number of atoms loaded in the DS-MOT. Capture efficiency is closely related to the velocity capture interval of the sub-Doppler mechanism, compared to the velocity distribution of the sample. In the specific case of GM cooling, as a consequence of blue detuning, atoms that are not captured in sub-Doppler cooling cycles are expected to be Doppler-accelerated and removed from the sample. The atomic sample temperature is estimated by imaging the expanding cloud at different times to evaluate the r.m.s. velocity of the sample using equation 2.3. The PSD of the sample, right after GM stage, is calculated as $\mathrm{PSD} = n_{\mathrm{p}}\lambda_{\mathrm{T}}^3$, where λ_{T} is the thermal de Broglie wavelength, and n_{p} is the estimated peak density of the *in-situ* distribution, assumed Gaussian for simplicity.

3.2.1 Constant intensity pulse

The procedure characterized here consists of a single light pulse, of duration τ, with a constant value of intensity and cooler detuning Δ_{pulse}.

Figure 3.3(a) shows the captured fraction and final temperature as a function of the pulse duration. The sample temperature reduces to a stationary value of $T \simeq 45\ \mu$K in about 0.5 ms, with nearly unitary capture efficiency. Such a fast relaxation dynamics can be explained both as a consequence of the high initial intensity, corresponding to a large value of polarization gradient-induced light shifts, and the relatively low mass of sodium compared to other atomic species, such as rubidium or potassium.

Characterization as a function of the cooler intensity (Fig. 3.3(b)) shows a linear reduction of the capture efficiency, as well as of the final temperature with the reduction of the pulse intensity. This behavior is expected in the framework of sub-Doppler cooling, as a consequence of the fact that both the sub-Doppler velocity capture range and lowest attainable temperature are proportional to the intensity. The intensity value to saturate the capture efficiency of our sample is 350 $\mathrm{mW/cm^2}$ per beam, leading to temperature values of the order of $40 - 50$ µK. On the other hand values as low as $10 - 15$ µK can be reached at low power values, confirming the aforementioned advantages related to operating on the blue side of the D1 line.

As shown in Fig. 3.3(c), the final temperature shows a marked reduction with increasing values of cooler detuning Δ_{pulse} in the region $2\Gamma < \Delta_{\mathrm{pulse}} < 6\Gamma$, consistently with polarization-gradient cooling. Relatively large capture efficiencies are retained in such an interval. For higher detuning values, a further temperature reduction at the expense of capture efficiency is observed, but the measurements in such a region are systematically affected by the reduction of intensity due to the AOMs diffraction

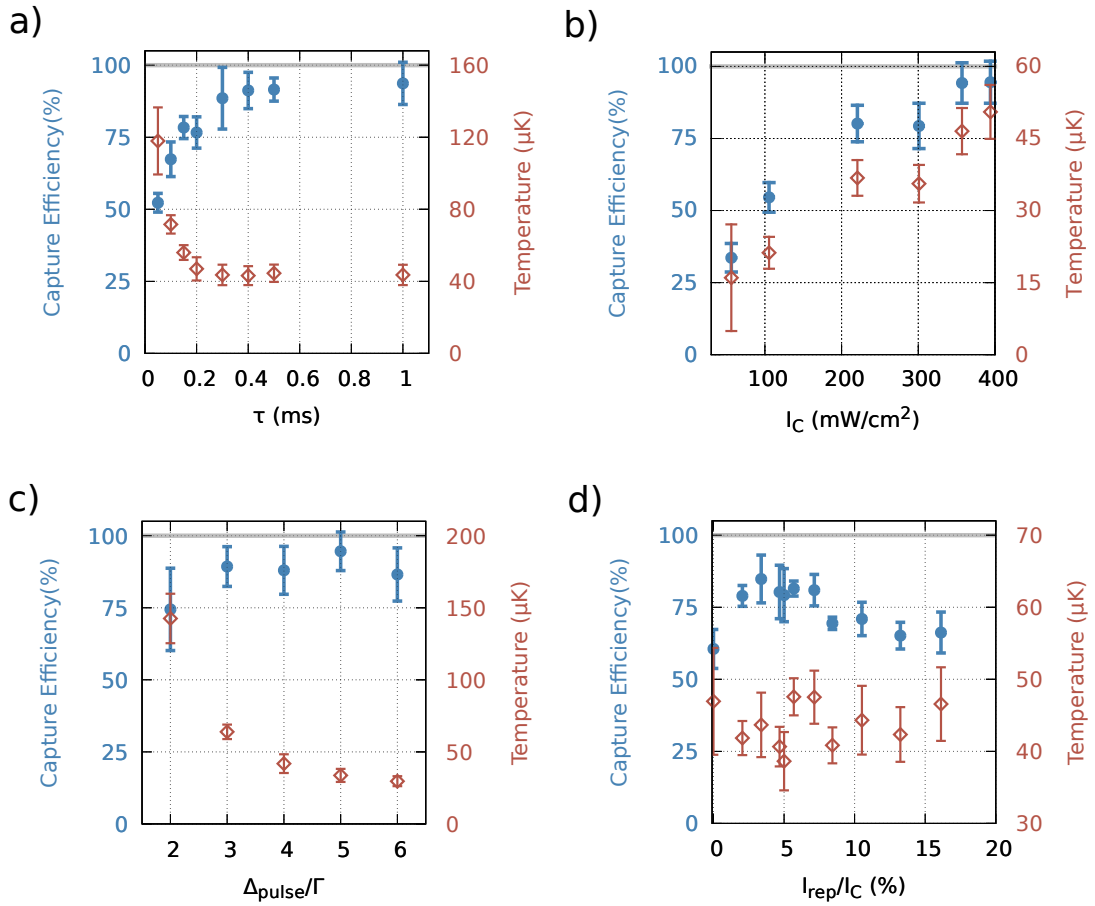

Figure 3.3: Capture efficiency (blue filled circles) and temperature (dark red diamonds) after a GM pulse at constant intensity $I_C = 330$ mW/cm^2 with a fixed value of the detuning $\Delta_{\text{pulse}} = 4\Gamma$, as a function of the duration of the pulse τ **(a)**, as a function of the total cooler intensity I_C with $\tau = 0.5$ ms, $I_{\text{rep}}/I_{\text{C}} \simeq 4\%$ and $\Delta_{\text{pulse}} = 5\Gamma$ **(b)**, as a function of the detuning Δ_{pulse} with $\tau = 0.5$ ms, $I_{\text{rep}}/I_{\text{C}} \simeq 4\%$ and $I_C = 330$ mW/cm^2 **(c)**, and as a function of the relative repumper intensity $I_{\text{rep}}/I_{\text{C}}$ with $I_C = 330$ mW/cm^2, $\tau = 0.5$ ms and $\Delta_{\text{pulse}} = 5\Gamma$ **(d)**. Error bars correspond to one standard deviation. The repumper relative detuning is fixed to $\delta = 0$.

efficiency loss. Close to resonance and on the negative side of the transition, $-6\Gamma < \Delta_{\text{pulse}} < 2\Gamma$, atoms are lost as a consequence of either an excessive photon scattering rate (with the consequent drop in velocity capture range) or polarization-gradient heating on the red side of the transition. For $\Delta_{\text{pulse}} < -6\Gamma$, an inefficient cooling mechanism both in capture efficiency and temperature is recovered, (to temperatures of the order of 100 μK), probably as a consequence of GM cooling involving the $|F_{\text{e}} = 1\rangle$ manifold limited by the effect of off-resonant coupling to the $|F_{\text{e}} = 2\rangle$.

The repumper sideband in this measurement series is set on the resonant Raman

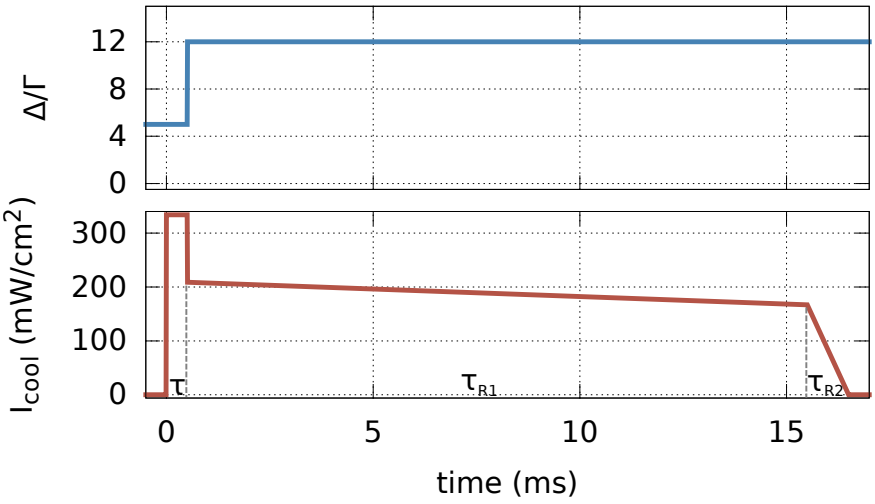

Figure 3.4: Cooler detuning Δ/Γ (blue line, upper graph) and intensity per beam I_C (red line, lower graph) as a function of time for the entire GM sequence. Capture pulse duration τ and the two ramp segments duration τ_{R1} and τ_{R2} are also indicated.

condition $\delta = 0$. Figure 3.3(d) shows the results as a function of the relative repumper intensity I_{rep}/I_C. While the final temperature is practically unaffected by such a parameter, an improvement in capture efficiency is observed for $I_{rep}/I_C \sim 0.04$.

3.2.2 Intensity ramp

Previous results show that in the constant pulse protocol, where intensity and detuning are fixed, the final results are limited by the tradeoff between allowing for large enough sub-Doppler capture efficiency and deep cooling. The dynamical sequence described in this chapter consists of a constant intensity pulse, whose parameter values are set to maximize the initial capture efficiency rather than minimizing the temperature. Such pulse is followed by an increase of the detuning and a progressive reduction of the intensity. Differently from the pulse protocol, here the sub-Doppler velocity capture range decreases together with the instantaneous sample temperature, retaining most of the atoms at the end of the procedure while reaching lower temperature values.

The optimized sequence is reported in Fig. 3.4. Relying on the characterizations shown in the previous subsection, the initial capture pulse is set to a duration of $\tau = 0.5$ ms, and its parameters are set to $I_C = 350$ mW/cm^2 per beam, $\Delta_{pulse} = 5\Gamma$. The detuning value is then increased to 12Γ. A gradual change in such value, instead of a sudden change, did not produce any relevant improvement. This increase in detuning also produces a drop of intensity to about 220 mW/cm^2 due to the different response of the AOMs. Piecewise optimization led to an initial ramp of roughly $10 - 20$ ms duration, to a value of 180 mW/cm^2 followed by a brief ($\tau_{R2} = 1$ ms) intensity ramp to zero. Setting the first ramp segment duration to $\tau_{R1} \geq 8$ ms is sufficient to reach a

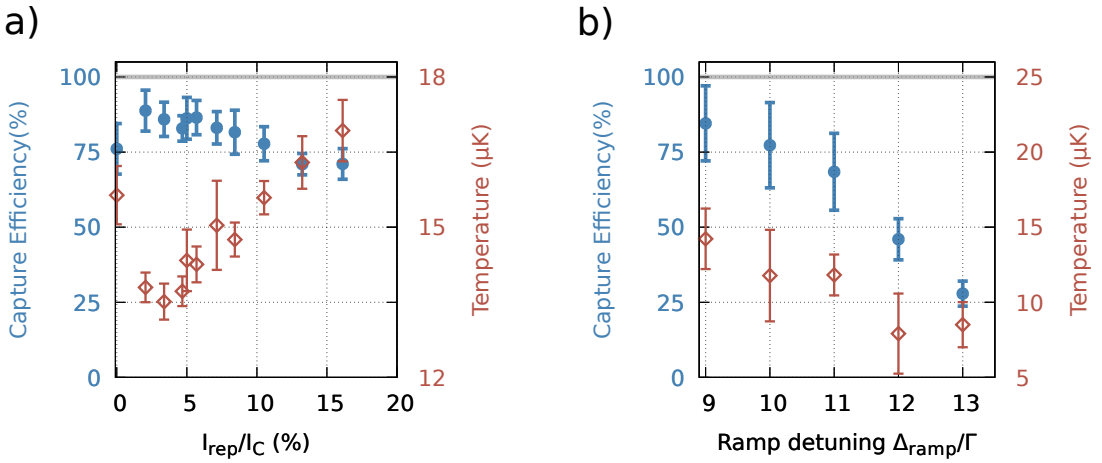

Figure 3.5: Capture efficiency (blue filled circles) and temperature (red empty diamonds) after the complete ramp sequence characterized as a function of $I_{\mathrm{rep}}/I_{\mathrm{C}}$ for $\delta = 0$ and $\Delta_{\mathrm{ramp}} = 10\Gamma$ **(a)**, and as a function of the ramp detuning Δ_{ramp} for $\delta = -0.01\Gamma$ and $I_{\mathrm{C}}/I_{\mathrm{rep}} = 0.034$ **(b)**. Error bars correspond to one standard deviation. The initial pulse parameters are fixed $\tau = 0.5$ ms, $\Delta_{\mathrm{pulse}} = 5\Gamma$ and $I_{\mathrm{C}} = 350\ \mathrm{mW/cm^2}$.

steady minimum in the final temperature. Since no detrimental effects were observed with longer ramp times, τ_{R1} was set to a value of 15 ms.

Fig. 3.5(a) shows the effect of repumper sideband intensity. While the capture efficiency shows a similar behavior to the pulse procedure, in this regime of low temperatures a marked dependence in the final temperature is also observed, whose minimum value is obtained for $I_{\mathrm{rep}}/I_{\mathrm{C}} = 0.034$. The role of the additional Raman coupling, in increasing the cooling efficiency is discussed in subsection 3.2.3.

Fig. 3.5(b) shows the results as a function of Δ_{ramp}. It is worth noticing that during the ramp, for different values of the detuning Δ_{ramp}, a different rescaling factor to the intensity is introduced as a consequence of different diffraction efficiency values of the AOMs. Larger values of PSD correspond to the results obtained at 12 Γ.

3.2.3 Λ-enhanced GM cooling

In the previous subsections the beneficial effect of the additional Raman-resonant coupling induced by the repumper sideband was shown, and optimal conditions were found in terms of relative power. The role of this additional coupling in GM cooling is less trivial compared to the one of the repumper in ordinary cooling techniques discussed 2.3, which consists only into repumping atoms back in a closed cooling cycle. Characterization of GM cooling as a function of the Raman detuning δ (Fig. 3.6) shows an enhancement of the efficiency of GM cooling close to the Raman resonance condition $\delta \simeq 0$, with a strongly asymmetric behavior moving away from the resonance. The best performance of the cooling process, both in temperature and capture efficiency is obtained for small negative Raman detuning $\delta \simeq -2\pi \times 100$ kHz, while for small and

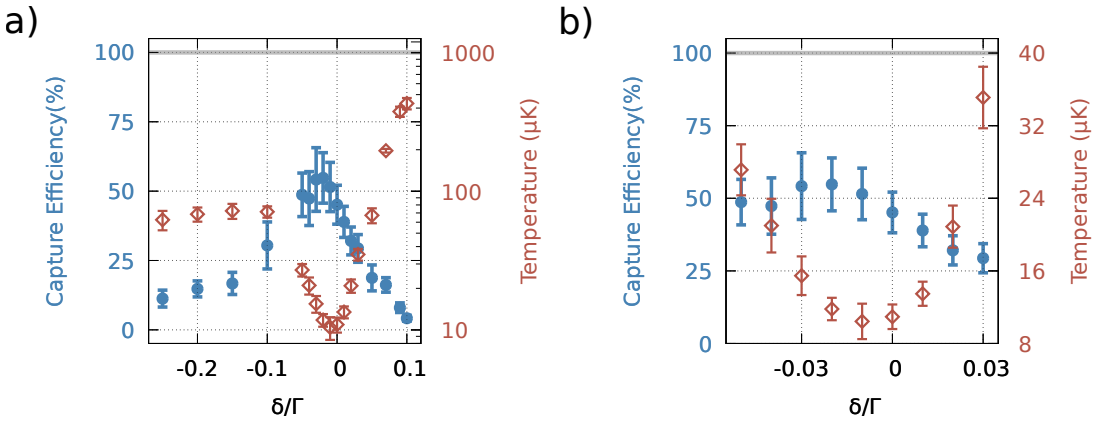

Figure 3.6: Capture efficiency (blue filled circles) and temperature (red empty diamonds) after the complete ramp sequence characterized as a function of δ for $\Delta_{\text{ramp}} = 12\Gamma$ and $I_{\text{rep}} = 0.034\, I_{\text{C}}$ **(a)**. Same data in the close proximity of Raman resonance condition **(b)**. Error bars correspond to one standard deviation. The initial pulse parameters are fixed $\tau = 0.5$ ms, $\Delta_{\text{pulse}} = 5\Gamma$ and $I_{\text{C}} = 350$ mW/cm^2.

positive values of δ, above $2\pi \times 200$ kHz, a significant heating of the sample is observed. A similar behavior is reported in other experiments with ^{7}Li [134], ^{39}K [136], ^{40}K and ^{6}Li [133] and ^{87}Rb [128].

The observed features can be qualitatively understood in a simple three-level Λ configuration involving the hyperfine $|F\rangle$ states, while leaving the Zeeman sublevels unresolved. Such a simplified system supports CPT involving the $|F = 1\rangle$ and $|F = 2\rangle$ states, and suppression of the scattering rate is expected on Raman resonance $\delta = 0$. An asymmetric excitation spectrum with a strong sub-natural peak slightly out of Raman resonance, resembling the observed temperature dependence, is a spectroscopic feature that emerges in systems exhibiting CPT with a similar choice of parameters, and is reproduced in the steady-state solutions of optical Bloch equations (see for instance [139]). The peak, identified as a Fano profile [140], is physically interpreted as a quantum interference effect between the direct excitation pathway, from the long-lived ground state (corresponding to the $|F = 1\rangle$ for $I_{\text{rep}}/I_{\text{C}} \ll 1$) to the excited state, and the three-photon pathway involving the intermediate ground state level $|F = 2\rangle$ [141]. The other effect which contributes to explain the results is that the coupling between different hyperfine manifolds induces additional polarization-gradient effects [134, 136]. Whether these bring additional cooling or a competing heating mechanism depends on the Raman detuning sign and the ratio $I_{\text{rep}}/I_{\text{C}}$. The role of the repumper coupling is then to provide a GM cooling scheme in addition to the one just involving the bare $|F = 2\rangle$ Zeeman manifold. This new scheme complements or hinders the main GM operating on the cooling transition, increasing its efficiency or introducing competing heating effects. On Raman resonance atoms are pumped in a long-lived dark state manifold involving both ground state hyperfine manifolds, further suppressing

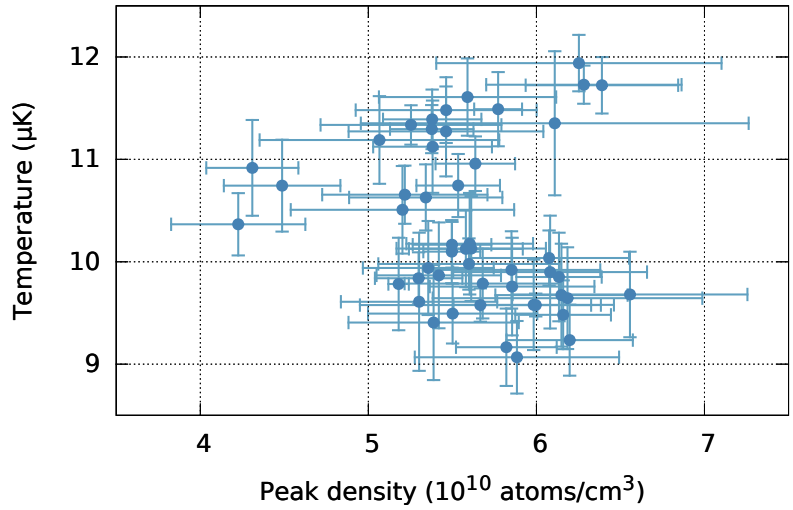

Figure 3.7: Temperature after GM as a function of the sample peak density.

the scattering rate. The validity of the simplified picture given above is confirmed in studies where the full Zeeman level structure is taken into account [128, 133].

3.2.4 Final results and comparison between different cooling protocols

Comparison between different cooling protocols is shown in Table 3.1, after a careful re-optimization of the system and of the magnetic field cancellation. Results obtained with GM cooling protocol are compared with the ones obtained with the ordinary optical molasses procedure, operated on the D2 transition, that was already optimized and regularly used in the same experiment. The comparison shows that the constant intensity GM pulse gives analogous results to the typical ones produced with the bright optical molasses sequence. PSD after the complete GM sequence improves by one order of magnitude compared to such results, to a value of the order of 10^{-4}, and the measured temperature of 8.9(4) μK is below $4\,T_{\mathrm{rec}}$.

Implementations preceding the reported results show similar performances. Temperatures down to 800 nK, were obtained with ^{133}Cs [126]. Such a value is slightly larger than $4\,T_{\mathrm{rec}}$ calculated for Cs. A PSD value of 2×10^{-4} was obtained with ^{39}K [135]. A realization with ^{85}Rb reported in [131] allowed for values of PSD as large as 1.7×10^{-3} by combining GM with spatial compression stages.

Density-dependent heating

As mentioned earlier, one of the mechanisms which limits the efficiency of atom cooling techniques is photon multiple scattering in a dense sample. This mechanism provides an effective atom-atom repulsive force, limiting the maximum atom densities. Another consequence of this detrimental effect that can be observed in optical

	Eff%	$n_{\mathrm{p}}\,(\mathrm{cm}^{-3})$	$T\,(\mu\mathrm{K})$	PSD
DS-MOT	–	$9(1)\times 10^{10}$	355(12)	$6.8(10)\times 10^{-7}$
D_2 Molasses	80	$4.3(2)\times 10^{10}$	38.1(9)	$8.9(6)\times 10^{-6}$
GM pulse	100	$6.3(3)\times 10^{10}$	46.9(6)	$9.5(4)\times 10^{-6}$
GM ramp	70	$6.0(5)\times 10^{10}$	8.9(4)	$1.1(1)\times 10^{-4}$

Table 3.1: Comparison between results after different optical molasses cooling protocols and typical conditions after DS-MOT loading. GM is operated with the same parameters as shown in Fig. 3.4, with $\delta = -0.01\Gamma$ and $I_{\mathrm{C}}/I_{\mathrm{rep}} = 3.4\%$. Eff%: approximative capture efficiency, n_{p}: peak density, T: temperature, PSD: phase-space density.

molasses, where no confining force is present, is density-dependent heating. GM cooling on the D1 line is expected to be less affected by multiple scattering, compared to ordinary molasses operating on the D2 transition. Pioneering works with GM on the D2 showed density-dependent heating comparable to ordinary bright molasses [125], and some residual heating can be observed also operating on the D1 transition, as confirmed in [133]. We attempted an investigation of possible density-dependent heating effects in our sample by reducing the loading time of the MOT. The limit of such a method is that the r.m.s. size of the cloud scales nearly as $N^{1/3}$, which translates in a narrow investigation window, between 10^{10} and 10^{11} atoms/cm^3. As shown in Fig. 3.7, no correlation emerges between temperature and density within our temperature sensitivity and density operational range. A more precise and broad density range investigation was not attempted, being outside of the scope of my work.

Chapter 4

Bose-Einstein condensation of sodium atoms in a magnetic-shield-compatible hybrid trap

***

This chapter deals with the production of *Bose-Einstein condensates* (BECs) of sodium with a magnetic-shield-compatible protocol. After a few unfruitful attempts

to efficiently load atoms into a pure *optical dipole trap* (ODT) from GM, quantum degeneracy was successfully and reliably achieved in a hybrid trap configuration. In such a configuration the *quadrupole magnetic trap* (QMT) is operated at low values of magnetic field gradient, of the same order as the one for MOT operation, well below the saturation limits of a properly designed μ-metal magnetic shield, with our approach differing from the one usually followed in this kind of traps. Here I demonstrate that, by combining a shallow QMT acting only as a reservoir with a tightly focused and comparatively deep ODT, efficient loading of the ODT can be achieved without the need of adiabatic loading, and with a reduced sensitivity to beam alignment.

In the first section, after a general introduction, I give a brief account of the direct ODT loading attempts. Such attempts failed at a preliminary stage, and only the relevant aspects are discussed qualitatively. In the following section I introduce the general features of the hybrid trap configuration with a single ODT beam, and I discuss the strategy leading to this choice. In the third section I report the curves of calibration of the final hybrid trap configuration, and in the fourth section I describe each step towards BEC. In the fifth section I present the final results and the characterization of the experimental sequence.

4.1 Introduction

The typical route to reach quantum degeneracy, consists in first loading a laser-cooled atomic sample into a conservative trap, then evaporatively cooling such a sample to quantum degeneracy. Atoms can be efficiently loaded into magnetic traps from a Magneto-optical trap (MOT) or optical molasses thanks to the large capture volume of the former. Trapped atoms in such a kind of trap show more convenient sample numbers and enhanced peak densities as a consequence of the long-range linear form of the potential and allow, at the lowest temperatures, to evaporate atoms at a fixed trapping frequency via energy-selective RF transitions to untrapped states. A highly efficient evaporation is achieved in this kind of traps by adiabatic compression of the trapping potential, typically to field gradients of the order of hundreds of G/cm, leading to an increase of the elastic collisions rate of the sample.

The present experiment is aimed at the study of defect dynamics in a Rabi-coupled binary mixture, involving the internal states of sodium $|1, \pm 1\rangle$. As argued in subsection 1.2.4, in order to maintain phase-coherence between the two components for a sufficiently long time to study the system dynamics, one requires the reduction of spurious unwanted magnetic fields to better than 10 μG. Such a reduction can be achieved either by active compensation or passive shielding. Active compensation is more complicated to implement, but is more suitable when dealing with noise in the $10-1000$ Hz frequency range, while compensation of static and low-frequency external magnetic fields can be easily achieved using passive magnetic shields. Both techniques can be used on a given experiment, due to their complementarity. High magnetic permeability materials suitable for this application, such as μ-metal and analogous alloys, are limited by their tendency to saturate when exposed to high magnetic fields, and lose their magnetic shielding properties until a demagnetization cycle is applied.

Elements that produce the magnetic fields necessary for the experiment must be fitted inside the shield, and the compatibility between these elements and the shield saturation limits must be carefully taken into account. A detailed study of such compatibility cannot leave the specific shield and coils design out of consideration and requires a simulative approach, that is reported in E.Fava Ph.D. thesis [40].

The final design of the magnetic shield, that will be used in our experiment, consists of the four cylindrical layers shown in Fig. 4.1(a). The innermost layer is composed of a different alloy (Supra-50), characterized by a larger magnetic field saturation threshold ($B_{\text{sat}} = 1.6$ T), compared to the three external layers (made of Mu-Metal). Each layer is made of two halves, with the top half partially sliding into the bottom one, in order to ensure contact continuity. Optical access to the octagonal cell windows is provided by 30 mm diameter holes, while additional smaller holes provide access to cables and support screws. The external dimensions of the assembly are 217 mm of base diameter and 323 mm height. The simulations for such a design predict an attenuation of the external magnetic field fluctuations to better than 10^4, with a satisfying spatial homogeneity [40]. Another result is that the magnetic fields produced by quadrupole coils inside the shield are unlikely to produce saturation effects, when exerting on the atoms a magnetic field gradients of few tens of G/cm, compatible with MOT operation or weak magnetic trapping (Fig. 4.1(b)). Compressed magnetic traps, on the other hand, could exceed these limits, especially considering the non-ideal response of the shielding material, and for this reason protocols to reach quantum degeneracy through magnetic trap compression were excluded.

Production of degenerate atomic samples with all-optical techniques allows in principle to circumvent these limits. Despite their well-known advantages, such as the possibility to devise spin-independent trapping potentials, pure *optical dipole traps* (ODT) are limited by the available power in the tradeoff between the capture volume and trap depth and, in the simplest implementations, by the reduction of trapping frequencies during evaporation. More refined techniques that have been recently demonstrated [142, 143] are required to decouple trap confinement and depth. Weak longitudinal trapping in single beam configurations usually implies the use of two crossed beams, further reducing the trapping volume.

Production of BECs in traps that combine the advantages of both optical and magnetic potentials was demonstrated to be a viable strategy since the first realizations [144], where a repulsive "optical plug" was used to suppress Majorana spin-flips [145] in a simple quadrupole magnetic trap. Another recently demonstrated approach consists in combining a red detuned single beam [146, 147] or crossed [138] dipole trap with a QMT. Since the collisional rate of atoms captured in the magnetic trap, in typical conditions, is too low to ensure an efficient RF evaporation, the adiabatic compression of the QMT remains a key strategy with such an hybrid approach. In fact, temperature and density for the linear quadrupole potential scale respectively as $B'^{2/3}$ and B' [144], increasing the collisional rate (hence the evaporation efficiency), as well as its ratio to Majorana spin flip losses (which scale as $(B'/k_BT)^2$) [145, 148]. On the other hand, even all-optical production techniques can be enhanced by using weak magnetic field gradients to spin-polarize the sample [135], or to compensate for

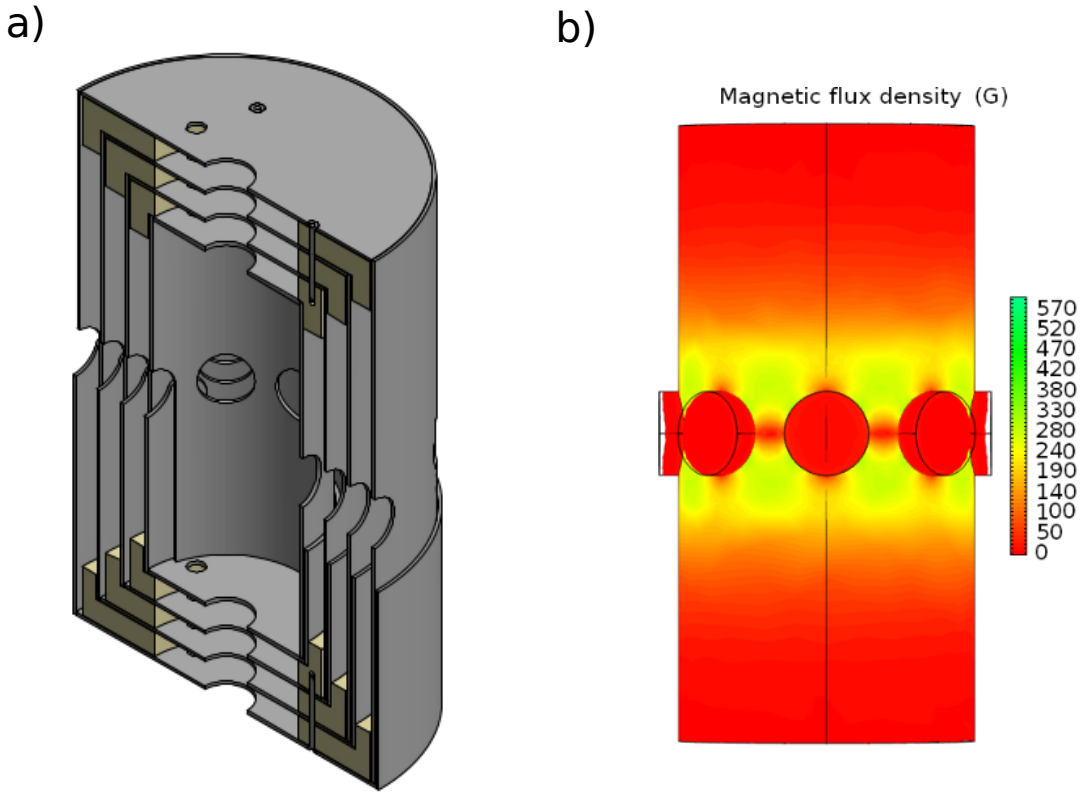

Figure 4.1: **a)** Section view of the four magnetic shield layers. **b)** Magnetic flux density produced inside the inner shield by coils placed around the cell top and bottom window, operated to produce a magnetic field gradient of 50 G/cm. Image taken from Ref. [40].

gravity during optical evaporation [142].

Experiments aimed to the study of multicomponent BECs require to transfer the sample into a pure optical trapping potential at a given point, hence the simplest choice in terms of procedure is to produce the condensate directly in a pure optical trap. Constraints on magnetic field gradient imposed by magnetic shield compatibility, at first glance, discouraged us from trying a hybrid protocol first. So our first attempt was an all-optical protocol, as is described in the following subsection.

4.1.1 Direct ODT loading attempts

The first attempted protocol consisted in reaching quantum degeneracy in an all-optical way. This required to directly load atoms into an ODT from GM. Efficient loading relies on the diffusive motion of atoms in the optical molasses, caused by photon scattering, with the simultaneous presence of the ODT. This diffusion-driven loading mechanism is critical to the efficiency of the protocol since the trapping volume of ODTs is generally much smaller than the one of the MOT. Since loading happens in the

simultaneous presence of the optical molasses, a critical issue to be taken into account is the way in which the light shift, induced by the ODT, interferes with molasses cooling. In the ideal situation, there is a range of parameters for which a functional cooling protocol is retained for atoms both external and internal to the trapping volume, in such a way that the trapped sample is cooled and its density increases while atoms are transferred to the ODT. In this respect, GM was an ideal candidate allowing to trap atoms with relatively low optical powers, and further cool them once trapped, taking advantage of the absence of density-limiting effects and density-dependent heating, as discussed in Chapter 3. Achieving this situation, however, requires to take into account not only the intensity-dependent energy shift of the ground state, relevant for trapping, but also the one of the excited state. In this respect, a significant increase in the excited state polarizability can emerge as a consequence of the trapping laser being nearly resonant to a transition between the excited state and higher energy levels, usually neglected in a simple two-level approximation. When properly taken into account, these effects can be exploited to implement specific measurements and loading protocols [143, 149]. On the other hand, if not tracked, they can lead to incompatibility between the GM and ODT.

Sample pre-cooling

The following attempts were made with roughly half of the optimal atom number loaded in the DSMOT. Reimplementation of GM in the new experimental apparatus was straightforward using the same procedure described in Chapter 3, and roughly 1.6×10^9 atoms were cooled to values of temperature and PSD comparable with the ones reported in Chapter 3. Since the size of the density distribution after GM was still of the order of one millimeter, this was not expected to be an issue for direct transfer in the ODT due to its comparatively small capture volume. Transfer to the ODT was attempted in three different beam configurations, briefly described below. For each of three, a re-optimization of the GM parameters was attempted, trying to find the conditions for improved loading.

Crossed dipole trap configuration

The first ODT trap configuration in which a direct loading procedure was attempted was a *crossed dipole trap* (CDT). The necessary laser power is delivered in the vicinity of the octagonal quartz cell by means of the two high-power optical fibers described in section 2.5. Both beams were focused to an estimated waist of the order of 50 µm, propagating along orthogonal directions. The correspondent trap depth is of the order of $k_B \times 80$ µK, when operating both beams at 6 W. Up to 2×10^6 atoms could be captured in the horizontal beam.

For this attempt absorption imaging in the direction of the atomic source was implemented using the push beam as a probe to avoid the overlap of ODT and imaging directions. The push beam was geometrically reshaped, to pass through the DP channel of the chamber then expand to a sufficient size at the atoms position. Such an imaging allowed only for qualitative information on the number of atoms in the cross

region. More than 2/3 of the trapped atoms were lost from the cross region during the initial equilibration time, of the order of a hundred ms, after which a lifetime of few seconds could be observed.

Atoms cooled in GM are in a superposition of states involving both $|F_g\rangle = 1, 2$ hyperfine manifolds. Since trapped atoms in different hyperfine states enhance inelastic collisional losses, a depumper protocol to depopulate the $F_g = 2$ was applied at the end of GM ramp, by turning off the D1 repumper in the last ms of the GM ramp, eventually increasing the cooling light intensity. This did not lead to any relevant improvement, however.

Horizontal cross configuration

Suspecting that the strong depletion could be caused by insufficient axial trapping, we moved to a second configuration in which the horizontal beam was recycled and crossed with itself at a narrow angle. This configuration aimed to add an axial confinement to the horizontal beam without reducing too much the trapping volume, eventually to improve the loading conditions in the region crossed by the vertical beam. This also required to ensure orthogonal polarizations between the main and the recycled beam, to avoid lattice intensity interference effects. All the attempts made with this configuration still resulted in an inefficient loading. Estimated atomic densities in the trap resulted of the same order of the density of the thermal cloud in GM, and an initial depletion comparable to the previous case, on a timescale of half a second, was still observed.

Loading in a deep dimple ODT

After the previous attempts, I tried to load the atoms to a tightly focused (13.5 µm waist) single beam ODT. For this attempt I used an ODT branch without optical fibers (see section 2.5), increasing the amount of power at disposal to 17 W. Using such a configuration, in contrast with previous observations, atoms could be held in the single beam trap for tens of seconds, but still no more than 2.2×10^6 atoms at densities of the order of 10^{11} atoms/cm^3 could be loaded, regardless of the loading protocol used. Applying a GM capture pulse to the trapped atoms resulted in a complete loss, signaling that GM was not working as intended on the atoms inside the trapping volume.

Concluding remarks

All the described preliminary attempts failed to produce sizable capture and were not suitable for any sort of meaningful quantitative characterization. It was then clear that a more systematic approach was required if we wanted to pursue with the all-optical protocol. An explanation of the described issues, is the enhancement of the excited state polarizability. The trapping laser wavelength we use (1064 nm) is relatively close and blue-detuned to the $3P - 4S$ transition for sodium (1140 nm) [150]. The validity of this hypothesis has not been investigated yet. Following a pragmatic approach, instead, we moved to the hybrid trap protocol, that turned out to be a

successful strategy even with the constraints imposed by the saturation limit of the magnetic shield.

4.2 Production of BECs in a low-magnetic-field-gradient hybrid trap

4.2.1 GM reimplementation

Since QMTs are characterized by a larger capture volume compared to ODTs, I re-optimized the system to improve the loading conditions in the QMT of the hybrid trap configuration. The GM procedure was adjusted focusing on the following considerations:

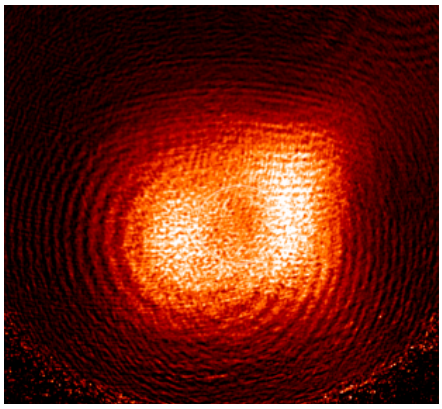

Figure 4.2: Density profile of the cold atomic cloud after GM at 1 ms TOF, before increasing the spot size.

Beam Waist: After MOT re-optimization, as much as 5×10^9 atoms were recovered, increasing accordingly the size of the MOT. After this, a reduction in GM capture efficiency and an apparently cut integrated density profile at low expansion times were observed. I interpreted this as a consequence of the non-uniformity of the beam intensity, or imperfect alignment, leading to insufficient capture velocities on the tails of the atom distribution, hence atom losses, especially for large values of Δ_{ramp}. After increasing the GM beam waist to 3 mm capture efficiencies of the order of 70%, were recovered.

Depumping: As it was already implemented for direct ODT loading, the repumper sideband of the D1 is turned off before the end of the GM. However, as a consequence of the high detuning and low intensity in the last part of the ramp, this depumping protocol was not efficient. Increasing the duration of the depumping procedure led to a degradation of GM performances. The best compromise was then to reduce the detuning to 4Γ, to increase the depumping rate, during the last 0.5 ms of the GM ramp.

Ramp Duration: Atoms in optical molasses are not confined and undergo a diffusive motion, and for this reason longer ramps are expected to lead to a reduction of peak density. Since the initial ramp was longer than necessary, to improve loading conditions in the QMT the ramp duration was reduced as much as possibile to the point where a reduction of GM performances was observed. This was done after the increase of the beams size and, in contrast with the results obtained in the previous implementation,

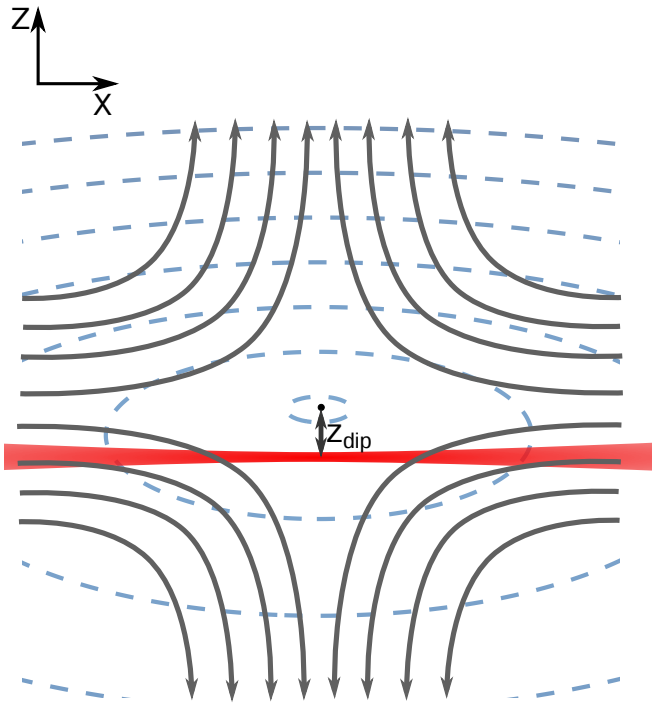

Figure 4.3: Sketch of the hybrid trap configuration. A single beam dipole trap (red shaded region) is focused below the quadrupole trap center at a distance z_{dip}. Here z is the simmetry (strong) axis of the QMT, while x designates the axial coordinate of the dipole beam. Magnetic field lines are pictorially represented (solid, gray) as well as magnetic potential contour lines accounting for gravity in arbitrary units (dashed, blue).

resulted in a marked increase in efficiency, to near unity, and no degradation for ramps as short as 5 ms and $\Delta_{\mathrm{ramp}} = 12\Gamma$.

4.2.2 Description of the hybrid trap configuration

The single beam HT configuration is sketched in Fig. 4.3, where the vertical (z) direction coincides with the quadrupole coils symmetry axis. An attractive optical potential is obtained by means of a red-detuned horizontal laser beam (1064 nm), which is superimposed to the quadrupole trap. The beam focal point is vertically displaced from the QMT center, preserving atoms trapped by the ODT potential from depolarization due to Majorana spin flips. For a relative displacement of z_{dip} the combined magnetic, gravitational and optical potential is

$$U(x,y,z) = \mu B'_{\mathrm{z}} \sqrt{\frac{x^2}{4} + \frac{y^2}{4} + z^2} - C\frac{2P}{\pi w^2(x)} e^{-2\frac{y^2+(z-z_{\mathrm{dip}})^2}{w^2(x)}} + mgz. \tag{4.1}$$

The first term in the right-hand side of the equation is the quadrupole magnetic potential in the vicinity of the trap center, the second term is the optical potential term and the third term is the gravitational one. In this equation, B'_z is the magnetic field gradient along z, μ designates the magnetic moment of the atoms, and C is a constant proportional to the polarizability of the atomic species ground state, depending on the trapping beam wavelength. The constant C, for a far-detuned ODT operating at $\lambda_d = 1064$ nm, amounts to 7.27×10^{-37} J/(W m^{-2}).

The general route to quantum degeneracy in such a trap, that was also followed in the first hybrid-trap realization described below, consists in capturing the atoms in the combined potential, with the dipole beam focused below the QMT center at a distance of the order of the beam waist $z_{dip} \simeq w_0$, then performing RF evaporation after adiabatic compression of the magnetic trap, until Majorana losses become relevant in the QMT trap center. After this, the QMT gradient is gradually reduced to a value almost compensating for the Earth gravity potential, transferring adiabatically part of the atoms in the ODT trapping beam. The residual QMT gradient then contributes to the beam axial trapping during evaporative cooling in the ODT. On the contrary, the currently employed configuration that is described afterwards, allows us to efficiently load the ODT without magnetic compression, with no critical dependence on the ODT alignment nor the need of adiabatic transfer.

First realization

In the first hybrid trap configuration that we used the ODT beam was focused to a waist of approximately 50 µm on the atoms without the use of optical fibers. Following the above described procedure, BECs composed of up to 4×10^6 atoms were produced. Such a configuration was however not satisfactory for a series of reasons. I was not able to find an optimal protocol to produce BECs both without compression and, at the same time, at lower values of the ODT power. The production of condensates was unreliable, with strong drifts on the performance during the day and a critical dependence on the vertical alignment of the dipole beam. Such drifts can be in part related to the pointing instabilities of the ODT test branch, which could be fixed by using an optical fiber, but also from thermal drifts of our copper coils, not designed to work in steady state at $B'_z \simeq 30$ G/cm. Taking these issues into account, I moved to the configuration described below.

Present configuration

Currently the ODT beam is collimated at the output of an optical fiber to an approximate waist value of about 3.2 mm then focused on the atoms through an $f = 200$ mm achromatic lens, to a waist of 23 µm on the atoms. Such a value is inferred from the radial trapping frequencies measured on the condensate as described in the next section. The ODT propagates quasi-coaxially (9° tilt) to the horizontal imaging direction. In the context of this chapter, the x direction is referred to the ODT axial direction.

Compared to the previously described arrangement, we expect a reduction of pointing instabilities as a consequence of the geometrical decoupling induced by the optical fiber. The significant reduction in the waist, roughly a factor of 2, was chosen in order to reduce the necessary amount of power to load the atoms in an equivalently deep ODT. These qualitative assumptions proven to be correct. In the new configuration, BECs can be reliably produced in the desired conditions of low capture power (down to 4.2 W) and in the absence of magnetic trap compression. The next section deals with the characterization of the relevant trap parameters for this configuration, and with the optimization of the different steps of the sequence.

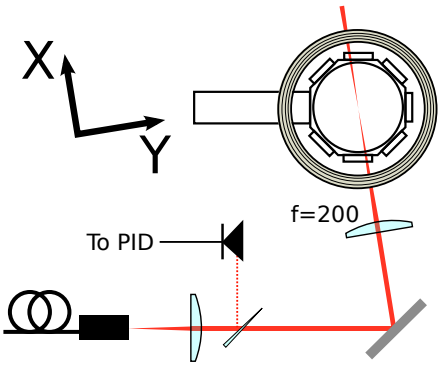

Figure 4.4: Sketch of the current hybrid trap configuration.

4.3 Characterization of trap parameters

In this section I describe the experimental characterization of the trapping potential. In the first subsection I describe the fine calibration procedure for the QMT coils gradient, and the vertical ($\hat{z}$ field direction) compensation coils. In the second subsection, I describe the procedure to extract the values of the trapping frequencies for our hybrid trap exploiting collective oscillations induced on the condensate. Both described procedures are standard routines in ultracold atoms experiments and their results are here used extensively in the following, for a full quantitative characterization of the experimental sequence.

4.3.1 Magnetic coils calibration

Quadrupole magnetic coils

In order to calibrate the QMT gradient, I determined the acceleration a_{M} induced on the condensate by operating the lower quadrupole coil in levitating configuration, as a function of the coil current and by measuring the atomic position in time. The resulting acceleration values are reported in Fig. 4.5(a). Magnetic fields exerted on the atoms during this procedure can be as high as 40 G in modulus, and higher-order corrections to the Zeeman energy shift must be taken into account. The lowest-order correction term is obtained by expanding in series the Breit-Rabi formula [151], and corresponds to a term quadratic in the current, additional to the linear Zeeman shift

$$a_{\mathrm{M}} = a^{(\mathrm{I})}\frac{\mathrm{d}B_{\mathrm{z}}}{\mathrm{d}z} + a^{(\mathrm{II})}B_{\mathrm{z}}\frac{\mathrm{d}B_{\mathrm{z}}}{\mathrm{d}z}, \tag{4.2}$$

that is accounted for in the fitting function. The resulting gradient of 1.11(2) G/(cm A) corresponds to half of the gradient along the $\hat{z}$ direction when operating both coils, in

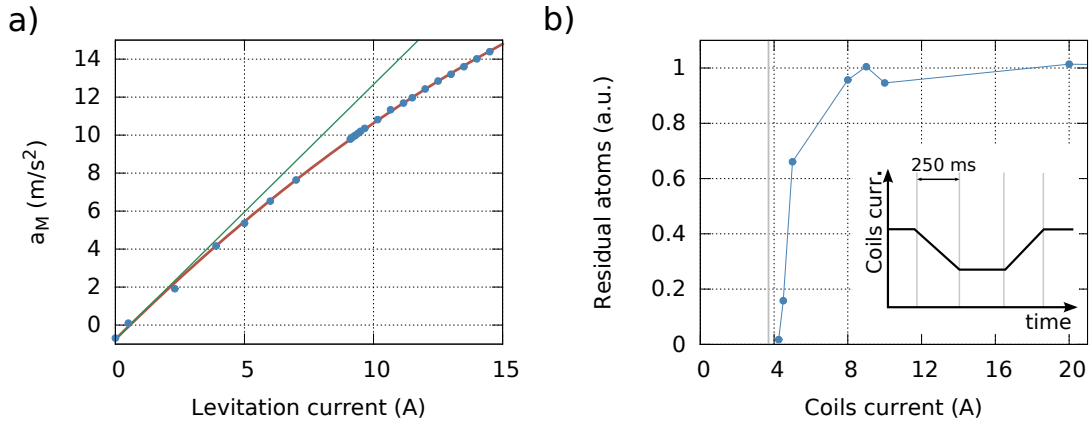

Figure 4.5: **a)** Acceleration induced on the condensate by operating the quadrupole coils in levitating configuration obtained by fitting levitation trajectories for different values of operating current. The red line shows the result by fitting the curve taking into account quadratic corrections. The green line shows the bare linear term, in the absence of corrections. **b)** Retained number of atoms in the QMT after decompressing the trap for 250 ms, as a function of the operating current during the decompressed phase. The gray vertical line signals the current at which the quadrupole potential is expected to exactly compensate for gravity, from the data of panel (a).

MT and MOT configuration. This result implicitly assumes coils symmetry, and sufficient spatial homogeneity of the field gradient in the region explored by the levitation trajectories.

Figure Fig. 4.5(b) shows the results of a less accurate measurement, used as consistency check: after capturing the atoms at the end of GM and adiabatically compressing the QMT, the current was reduced in 250 ms to a given value, for a duration of 250 ms, before re-compression. The residual number of atoms after this operation is plotted as a function of the decompressed trap current. The gray line signals the value of the current for which the vertical gradient is expected to exactly compensate for gravity, according to the previously shown calibration. Apart from a small offset, maybe given by the transient, the two results are consistent. For the remainder of this chapter, the result of the first measurement is used.

Vertical compensation coils

An additional homogeneous magnetic field $B_0\hat{z}$ produces a shift of the QMT center $\Delta z = B_0/B'_z$. Calibration of both the compensation coils and the quadrupole coils is then required for quantitative current-driven control over the displacement z_{dip}. This calibration implicitly takes advantage of the horizontal magnification parameter calibration, which was carried out studying free-fall trajectories. Figure 4.6 shows the calibration measurements, from which a value of 1.21(2) G/A is obtained.

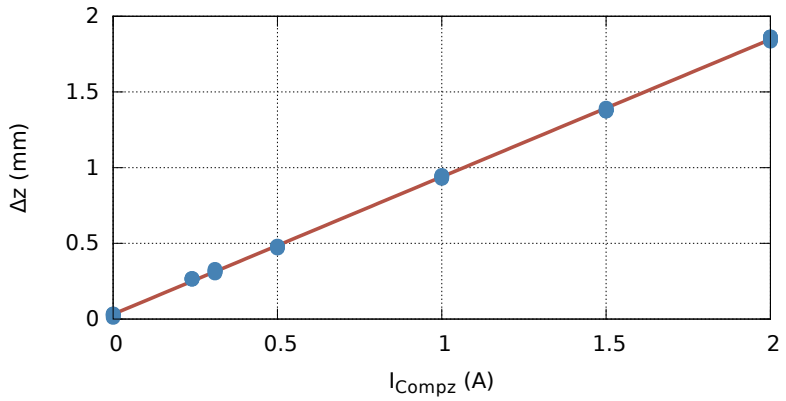

Figure 4.6: Displacement of the center of a QMT operated at 13.3 A (blue dots), as a function of the compensation coil current. The slope (0.908(2) mm/A) is extracted by a linear fit (red line).

4.3.2 Trapping frequencies

Ultracold atomic samples typically explore only the bottom part of the trapping potential. This allows to approximate the potential simply with a harmonic trap, which in turn is fully characterized by the harmonic oscillator frequencies. Experimental determination of the potential trapping frequency provides an important piece of information for several reasons.

- Trapping frequencies scale predictably with experimental parameters that can be reproducibly controlled, such as ODT beam power and QMT magnetic field gradient. A single experimental determination of trapping frequencies for a given set of conditions is then sufficient to infer the trap frequency for different parameter values.

- In-trap equilibrium properties of the atomic sample (such as peak density and PSD) are easily accessible from a temperature measurement if the trapping frequencies are known, and if thermal equilibrium can be assumed.

- Properties of quantum-degenerate gases have been studied extensively in the harmonic potential approximation, thanks to its formal tractability. Trapping frequencies appear explicitly in many of these properties, such as the critical temperature for condensation.

Values of the radial trapping frequencies $\omega_{y,z}$, for the combined potential (4.1), are dominated by the optical dipole trap component, thus they can be approximated by the ODT potential contribution only

$$\omega_{y,z} \simeq \omega_{y,z}^{ODT} = 2\sqrt{U_d/mw_0^2}, \tag{4.3}$$

where U_d designates the dipole trap depth, and w_0 the beam waist. For the axial trapping frequency the situation is different. Both contributions from the optical and the magnetic potential are expected to be relevant for our experimental parameters throughout the entire experimental sequence. The total trapping frequency can be expressed as the sum in quadrature of the two contributions

$$\omega_x = \sqrt{\left(\omega_x^{QMT}\right)^2 + \left(\omega_x^{ODT}\right)^2}, \tag{4.4}$$

where ω_x^{QMT} is the magnetic potential contribution to the trapping frequency evaluated along the ODT beam axis

$$\omega_x^{QMT} = \frac{1}{2}\sqrt{\frac{\mu B'_z}{m z_{dip}}}, \tag{4.5}$$

and ω_x^{ODT} is the axial trapping frequency of the bare ODT. For an ideal Gaussian beam such a quantity is related to the radial trapping frequency by a scaling factor $\omega_x^{ODT} = \omega_{y,z}^{ODT}\lambda/(\pi w_0\sqrt{2})$. This relation is not assumed here, to take into account the possible effects related to an imperfect beam quality, such as beam astigmatism.

Experimental measurement of the trapping frequencies

In order to perform clean measurements of the trapping frequencies, collective excitations are induced directly on the condensate. Indeed, the frequencies of such modes are proportional to the trapping frequencies, with a proportionality factor that accounts for the effect of mean-field interactions, and depends on the involved kind of excitation [152]. Center of mass oscillations, in particular, are not influenced by the presence of atom-atom interactions, and allow to directly measure the trapping frequency. For the reported measurement of the trapping frequencies, the ODT was operated at 60 mW of power, and the quadrupole gradient along the coil symmetry axis was set to $B'_z = 7.74$ G/cm.

Compression modes are induced performing a release-and-recapture measurement with 0.15 ms switch-off time. Thomas-Fermi radii, measured after 20 ms of free expansion, are shown in Fig. 4.7(a,b,c) as a function of the in-trap hold time. The results show in-phase compression modes along the radial directions of the condensate and a longer timescale axial compression mode. The corresponding frequencies, extracted by fitting the data, are $[\omega_y^{cp}, \omega_z^{cp}] = 2\pi \times [1.024(5), 1.021(5)]$ kHz, and $\omega_x^{cp} = 2\pi \times 16.1(1)$ Hz. The related trapping frequencies, considering the trap geometry [152], are then $\omega_{y,z} = (1/2)\,\omega_{y,z}^{cp} = 2\pi \times [512(3), 510(3)]$ Hz in the radial directions, and $\omega_x = (\sqrt{2/5})\,\omega_x^{cp} = 2\pi \times 10.2(1)$ Hz in the axial one. Axial oscillations, induced in the same trap conditions (shown in Fig. 4.7(d)), give a consistent result of $2\pi \times 10.2(1)$ Hz. From the radial trapping frequencies and the measured ODT power, the beam waist on the atoms is estimated to be 23 µm using (4.3).

Experimentally measuring the dependence of ω_x on z_{dip}, appearing in (4.4) through the quadrupole magnetic trap contribution (4.5), I extracted the axial ODT contribution to the trapping frequency ω_x^{ODT}. Figure 4.8 shows the axial oscillation frequencies

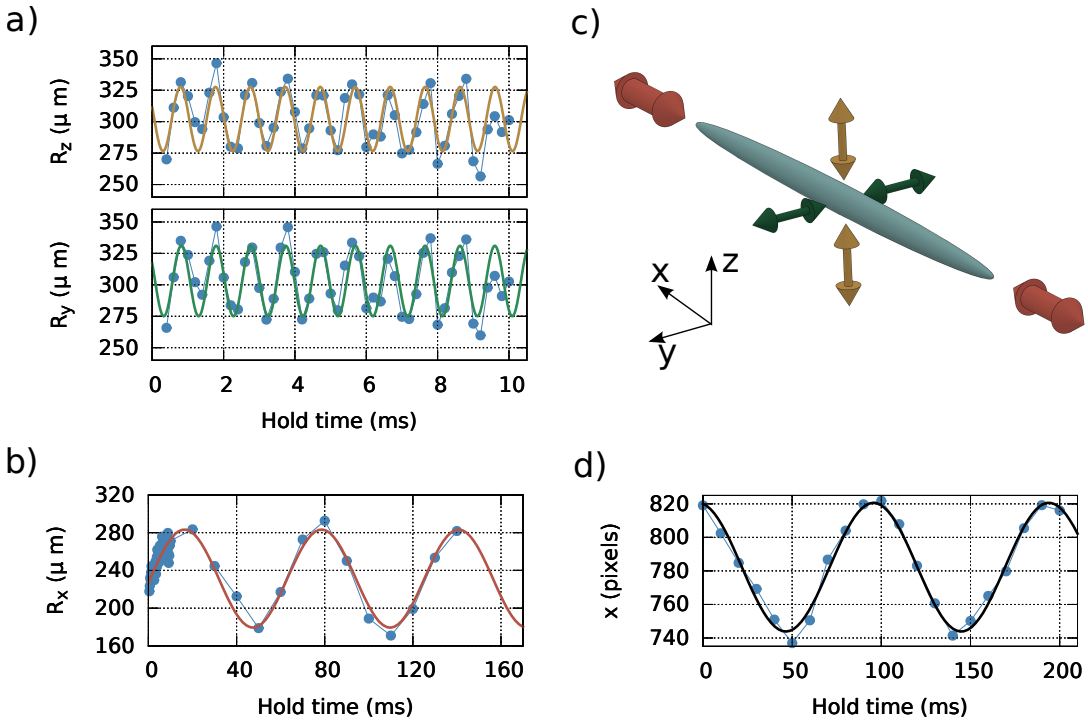

Figure 4.7: Thomas-Fermi radii measured after 20 ms of free expansion, in the radial **(a)** and axial **(b)** directions, as a function of hold time in trap. The corresponding modes are sketched in **(c)**. Measured axial oscillations **(d)**, as a function of hold time. Fit results are also shown for each dataset.

measured as a function of the vertical displacement z_{dip}, which is controlled through the vertical bias field (see subsection 4.3.1). The value of the ODT axial trapping frequency extracted fitting the experimental data with (4.4) and (4.5) is $\omega_{\mathrm{x}}^{\mathrm{ODT}} = 2\pi \times 2.5(2)$ Hz, corresponding to roughly half of the value expected for an ideal Gaussian beam with the given beam parameters. A rapid check of axial oscillation frequency in the bare ODT provided a result of the order of $\omega_{\mathrm{x}}^{\mathrm{ODT}} = 2\pi \times 2.8$ Hz.

4.4 Optimization of the experimental sequence

In this section, the step-by-step optimization of the experimental sequence is described. In the first subsection I characterize the matching between the thermal cloud after GM, and the QMT potential. After this, I show the advantage related to the presence of a RF signal that stabilizes the temperature of the reservoir during the loading stage of a deep ODT. Finally I describe the optimization of the dipole evaporation ramp, before moving to the next section, where the optimized sequence is fully characterized.

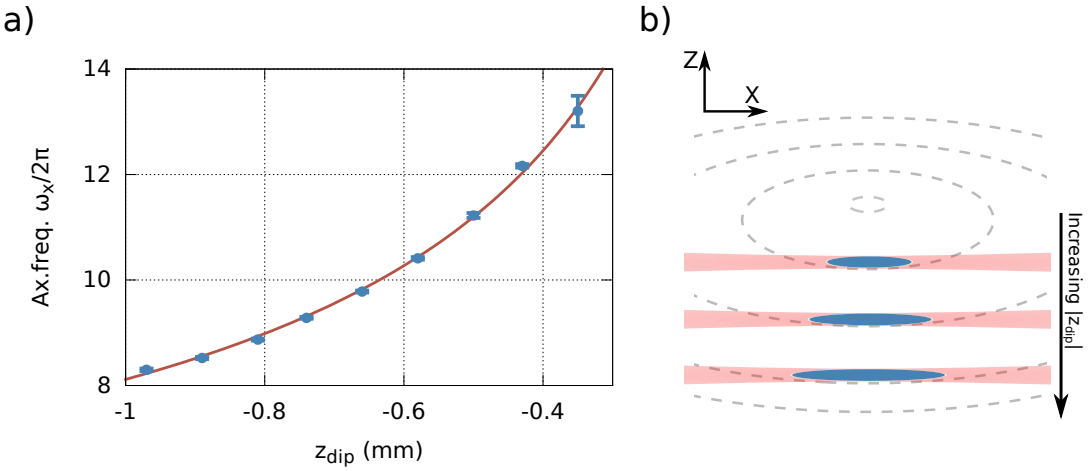

Figure 4.8: Axial trapping frequency measured as a function of the vertical displacement **(a)**. The vertical displacement is quantitatively controlled applying a bias magnetic field in the z direction. The red curve is the fit of the experimental data with z_{dip} and $\omega_{\mathrm{x}}^{\mathrm{ODT}}$ as free parameters. The sketch in panel **(b)** represents the reduction of the axial trap confinement, as $|z_{\mathrm{dip}}|$ is increased.

4.4.1 Optimization of QMT loading condition

Once the GM cooling sequence is completed, the sample is transferred to a QMT. Since the unpolarized sample occupies the $|F_{\mathrm{g}} = 1\rangle$ manifold and only atoms in the low-field-seeking state $m_F = -1$ can be trapped, a transfer efficiency of the order of 1/3 is expected. The QMT is loaded by abruptly turning on the coils in magnetic trap configuration, setting the magnetic field gradient to an optimal value which depends on both the cloud size and temperature.

The figure of merit used to quantify the matching between the capture gradient and the thermal cloud is the sample PSD after equilibration in the trapping potential, as shown in Fig. 4.9.

Here the capture was followed by an adiabatic compression of the trap (to $B'_{\mathrm{z}} = 66$ G/cm) to make the measurement consistent. Peak densities for PSD calculation was roughly approximated by assuming a Gaussian *in-situ* spatial distribution and extracting the r.m.s. size from the fits of TOF distribution, in both strong and weak confining directions of the quadrupole, leading to an underestimation of the PSD since equilibrium distributions in linear trapping potentials have larger peak densities. The result shows that the best loading condition is achieved with gradient values between 18 G/cm and 22 G/cm, corresponding to magnetic fields values well below the saturation threshold of the magnetic shield.

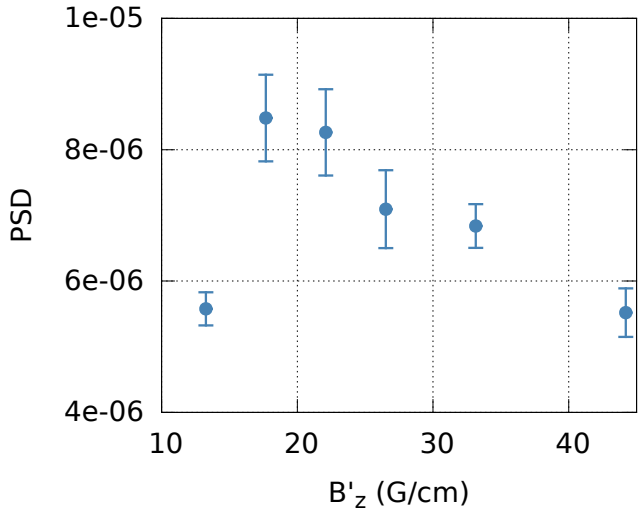

Figure 4.9: Estimated values of PSD of the atoms trapped in the QMT after compression, as a function of the capture gradient.

4.4.2 RF-Sweep, ODT loading

In typical experimental conditions, roughly 1.5×10^9 atoms are captured at a temperature of 30 µK in the QMT operated at 22.1 G/cm, resulting in an elastic collision rate of the order of 1 per second. At this stage the RF evaporation is not efficient. The QMT acts as a reservoir and the comparatively deep ODT, where the sample becomes rapidly collisionally thick, is loaded by elastic collisions as the system reaches thermal equilibrium.

Even in the absence of an efficient evaporation the RF can be used to fix the reservoir temperature against spurious heating effects hence leading to an improvement of the loading efficiency. To this purpose, after the sample is captured in the reservoir, the RF signal is swept in 2.5 s from an initial value of 6.5 MHz to a final value of 4.3 Hz that is kept constant during the loading of the ODT, before being switched off. Figure 4.10 shows the saturated number of atoms, captured in the ODT operated at 7.5 W, as a function of the final RF frequency value. The measurements show a clear effect from the RF signal, that can be explained by considering its effect on the bare atom reservoir, as shown in Fig. 4.11. In the absence of RF, a heating of the sample and the corresponding reduction of the PSD of roughly a factor 2 can be observed, on the loading stage timescale of 10 s. This heating effect can be suppressed by applying the sweep, preserving the initial value of PSD regardless of the small reduction in the atom number.

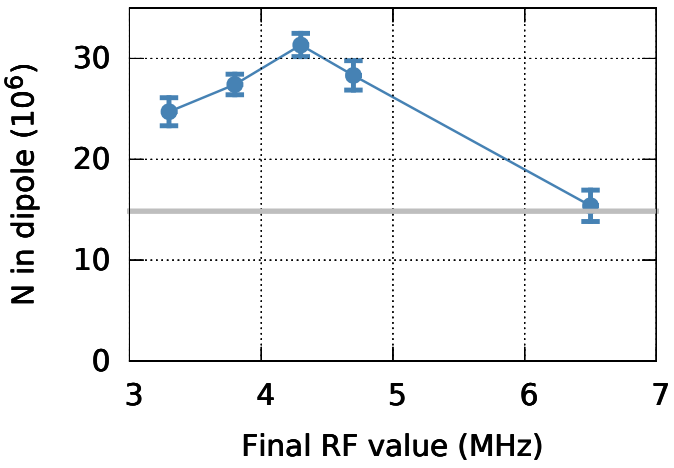

Figure 4.10: Number of atoms in the ODT at the end of the 10 s loading stage, as a function of the final frequency value of the optimized ramp, operating the ODT trap at 7.5 W. The gray line shows the number of atoms loaded in the absence of RF.

4.4.3 Dipole evaporation ramp

Evaporative cooling consists in dynamically reducing the depth of the trap, in order to cut the high-energy tails of the sample distribution, while elastic collisions restore thermal equilibrium, lowering the sample temperature. Generally speaking, the higher the ratio of the trap depth to the sample thermal energy (quantified by the truncation factor $\eta = U_{\mathrm{dip}}/k_{\mathrm{B}}T$), the larger the energy fraction removed by the escaping particle. With an infinite time at disposal, such a process can be arbitrarily efficient. In real situations, however, the evaporation process must be finalized on a timescale short compared to the sample lifetime, and longer than the sample thermalization time, of the order of the inverse of the elastic collision rate $\Gamma_{\mathrm{coll}} \simeq \sigma_0 n v$. The optimized dipole evaporation ramp was experimentally achieved by setting an initial ramp consisting of four segments. In each segment, the ODT power is ramped down to roughly 1/3 of the initial value, mimicking a discrete exponential reduction. The duration of each step, was then optimized independently of the others, at fixed values of the power.

4.4.4 Roboustness to the vertical displacement of the ODT

Typical realizations of condensates in hybrid traps benefit from aligning the ODT beam at a vertical displacement from the quadrupole center, comparable to the beam

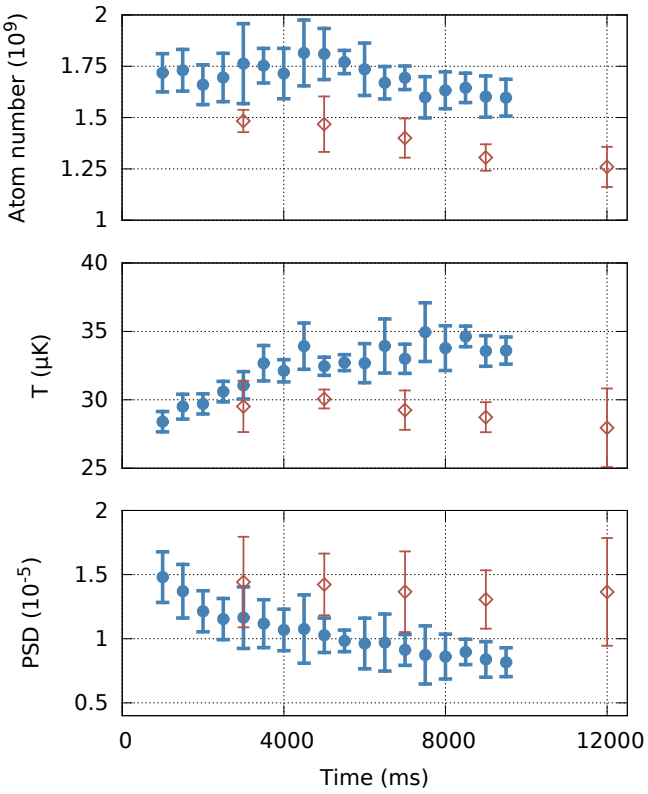

Figure 4.11: Atom number (upper image), temperature (middle) and estimated PSD (lower) for the atoms captured in the QMT operated at 22.1 G/cm, as a function of time, with the RF ramp sequence described in the text, to a final value of 4.3 MHz (red diamonds) or without applying the RF signal (blue dots).

waist, then adiabatically transferring the RF-evaporated sample from the QMT to the ODT. These observations were qualitatively confirmed in our first implementation, described above, which showed a critical behavior with the beam alignment. In the present configuration, such a behavior is not observed. Fig. 4.12 shows the dependence of the number of atoms trapped in the ODT beam after 10 s loading, as a function of the relative displacement z_{dip} (where the zero value indicates the initial beam position, roughly one millimeter below QMT center). Such a dependence is mostly related to the atom density profile of the reservoir. No clear reduction of the loading efficiency is observed trying to superimpose the beam on the QMT center. Also the production of BECs does not seem to be critically affected by the beam alignment, exception made in the close vicinity of QMT center, where a complete loss of the condensate is observed, instead. I did not investigate the evaporation efficiency above the QMT center, where the trapping potential is anti-levitating, since such a characterization is outside of the scope of my work.

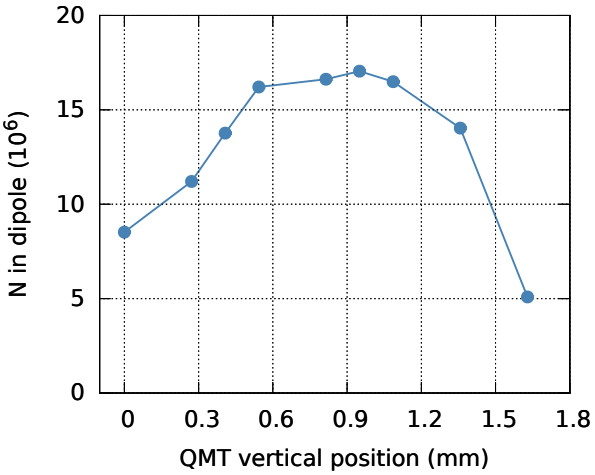

Figure 4.12: Number of atoms captured in the ODT after the 10 s loading phase, as a function of the vertical displacement z_{dip}. The zero value is not referred to the QMT center.

4.5 Optimized production of BEC

4.5.1 Characterization of the experimental sequence

The optimized sequence is shown in Fig. 4.13(a,b,c). The ODT loading phase and evaporation phase are shaded in gray and red, respectively.

Right after gray molasses cooling, the atoms are captured in the combined potential by switching on the QMT at 22.1 G/cm in the presence of the ODT beam, which is operated at 7.5 W, resulting in a ODT trap depth of $U_{\mathrm{d}}/k_{\mathrm{B}} = 475$ µK. Roughly 1.5 10^9 atoms, corresponding to the fraction occupying the $m_{\mathrm{F}} = -1$ Zeeman sublevel, are captured by the QMT at an approximate temperature of 32 µK.

During the 10 s loading stage, the RF frequency value is swept from 6.5 to 4.3 MHz in 2.5 s, then kept constant. The number of atoms captured in the ODT saturates to a value of the order of 3×10^7, with a temperature of the order of 40 µK. The corresponding peak density is above 10^{14} atoms/cm^3, for which three-body inelastic losses start to be relevant. Quantitative results for the atomic sample, at the varius stages of the sequence, are summarized in Table 4.1.

Despite the small transfer efficiency, an increase in PSD of more than three orders of magnitude is observed for the atoms transferred in the ODT. Such an increase, is typically obtained when a deep dimple trap is superimposed to an accordingly larger volume reservoir (either adiabatically [153], or nonadiabatically [154]). The logarithmic trap volume ratio for our configuration can be roughly estimated as $\ln(\sigma_0^2/w_0^2) \sim 7.8$ (where $\sigma_0 \sim 1$ mm, is the approximate size of the reservoir), which allows to take advantage of the large ODT depth, for which $U_{\mathrm{d}}/(k_{\mathrm{B}}T) \simeq 12$.

After switching off the RF at the end of the loading phase, the magnetic field gradient

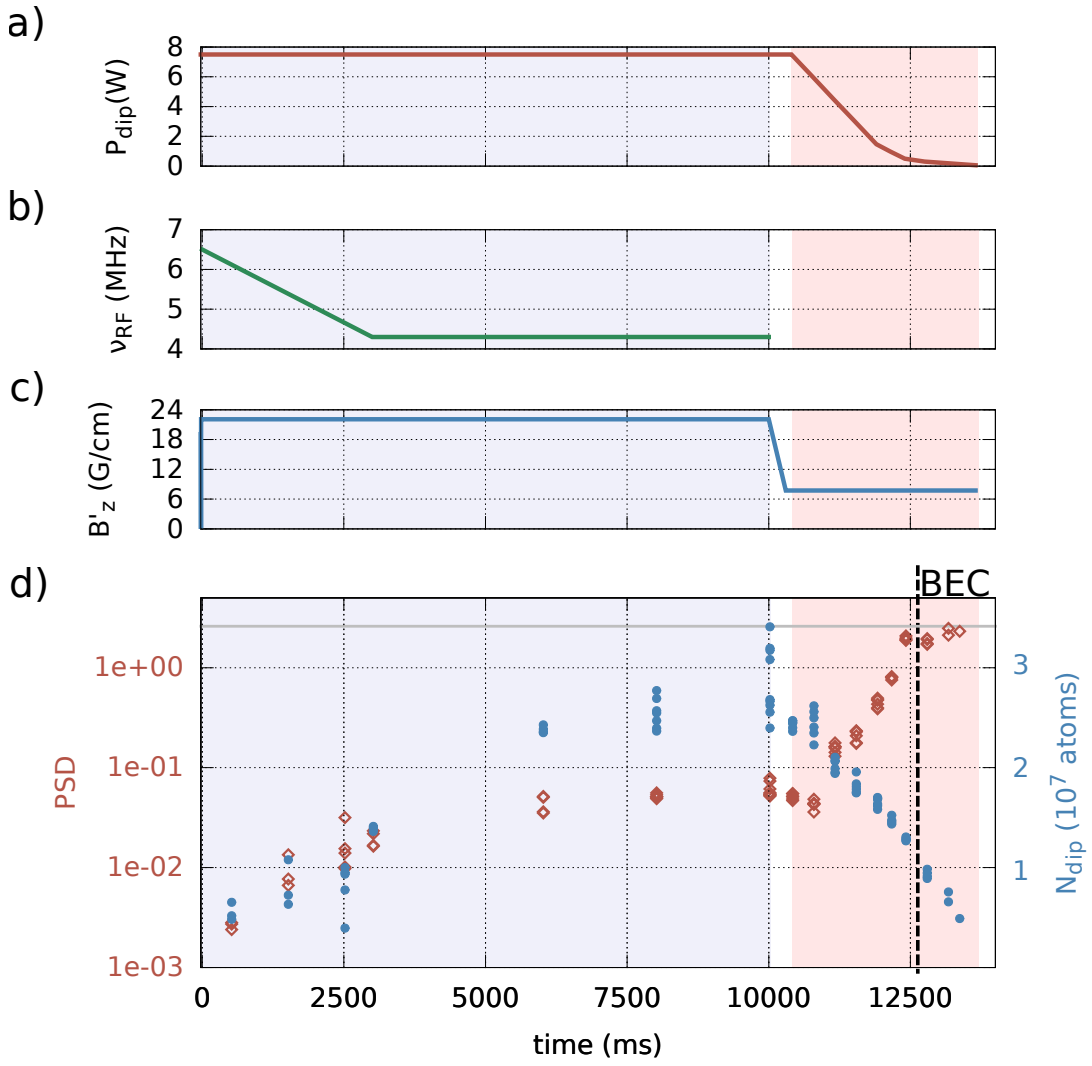

Figure 4.13: **a-c)** Plot of the optimized experimental sequence after atomic capture in the QMT. **d)** Measurements of atom number (blue dots) PSD estimation based on thermal equilibrium hypothesis (red diamonds) for the atoms trapped in the ODT potential dip. Shaded regions refer to the 10 s ODT loading phase (gray) and the dipole evaporation phase (red). The gray line signals the PSD value at the condensation threshold PSD = 2.6. Atom numbers reported after BEC threshold account for the total number, while the PSD value accounts for the thermal part only.

is reduced in 300 ms to a value of 7.74 G/cm, that is below the gravity compensation value $mg/\mu \simeq 8.1$ G/cm, releasing the atoms that are held only by the quadrupole potential reservoir. The sample is then evaporatively cooled in the ODT, for which the initial truncation factor $\eta = U_d/(k_B T) \simeq 13$ is, generally speaking, a favorable condition [155]. The ODT power is ramped down from 7.5 W to $\simeq 60$ mW in 3.25 s,

	N (atoms)	T(µK)	ρ_0(atoms/cm^{-3})	PSD
DSMOT	$4.0(5) \times 10^9$	310(20)	$1.5(4) \times 10^{11}$	$1.1(3) \times 10^{-6}$
GM	$4.14(2) \times 10^9$	14.8(3)	$1.50(7) \times 10^{11}$	$1.04(6) \times 10^{-4}$
QMT loading	$1.46(7) \times 10^9$	32(2)	$5.6(5) \times 10^{10}$	$1.3(2) \times 10^{-5}$
QP after RF ramp	$0.81(5) \times 10^9$	32(3)	$3.9(4) \times 10^{10}$	$0.8(2) \times 10^{-5}$
ODT after RF ramp	$8.5(2) \times 10^6$	40(10)	$8.2(8) \times 10^{13}$	$1.6(9) \times 10^{-2}$
ODT after load	$2.8(3) \times 10^7$	39(2)	$3.1(4) \times 10^{14}$	$6(1) \times 10^{-2}$

Table 4.1: Atom number, temperature, peak density and phase-space density in various stages of the experiment. Shown standard deviations account for statistical errors.

producing an almost pure Bose-Einstein condensate composed of up to 7×10^6 atoms. During the dipole evaporation, the magnetic field gradient is kept at a constant value, contributing to the otherwise weak axial confinement.

The atom number and PSD values of the sample trapped in the ODT, at the various stages of the described procedure, are reported in Fig. 4.13(d). The values of PSD are estimated by measuring the temperatures in TOF and assuming thermal equilibrium in trap, for which PSD $= N(\hbar\bar{\omega})^3/(k_B T)^3$, where $\bar{\omega} = (\omega_{z,y}^2 \omega_x)^{1/3}$ is the geometric average of the trapping frequencies. Trapping frequencies for the different values of ODT power and magnetic field gradients are estimated from the experimentally measured values at given conditions (see subsection 4.3.2), through their dependencies on B'_z and P appearing in equations (4.3) and (4.4). The uncertainty on the computed values of $\bar{\omega}$ is estimated to be of the order 10%, accounting for systematic contributions. In the vicinity or after crossing the BEC transition, the thermal fraction of the imaged distributions in TOF is fitted to a Bose-enhanced Gaussian distribution [104]. The gray line signals the condensation threshold value PSD = 2.6. The agreement between the BEC threshold and the estimated PSD values testifies the overall quality of the calibration (imaging, trapping frequencies).

Evaporation efficiency

The efficiency of the dipole evaporation ramp is characterized through the parameter

$$\gamma_{ev} = -\frac{\mathrm{d}\ln(\mathrm{PSD})}{\mathrm{d}\ln(N)}. \tag{4.6}$$

Using the same data previously shown in Fig. 4.13(d) in correspondence of the ODT evaporation before the onset of condensation, the resulting efficiency value that is obtained by the linear fit showed in Fig. 4.14 is $\gamma_{ev} = 5.8(3)$. Such a value is lower than the one predicted by scaling laws [156] for optical evaporation, considering our truncation factor $\eta = 12.5(15)$, but quite large compared to values typically achieved

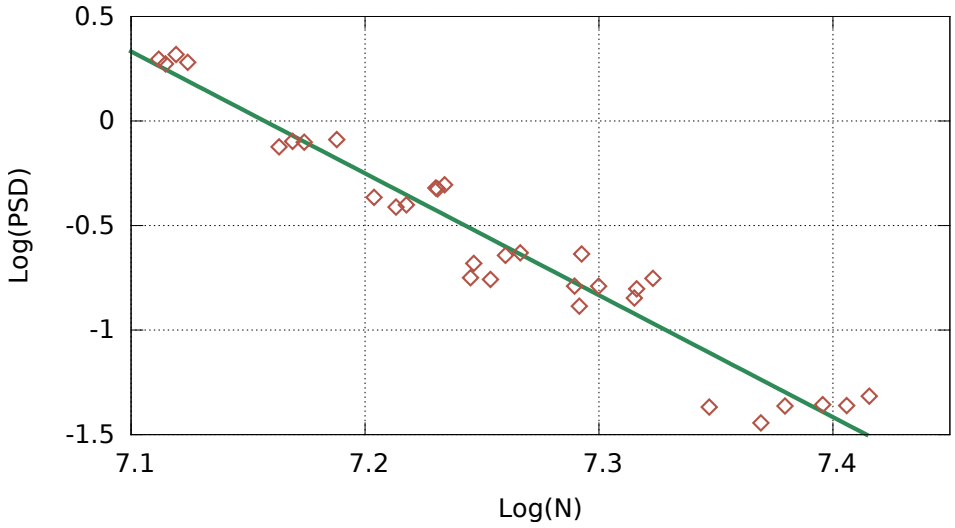

Figure 4.14: Phase space density as a function of atom number, during the evaporation before the onset of Bose-condensation. The green line represents the result of the linear fit.

in the presence of inelastic collisional losses [143, 157], even considering the additional systematic contribution to the error, not accounted for in the fit result. Such an efficient evaporation can be explained considering the QMT gradient contribution to the axial trapping, that remains constant during the evaporation and is not accounted for in scaling laws [156], and the comparatively low inelastic loss rates of Na, compared to other alkali species such as Rb [158]. In addition to this, the effect of gravity on evaporation is negligible due to the magnetic levitation, leading to a 2D evaporation instead of 1D [154, 155].

4.5.2 Condensed fraction

For an ideal gas in a harmonic potential, the condensed fraction scales simply as $N_0/N = 1 - t^3$ where N_0 is the number of atoms in the condensate, and $t = T/T_C^{(0)}$ is the sample temperature, normalized to the ideal gas transition temperature $T_C^{(0)}$

$$T_C^{(0)} = \hbar\bar{\omega}\left(\frac{N}{\zeta(3)}\right)^{1/3}. \tag{4.7}$$

To characterize the system below the critical temperature, I evaporated the sample to different final values of ODT trap depth, before measuring simultaneously the condensed fraction N_0/N (Fig. 4.15(a)), the total atom number N (Fig. 4.15(b)) and the sample temperature T (Fig. 4.15(c)) of the sample. To normalize the measured temperatures, the ideal gas transition temperature $T_C^{(0)}$ is computed for each individual

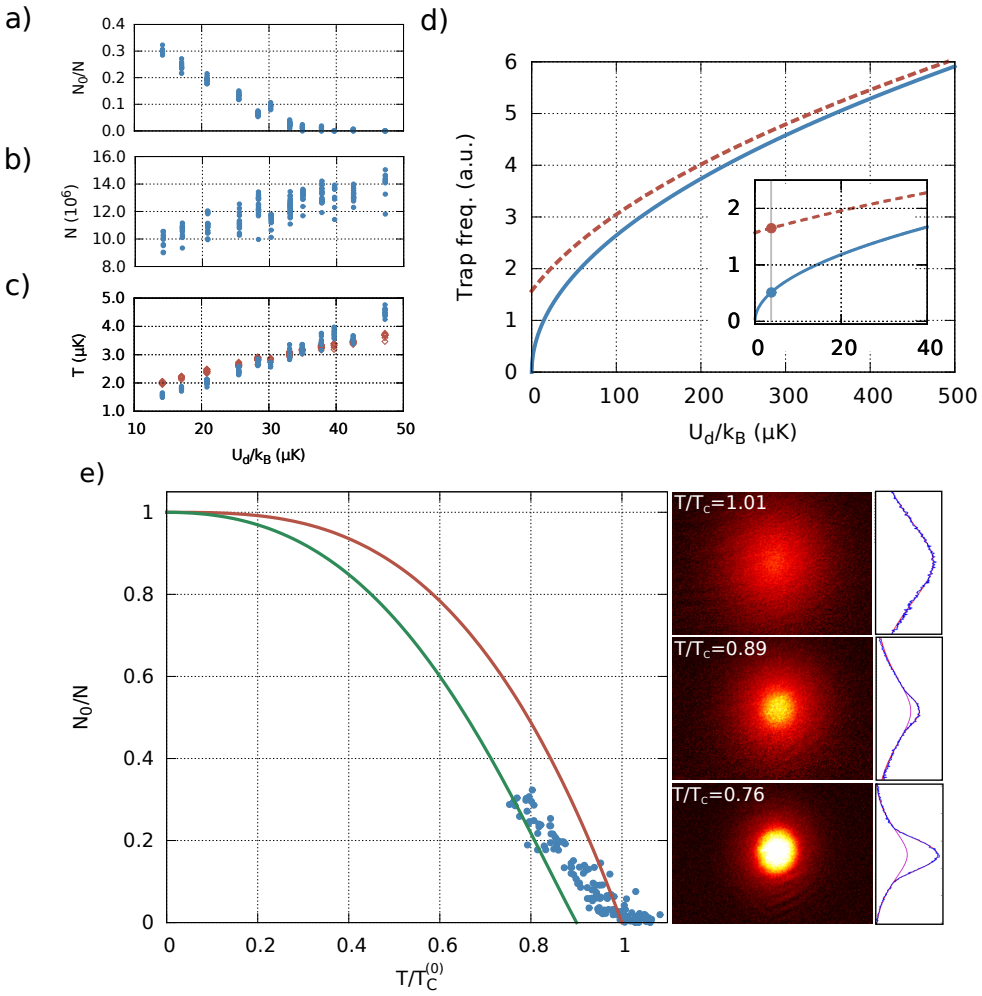

Figure 4.15: Condensed fraction and total atom number as a function of the optical trap depth during evaporation **(a,b)**. Temperature (blue dots) and values of the critical temperature $T_C^{(0)}$ (red diamonds) estimated for each point **(c)**, using the values of trapping frequencies inferred from the dependence on the ODT power, represented in arbitrary units **(d)**. Arbitrary frequency units amount to 1 kHz for the radial trapping (blue line) and to 5 Hz for the axial trapping (red dashed line). The inset shows the scaling behavior at low values of dipole power, where the effect of the residual magnetic confinement is evident. The gray line signals the final power at the end of the evaporation, where the trapping frequencies are experimentally measured. Panel **(e)** shows the condensed fraction as a function of the normalized temperature. The side panel shows absorption image profiles for three different values of the normalized temperature.

data point (also reported Fig. 4.15(c)), using the value $\bar{\omega}$ estimated at different ODT powers, as explained in subsection 4.5.1, and shown in Fig. 4.15(d).

Figure 4.15(e) finally shows the result of this preliminary characterization. As expected [34], as a consequence of repulsive interactions, the experimental points lie below the ideal gas curve. The related corrections to the ideal gas behavior can be quantified through the parameter [34]

$$\eta_{\mathrm{int}} = \frac{\mu}{k_{\mathrm{B}} T_{\mathrm{C}}^{(0)}} \simeq 1.57 \left(N^{1/6} a \sqrt{\frac{m\bar{\omega}}{\hbar}} \right)^{2/5}, \tag{4.8}$$

which amounts to 0.41(1) for the given dataset.

The first effect induced by repulsive interactions is a reduction in the sample peak density, delaying the onset of condensation hence leading to a negative correction to the critical temperature $\delta T_{\mathrm{C}} = -0.43 \eta_{\mathrm{int}}^{5/2} T_{\mathrm{C}}^{0} \simeq 0.04\, T_{\mathrm{C}}^{0}$. Such a small correction is hardly observable in our experimental data, which is in agreement with the expected value within systematic uncertainties.

The other effect arises after the condensation threshold. Mean field interactions in trapped samples tend to spatially separate the thermal fraction from the condensate, leading to a negative correction to the condensed fraction at the lowest order in η_{int} [34]

$$\frac{N_0}{N} = 1 - t^3 - \frac{\zeta(2)}{\zeta(3)} \eta_{\mathrm{int}} t^2 \left(1 - t^3\right)^{2/5}. \tag{4.9}$$

Note that this approximation does not fully account for the system behavior close to T_{C}^{0}, and the resulting curve is also reported in 4.15(d). The experimental points show a crossover behavior, in the region near $T_{\mathrm{C}}^{(0)}$, where (4.9) is not accurate, due to leading higher order contributions, and show a satisfactory agreement with the experimental data. In conclusion, the results presented in this test characterization further confirm the quality of the calibration procedure described in the previous subsections.

4.5.3 Attempts of Bose-condensation without evaporation

As stated earlier, an increase in PSD of several orders of magnitude is obtained by superimposing a dimple trap to a large volume reservoir. This effect already allowed to cross in a reversible manner the quantum degeneracy threshold on a previously RF-evaporated sample by adiabatically reshaping the trap [153]. Given the performance discussed above, one may imagine to push further this method and reach BEC directly via adiabatic compression. To this purpose I made an attempt, by adding a beam orthogonal to the hybrid trap ODT and focused to a waist of the order of 25 µm on the atoms. Switching on the additional trapping potential after the atoms were loaded into the single beam ODT, I was able to observe the signature of a further increase of one order of magnitude in the PSD, for the atoms loaded in the cross trap. These attempts were not pursued further, however, since we understood that reaching quantum degeneracy with temperatures of the order of 40 µK, requires density values for which the sample lifetime would be limited by three-body recombination to tens of ms.

Chapter 5

Conclusions and perspectives

***

In this thesis I report the results obtained during my Ph.D., mainly focusing on the buildup of a new apparatus, aimed to the study of the dynamics of Rabi-coupled Bose-Einstein condensate mixtures involving the $|F = 1, m_F = \pm 1\rangle$ internal states of sodium atoms. This mixture is characterized by the absence of buoyancy, allowing to retain perfect density overlap between the two components, also in harmonic potentials. This property, unexplored so far, is particularly desirable for the study of defects dynamics, and offers us the possibility to investigate the static and the dynamic spin response in the linear regime, in the regimes of near-zero and finite temperature. In the presence of Rabi coupling, novel and exotic defect structures are predicted, including vortex bound-states showing analogies with quark confinement in QCD. Studying the dynamics of such defects requires the internal spin dynamics to maintain coherence at the second timescale, a challenging condition which has not been achieved so far with mixtures whose components are subject to differential linear (Zeeman) magnetic-field dependent energy shifts, as for our sodium mixture. To ensure the necessary magnetic field stability, the apparatus will feature a µ-metal passive magnetic shield.

The magnetic-field sensitivity of the mixture was kept in consideration throughout the buildup of the experiment, from the choice of materials to the experimental protocol to reach quantum degeneracy. In particular, we excluded to reach quantum degeneracy in compressed magnetic traps, to avoid magnetic saturation issues with the µ-metal shield. The other possible protocols benefit from an efficient molasses stage, and to this purpose I successfully implemented and characterized gray molasses cooling on the D1 optical line, obtaining temperatures as low as 9 µK, corresponding to less than 4 recoil temperatures, with an increase of one order of magnitude in phase-space density ($\sim 10^{-4}$) compared to ordinary optical molasses.

I tried to load atoms into an optical dipole trap directly from gray molasses, but eventually quantum degeneracy was achieved through a final evaporation cooling stage in a hybrid magnetic and optical trap. In particular, I explored a regime in which the non-compressed magnetic trap acts as a large volume reservoir, and the comparatively deep optical trap is loaded adiabatically, being the sample at thermal equilibrium. This method allows for an increase of three orders of magnitude in phase-space density, and shows little dependence on the relative alignment of the optical trap beam to the quadrupole trap center. The magnetic gradient also contributes to the single beam

axial trapping and compensates for the effect of gravity during optical evaporation, boosting its efficiency and allowing to reliably produce condensates with up to 7×10^6 atoms.

With the protocol to reach quantum degeneracy in hand, that is the main result of my doctorate, we are able to move towards the production of coherently coupled mixtures in condition of high magnetic field stability. In paticular, shorter term perspectives compatible with the actual trap geometry include the observation of the magnetic soliton in the presence of Rabi coupling, and the study of its dynamical properties. Another perspective in the presence of Rabi coupling is the study of the dynamics bound states of vortices in the two different components, vortex lattice configurations, and spin-orbit coupled Bose-Einstein condensates

Bibliography

***

[1] M. M. Salomaa and G. E. Volovik, "Quantized vortices in superfluid ^{3}He," *Rev. Mod. Phys.*, vol. 59, pp. 533–613, 1987. (cited on pp. 10 and 17)

[2] A. Knigavko and B. Rosenstein, "Magnetic skyrmion lattices in heavy fermion superconductor upt$_3$," *Phys. Rev. Lett.*, vol. 82, pp. 1261–1264, 1999. (cited on p. 10)

[3] B. Rosenstein, I. Shapiro, B. Y. Shapiro, and G. Bel, "Vector vortices in p-wave superconductors with arbitrary κ parameter," *Phys. Rev. B*, vol. 67, p. 224507, Jun 2003. (cited on p. 10)

[4] G. S. M., "Spin and isospin: exotic order in quantum hall ferromagnets," *Phys. Today*, vol. 53, p. 39–45, 2000. (cited on p. 10)

[5] R. Fazio and H. van der Zant, "Quantum phase transitions and vortex dynamics in superconducting networks," *Physics Reports*, vol. 355, no. 4, pp. 235 – 334, 2001. (cited on p. 10)

[6] K. Kasamatsu, M. Tsubota, and M. Ueda, "Vortices in multicomponent Bose-Einstein condensates," *International Journal of Modern Physics B*, vol. 19, no. 11, pp. 1835–1904, 2005. (cited on pp. 10, 14, and 17)

[7] U. Leonhardt and G. E. Volovik, "How to create an alice string (half-quantum vortex) in a vector Bose-Einstein condensate," *Journal of Experimental and Theoretical Physics Letters*, vol. 72, no. 2, pp. 46–48, 2000. (cited on pp. 10 and 14)

[8] E. J. Mueller, "Spin textures in slowly rotating Bose-Einstein condensates," *Phys. Rev. A*, vol. 69, p. 033606, 2004. (cited on pp. 10 and 14)

[9] Y. Kawaguchi, M. Kobayashi, M. Nitta, and M. Ueda, "Topological excitations in spinor Bose-Einstein condensates," *Progress of Theoretical Physics Supplement*, vol. 186, pp. 455–462, 2010. (cited on p. 10)

[10] M. Ueda, "Topological aspects in spinor bose–einstein condensates," *Reports on Progress in Physics*, vol. 77, no. 12, p. 122401, 2014. (cited on p. 10)

[11] D. M. Stamper-Kurn and M. Ueda, "Spinor bose gases: Symmetries, magnetism, and quantum dynamics," *Rev. Mod. Phys.*, vol. 85, pp. 1191–1244, 2013. (cited on p. 10)

[12] F. Schreck, L. Khaykovich, K. L. Corwin, G. Ferrari, T. Bourdel, J. Cubizolles, and C. Salomon, "Quasipure Bose-Einstein condensate immersed in a fermi sea," *Phys. Rev. Lett.*, vol. 87, p. 080403, Aug 2001. (cited on p. 10)

[13] M. Modugno, C. Fort, P. Maddaloni, F. Minardi, and M. Inguscio, "Damping and frequency shift in the oscillations of two colliding Bose-Einstein condensates," *The European Physical Journal D - Atomic, Molecular, Optical and Plasma Physics*, vol. 17, no. 3, pp. 345–349, 2001. (cited on p. 10)

[14] F. Ferlaino, R. J. Brecha, P. Hannaford, F. Riboli, G. Roati, G. Modugno, and M. Inguscio, "Dipolar oscillations in a quantum degenerate fermi–bose atomic mixture," *Journal of Optics B: Quantum and Semiclassical Optics*, vol. 5, no. 2, p. S3, 2003. (cited on p. 10)

[15] I. Ferrier-Barbut, M. Delehaye, S. Laurent, A. T. Grier, M. Pierce, B. S. Rem, F. Chevy, and C. Salomon, "A mixture of bose and fermi superfluids," *Science*, vol. 345, no. 6200, pp. 1035–1038, 2014. (cited on p. 10)

[16] R. Roy, A. Green, R. Bowler, and S. Gupta, "Two-element mixture of bose and fermi superfluids," *Phys. Rev. Lett.*, vol. 118, p. 055301, 2017. (cited on p. 10)

[17] P. Maddaloni, M. Modugno, C. Fort, F. Minardi, and M. Inguscio, "Collective oscillations of two colliding Bose-Einstein condensates," *Phys. Rev. Lett.*, vol. 85, pp. 2413–2417, 2000. (cited on p. 10)

[18] G. Modugno, M. Modugno, F. Riboli, G. Roati, and M. Inguscio, "Two atomic species superfluid," *Phys. Rev. Lett.*, vol. 89, p. 190404, 2002. (cited on p. 10)

[19] K. Jiménez-García, L. J. LeBlanc, R. A. Williams, M. C. Beeler, C. Qu, M. Gong, C. Zhang, and I. B. Spielman, "Tunable spin-orbit coupling via strong driving in ultracold-atom systems," *Phys. Rev. Lett.*, vol. 114, p. 125301, 2015. (cited on p. 10)

[20] T. Bienaimé, E. Fava, G. Colzi, C. Mordini, S. Serafini, C. Qu, S. Stringari, G. Lamporesi, and G. Ferrari, "Spin-dipole oscillation and polarizability of a binary Bose-Einstein condensate near the miscible-immiscible phase transition," *Phys. Rev. A*, vol. 94, p. 063652, 2016. (cited on pp. 10 and 15)

[21] S. B. Koller, A. Groot, P. C. Bons, R. A. Duine, H. T. C. Stoof, and P. van der Straten, "Quantum enhancement of spin drag in a bose gas," *New Journal of Physics*, vol. 17, no. 11, p. 113026, 2015. (cited on p. 10)

[22] G. Semeghini, G. Ferioli, L. Masi, C. Mazzinghi, L. Wolswijk, F. Minardi, M. Modugno, G. Modugno, M. Inguscio, and M. Fattori, "Self-bound quantum droplets in atomic mixtures," *ArXiv e-prints*, 2017. (cited on p. 10)

[23] P. Cheiney, C. R. Cabrera, J. Sanz, B. Naylor, L. Tanzi, and L. Tarruell, "Bright soliton to quantum droplet transition in a mixture of Bose-Einstein condensates," *ArXiv e-prints*, 2017. (cited on p. 10)

[24] C. J. Myatt, E. A. Burt, R. W. Ghrist, E. A. Cornell, and C. E. Wieman, "Production of two overlapping Bose-Einstein condensates by sympathetic cooling," *Phys. Rev. Lett.*, vol. 78, pp. 586–589, 1997. (cited on p. 10)

[25] D. S. Hall, M. R. Matthews, J. R. Ensher, C. E. Wieman, and E. A. Cornell, "Dynamics of component separation in a binary mixture of Bose-Einstein condensates," *Phys. Rev. Lett.*, vol. 81, pp. 1539–1542, 1998. (cited on pp. 10 and 13)

[26] C. Hamner, J. J. Chang, P. Engels, and M. A. Hoefer, "Generation of dark-bright soliton trains in superfluid-superfluid counterflow," *Phys. Rev. Lett.*, vol. 106, p. 065302, 2011. (cited on p. 10)

[27] E. Nicklas, H. Strobel, T. Zibold, C. Gross, B. A. Malomed, P. G. Kevrekidis, and M. K. Oberthaler, "Rabi flopping induces spatial demixing dynamics," *Phys. Rev. Lett.*, vol. 107, p. 193001, 2011. (cited on pp. 10 and 19)

[28] E. Nicklas, W. Muessel, H. Strobel, P. G. Kevrekidis, and M. K. Oberthaler, "Nonlinear dressed states at the miscibility-immiscibility threshold," *Phys. Rev. A*, vol. 92, p. 053614, 2015. (cited on p. 10)

[29] S. Pitaevskii, Lev Petrovitch; Stringari, *Bose-Einstein Condensation and Superfluidity*. International series of monographs on physics 164, Oxford University Press, 1 ed., 2016. (cited on pp. 10 and 12)

[30] A. Andreev and E. Bashkin, "Three-velocity hydrodynamics of superfluid solutions," *Soviet Journal of Experimental and Theoretical Physics*, vol. 42, p. 164, 1976. (cited on p. 11)

[31] J. Nespolo, G. E. Astrakharchik, and A. Recati, "Andreev–bashkin effect in superfluid cold gases mixtures," *New Journal of Physics*, vol. 19, no. 12, p. 125005, 2017. (cited on p. 11)

[32] M. Abad and A. Recati, "A study of coherently coupled two-component Bose-Einstein condensates," *The European Physical Journal D*, vol. 67, no. 7, p. 148, 2013. (cited on pp. 12, 14, and 19)

[33] K. L. Lee, N. B. Jørgensen, I.-K. Liu, L. Wacker, J. J. Arlt, and N. P. Proukakis, "Phase separation and dynamics of two-component Bose-Einstein condensates," *Phys. Rev. A*, vol. 94, p. 013602, 2016. (cited on p. 12)

[34] F. Dalfovo, S. Giorgini, L. P. Pitaevskii, and S. Stringari, "Theory of Bose-Einstein condensation in trapped gases," *Rev. Mod. Phys.*, vol. 71, pp. 463–512, 1999. (cited on pp. 13 and 88)

[35] A. Recati and S. Stringari, "Spin fluctuations, susceptibility, and the dipole oscillation of a nearly ferromagnetic fermi gas," *Phys. Rev. Lett.*, vol. 106, p. 080402, 2011. (cited on p. 14)

[36] R. N. Bisset, R. M. Wilson, and C. Ticknor, "Scaling of fluctuations in a trapped binary condensate," *Phys. Rev. A*, vol. 91, p. 053613, 2015. (cited on p. 14)

[37] S. Knoop, T. Schuster, R. Scelle, A. Trautmann, J. Appmeier, M. K. Oberthaler, E. Tiesinga, and E. Tiemann, "Feshbach spectroscopy and analysis of the interaction potentials of ultracold sodium," *Phys. Rev. A*, vol. 83, p. 042704, 2011. (cited on p. 14)

[38] M. R. Matthews, B. P. Anderson, P. C. Haljan, D. S. Hall, C. E. Wieman, and E. A. Cornell, "Vortices in a Bose-Einstein condensate," *Phys. Rev. Lett.*, vol. 83, pp. 2498–2501, 1999. (cited on pp. 14, 16, 17, and 18)

[39] E. Fava, T. Bienaimé, C. Mordini, G. Colzi, C. Qu, S. Stringari, G. Lamporesi, and G. Ferrari, "Spin Superfluidity of a Bose Gas Mixture at Finite Temperature." arXiv:1708.03923 [cond-mat.quant-gas], 2017. (cited on p. 15)

[40] E. Fava, *Static and Dynamics properties of a miscible two-component Bose-Einstein Condensates*. PhD thesis, Università degi studi di Trento, 2018. (cited on pp. 15, 23, 37, 67, and 68)

[41] A. Sartori, J. Marino, S. Stringari, and A. Recati, "Spin-dipole oscillation and relaxation of coherently coupled bose–einstein condensates," *New Journal of Physics*, vol. 17, no. 9, p. 093036, 2015. (cited on pp. 15 and 19)

[42] D. M. Jezek and P. Capuzzi, "Interaction-driven effects on two-component Bose-Einstein condensates," *Phys. Rev. A*, vol. 66, p. 015602, 2002. (cited on p. 15)

[43] D. M. Stamper-Kurn, H.-J. Miesner, S. Inouye, M. R. Andrews, and W. Ketterle, "Collisionless and hydrodynamic excitations of a Bose-Einstein condensate," *Phys. Rev. Lett.*, vol. 81, pp. 500–503, 1998. (cited on p. 16)

[44] G. A. Swartzlander and C. T. Law, "Optical vortex solitons observed in kerr nonlinear media," *Phys. Rev. Lett.*, vol. 69, pp. 2503–2506, 1992. (cited on p. 16)

[45] R. L. Davis and E. P. S. Shellard, "Global strings and superfluid vortices," *Phys. Rev. Lett.*, vol. 63, pp. 2021–2024, 1989. (cited on p. 16)

[46] "Global strings and superfluid vortices: Analogies and differences," *Nuclear Physics B*, vol. 338, no. 2, pp. 371 – 385, 1990. (cited on p. 16)

[47] K. W. Madison, F. Chevy, W. Wohlleben, and J. Dalibard, "Vortex formation in a stirred Bose-Einstein condensate," *Phys. Rev. Lett.*, vol. 84, pp. 806–809, 2000. (cited on p. 16)

[48] E. Hodby, G. Hechenblaikner, S. A. Hopkins, O. M. Maragò, and C. J. Foot, "Vortex nucleation in Bose-Einstein condensates in an oblate, purely magnetic potential," *Phys. Rev. Lett.*, vol. 88, p. 010405, 2001. (cited on p. 16)

[49] A. Fetter, "Rotating trapped Bose-Einstein condensates," *Rev. Mod. Phys.*, vol. 81, p. 647, 2009. (cited on p. 16)

[50] J. Abo-Shaeer, C. Raman, J. Vogels, and W. Ketterle, "Observation of vortex lattices in Bose-Einstein condensates," *Science*, vol. 292, pp. 476–479, 2001. (cited on p. 16)

[51] "The direct observation of individual flux lines in type ii superconductors," *Physics Letters A*, vol. 24, no. 10, pp. 526 – 527, 1967. (cited on p. 17)

[52] I. Coddington, P. Engels, V. Schweikhard, and E. A. Cornell, "Observation of tkachenko oscillations in rapidly rotating Bose-Einstein condensates," *Phys. Rev. Lett.*, vol. 91, p. 100402, 2003. (cited on p. 17)

[53] V. M. Pérez-García and J. J. García-Ripoll, "Two-mode theory of vortex stability in multicomponent Bose-Einstein condensates," *Phys. Rev. A*, vol. 62, p. 033601, 2000. (cited on p. 17)

[54] D. V. Skryabin, "Instabilities of vortices in a binary mixture of trapped Bose-Einstein condensates: Role of collective excitations with positive and negative energies," *Phys. Rev. A*, vol. 63, p. 013602, 2000. (cited on p. 17)

[55] M. Eto, K. Kasamatsu, M. Nitta, H. Takeuchi, and M. Tsubota, "Interaction of half-quantized vortices in two-component Bose-Einstein condensates," *Phys. Rev. A*, vol. 83, p. 063603, 2011. (cited on p. 17)

[56] V. Schweikhard, I. Coddington, P. Engels, S. Tung, Cornell, and E. A., "Vortex-lattice dynamics in rotating spinor Bose-Einstein condensates," *Phys. Rev. Lett.*, vol. 93, p. 210403, 2004. (cited on p. 17)

[57] L. Brey, H. A. Fertig, R. Côté, and A. H. MacDonald, "Skyrme crystal in a two-dimensional electron gas," *Phys. Rev. Lett.*, vol. 75, pp. 2562–2565, 1995. (cited on p. 17)

[58] K. Kasamatsu, M. Tsubota, and M. Ueda, "Vortex phase diagram in rotating two-component Bose-Einstein condensates," *Phys. Rev. Lett.*, vol. 91, p. 150406, 2003. (cited on p. 17)

[59] L. Khaykovich, F. Schreck, G. Ferrari, T. Bourdel, J. Cubizolles, L. D. Carr, Y. Castin, and C. Salomon, "Formation of a matter-wave bright soliton," *Science*, vol. 296, no. 5571, pp. 1290–1293, 2002. (cited on p. 17)

[60] S. Burger, K. Bongs, S. Dettmer, W. Ertmer, K. Sengstock, A. Sanpera, G. V. Shlyapnikov, and M. Lewenstein, "Dark solitons in Bose-Einstein condensates," *Phys. Rev. Lett.*, vol. 83, pp. 5198–5201, 1999. (cited on p. 17)

[61] J. Denschlag, J. E. Simsarian, D. L. Feder, C. W. Clark, L. A. Collins, J. Cubizolles, L. Deng, E. W. Hagley, K. Helmerson, W. P. Reinhardt, S. L. Rolston, B. I. Schneider, and W. D. Phillips, "Generating solitons by phase engineering of a Bose-Einstein condensate," *Science*, vol. 287, no. 5450, pp. 97–101, 2000. (cited on p. 17)

[62] T. Busch and J. R. Anglin, "Dark-bright solitons in inhomogeneous Bose-Einstein condensates," *Phys. Rev. Lett.*, vol. 87, p. 010401, 2001. (cited on p. 17)

[63] P. Kevrekidis and D. Frantzeskakis, "Solitons in coupled nonlinear schrödinger models: A survey of recent developments," *Reviews in Physics*, vol. 1, pp. 140 – 153, 2016. (cited on p. 17)

[64] Z. Chen, M. Segev, T. H. Coskun, D. N. Christodoulides, and Y. S. Kivshar, "Coupled photorefractive spatial-soliton pairs," *J. Opt. Soc. Am. B*, vol. 14, no. 11, pp. 3066–3077, 1997. (cited on p. 17)

[65] C. Qu, L. P. Pitaevskii, and S. Stringari, "Magnetic solitons in a binary Bose-Einstein condensate," *Phys. Rev. Lett.*, vol. 116, p. 160402, 2016. (cited on pp. 17 and 21)

[66] A. M. Kamchatnov and L. P. Pitaevskii, "Stabilization of solitons generated by a supersonic flow of Bose-Einstein condensate past an obstacle," *Phys. Rev. Lett.*, vol. 100, p. 160402, 2008. (cited on p. 17)

[67] I. Danaila, M. A. Khamehchi, V. Gokhroo, P. Engels, and P. G. Kevrekidis, "Vector dark-antidark solitary waves in multicomponent Bose-Einstein condensates," *Phys. Rev. A*, vol. 94, p. 053617, 2016. (cited on p. 18)

[68] C. Gross, T. Zibold, E. Nicklas, J. Estève, and M. K. Oberthaler, "Nonlinear atom interferometer surpasses classical precision limit," *Nature*, vol. 464, pp. 1165 EP –, 2010. (cited on p. 18)

[69] S. Butera, P. Öhberg, and I. Carusotto, "Black-hole lasing in coherently coupled two-component atomic condensates," *Phys. Rev. A*, vol. 96, p. 013611, 2017. (cited on p. 18)

[70] A. Cappellaro, T. Macrì, G. F. Bertacco, and L. Salasnich, "Equation of state and self-bound droplet in rabi-coupled bose mixtures," *Scientific Reports*, vol. 7, no. 1, p. 13358, 2017. (cited on p. 18)

[71] A. Smerzi, S. Fantoni, S. Giovanazzi, and S. R. Shenoy, "Quantum coherent atomic tunneling between two trapped Bose-Einstein condensates," *Phys. Rev. Lett.*, vol. 79, pp. 4950–4953, 1997. (cited on p. 19)

[72] M. Abad, "Persistent currents in coherently coupled Bose-Einstein condensates in a ring trap," *Phys. Rev. A*, vol. 93, p. 033603, 2016. (cited on p. 19)

[73] D. T. Son and M. A. Stephanov, "Domain walls of relative phase in two-component Bose-Einstein condensates," *Phys. Rev. A*, vol. 65, p. 063621, 2002. (cited on pp. 19 and 21)

[74] C. Qu, M. Tylutki, S. Stringari, and L. P. Pitaevskii, "Magnetic solitons in Rabi-coupled Bose-Einstein condensates," *Phys. Rev. A*, vol. 95, p. 033614, 2017. (cited on p. 21)

[75] T. Busch and J. Anglin, "Motion of dark solitons in trapped Bose-Einstein condensates," *Phys. Rev. Lett.*, vol. 84, p. 2298, 2000. (cited on p. 21)

[76] V. V. Konotop and L. Pitaevskii, "Landau dynamics of a grey soliton in a trapped condensate," *Phys. Rev. Lett.*, vol. 93, p. 240403, 2004. (cited on p. 21)

[77] M. Tylutki, L. P. Pitaevskii, A. Recati, and S. Stringari, "Confinement and precession of vortex pairs in coherently coupled Bose-Einstein condensates," *Phys. Rev. A*, vol. 93, p. 043623, Apr 2016. (cited on pp. 21 and 22)

[78] K. Kasamatsu, M. Tsubota, and M. Ueda, "Vortex molecules in coherently coupled two-component Bose-Einstein condensates," *Phys. Rev. Lett.*, vol. 93, p. 250406, 2004. (cited on pp. 21 and 22)

[79] A. Polyakov, "Quark confinement and topology of gauge theories," *Nuclear Physics B*, vol. 120, no. 3, pp. 429 – 458, 1977. (cited on p. 22)

[80] Y. Kondo, J. S. Korhonen, M. Krusius, V. V. Dmitriev, E. V. Thuneberg, and G. E. Volovik, "Combined spin-mass vortex with soliton tail in superfluid ^3B," *Phys. Rev. Lett.*, vol. 68, pp. 3331–3334, 1992. (cited on p. 22)

[81] M. Tylutki, S. Donadello, S. Serafini, L. P. Pitaevskii, F. Dalfovo, G. Lamporesi, and G. Ferrari, "Solitonic vortices in Bose-Einstein condensates," *Eur. Phys. J. Special Topics*, vol. 224, no. 3, pp. 577–583, 2015. (cited on p. 22)

[82] M. Eto and M. Nitta, "Confinement of half-quantized vortices in coherently coupled Bose-Einstein condensates: Simulating quark confinement in a QCD-like theory," *Phys. Rev. A*, vol. 97, p. 023613, 2018. (cited on p. 22)

[83] L. Calderaro, A. L. Fetter, P. Massignan, and P. Wittek, "Vortex dynamics in coherently coupled Bose-Einstein condensates," *Phys. Rev. A*, vol. 95, p. 023605, 2017. (cited on p. 22)

[84] A. Gallemí, A. M. Mateo, R. Mayol, and M. Guilleumas, "Coherent quantum phase slip in two-component bosonic atomtronic circuits," *New Journal of Physics*, vol. 18, no. 1, p. 015003, 2016. (cited on p. 22)

[85] M. Cipriani and M. Nitta, "Crossover between integer and fractional vortex lattices in coherently coupled two-component Bose-Einstein condensates," *Phys. Rev. Lett.*, vol. 111, p. 170401, 2013. (cited on p. 23)

[86] M. Nitta, M. Eto, and M. Cipriani, "Vortex molecules in Bose-Einstein condensates," *Journal of Low Temperature Physics*, vol. 175, no. 1, pp. 177–188, 2014. (cited on p. 23)

[87] M. Kobayashi and M. Nitta, "Vortex polygons and their stabilities in Bose-Einstein condensates and field theory," *Journal of Low Temperature Physics*, vol. 175, no. 1, pp. 208–215, 2014. (cited on p. 23)

[88] A. Aftalion and P. Mason, "Rabi-coupled two-component Bose-Einstein condensates: Classification of the ground states, defects, and energy estimates," *Phys. Rev. A*, vol. 94, p. 023616, 2016. (cited on p. 23)

[89] D. M. Harber, H. J. Lewandowski, J. M. McGuirk, and E. A. Cornell, "Effect of cold collisions on spin coherence and resonance shifts in a magnetically trapped ultracold gas," *Phys. Rev. A*, vol. 66, p. 053616, 2002. (cited on p. 23)

[90] P. Treutlein, P. Hommelhoff, T. Steinmetz, T. W. Hänsch, and J. Reichel, "Coherence in microchip traps," *Phys. Rev. Lett.*, vol. 92, p. 203005, 2004. (cited on p. 23)

[91] C. Deutsch, F. Ramirez-Martinez, C. Lacroûte, F. Reinhard, T. Schneider, J. N. Fuchs, F. Piéchon, F. Laloë, J. Reichel, and P. Rosenbusch, "Spin self-rephasing and very long coherence times in a trapped atomic ensemble," *Phys. Rev. Lett.*, vol. 105, p. 020401, 2010. (cited on p. 23)

[92] G. Kleine Büning, J. Will, W. Ertmer, E. Rasel, J. Arlt, C. Klempt, F. Ramirez-Martinez, F. Piéchon, and P. Rosenbusch, "Extended coherence time on the clock transition of optically trapped rubidium," *Phys. Rev. Lett.*, vol. 106, p. 240801, 2011. (cited on p. 23)

[93] P. D. Lett, W. D. Phillips, S. L. Rolston, C. E. Tanner, R. N. Watts, and C. I. Westbrook, "Optical molasses," *J. Opt. Soc. Am. B*, vol. 6, no. 11, pp. 2084–2107, 1989. (cited on p. 34)

[94] W. D. Phillips, "Nobel lecture: Laser cooling and trapping of neutral atoms," *Rev. Mod. Phys.*, vol. 70, pp. 721–741, 1998. (cited on p. 34)

[95] T. W. Hansch and B. Couillaud, "Laser frequency stabilization by polarization spectroscopy of a reflecting reference cavity," *Optics Communications*, vol. 35, pp. 441–444, 1980. (cited on p. 35)

[96] L. Ricci, M. Weidemüller, T. Esslinger, A. Hemmerich, C. Zimmermann, V. Vuletic, W. König, and T. Hänsch, "A compact grating-stabilized diode laser system for atomic physics," *Optics Communications*, vol. 117, no. 5–6, pp. 541 – 549, 1995. (cited on p. 36)

[97] T. G. Tiecke, S. D. Gensemer, A. Ludewig, and J. T. M. Walraven, "High-flux two-dimensional magneto-optical-trap source for cold lithium atoms," *Physical Review A*, vol. 80, no. 1, p. 013409, 2009. (cited on p. 41)

[98] G. Lamporesi, S. Donadello, S. Serafini, and G. Ferrari, "Compact high-flux source of cold sodium atoms," *Rev. Sci. Instrum.*, vol. 84, no. 6, p. 063102, 2013. (cited on pp. 41, 43, and 51)

[99] I. Nosske, L. Couturier, F. Hu, C. Tan, C. Qiao, J. Blume, Y. H. Jiang, P. Chen, and M. Weidemüller, "Two-dimensional magneto-optical trap as a source for cold strontium atoms," *Phys. Rev. A*, vol. 96, p. 053415, 2017. (cited on p. 41)

[100] W. Ketterle, K. Davis, M. Joffe, A. Martin, and D. Pritchard, "High densities of cold atoms in a dark spontaneous-force optical trap," *Physical review letters*, vol. 70, no. 15, pp. 2253–2256, 1993. (cited on pp. 42 and 52)

[101] M. Prentiss, E. L. Raab, D. E. Pritchard, A. Cable, J. E. Bjorkholm, and S. Chu, "Atomic-density-dependent losses in an optical trap," *Opt. Lett.*, vol. 13, no. 6, pp. 452–454, 1988. (cited on p. 42)

[102] L. Marcassa, V. Bagnato, Y. Wang, C. Tsao, J. Weiner, O. Dulieu, Y. B. Band, and P. S. Julienne, "Collisional loss rate in a magneto-optical trap for sodium atoms: Light-intensity dependence," *Phys. Rev. A*, vol. 47, pp. R4563–R4566, 1993. (cited on p. 42)

[103] T. Walker, D. Sesko, and C. Wieman, "Collective behavior of optically trapped neutral atoms," *Phys. Rev. Lett.*, vol. 64, pp. 408–411, 1990. (cited on p. 42)

[104] W. Ketterle, D. S. Durfee, and D. M. Stamper-kurn, "Making, probing and understanding Bose-Einstein condensates," in *PROCEEDINGS OF THE INTERNATIONAL SCHOOL OF PHYSICS "ENRICO FERMI", COURSE CXL, EDITED BY M. INGUSCIO, S. STRINGARI AND C.E. WIEMAN (IOS*, p. 67, Press, 1999. (cited on pp. 45 and 85)

[105] M. R. Andrews, M.-O. Mewes, N. J. van Druten, D. S. Durfee, D. M. Kurn, and W. Ketterle, "Direct, nondestructive observation of a bose condensate," *Science*, vol. 273, no. 5271, pp. 84–87, 1996. (cited on p. 47)

[106] Y. Castin and R. Dum, "Bose-Einstein condensates in time dependent traps," *Phys. Rev. Lett.*, vol. 77, pp. 5315–5319, 1996. (cited on p. 48)

[107] G. Colzi, G. Durastante, E. Fava, S. Serafini, G. Lamporesi, and G. Ferrari, "Sub-doppler cooling of sodium atoms in gray molasses," *Phys. Rev. A*, vol. 93, no. 023421, 2016. (cited on pp. 51 and 55)

[108] P. D. Lett, R. N. Watts, C. I. Westbrook, W. D. Phillips, P. L. Gould, and H. J. Metcalf, "Observation of atoms laser cooled below the doppler limit," *Phys. Rev. Lett.*, vol. 61, pp. 169–172, 1988. (cited on p. 51)

[109] J. Dalibard and C. Cohen-Tannoudji, "Laser cooling below the Doppler limit by polarization gradients: simple theoretical models," *J. Opt. Soc. Am. B*, vol. 6, no. 11, pp. 2023–2045, 1989. (cited on p. 52)

[110] P. J. Ungar, D. S. Weiss, E. Riis, and S. Chu, "Optical molasses and multilevel atoms: theory," *J. Opt. Soc. Am. B*, vol. 6, no. 11, pp. 2058–2071, 1989. (cited on p. 52)

[111] M. Kasevich and S. Chu, "Laser cooling below a photon recoil with three-level atoms," *Phys. Rev. Lett.*, vol. 69, pp. 1741–1744, Sep 1992. (cited on p. 52)

[112] M. Landini, S. Roy, L. Carcagnì, D. Trypogeorgos, M. Fattori, M. Inguscio, and G. Modugno, "Sub-Doppler laser cooling of potassium atoms," *Phys. Rev. A*, vol. 84, p. 043432, 2011. (cited on p. 52)

[113] L. M. G. Alzetta, A. Gozzini and G. Orriols, "An experimental method for the observation of R.F. transitions and laser beat resonances in oriented Na vapour.," *Il Nuovo Cimento*, vol. 36B, pp. 5–20, 1976. (cited on p. 52)

[114] E. Arimondo and G. Orriols, "Nonabsorblng atomic coherences by coherent two-photon transitions in a three-level optical pumping.," *Lett. ll Nuovo Cimento*, vol. 17, pp. 333–338, 1976. (cited on p. 52)

[115] M. Fleischhauer, A. Imamoglu, and J. P. Marangos, "Electromagnetically induced transparency: Optics in coherent media," *Rev. Mod. Phys.*, vol. 77, pp. 633–673, 2005. (cited on p. 53)

[116] F. Papoff, F. Mauri, and E. Arimondo, "Transient velocity-selective coherent population trapping in one dimension," *J. Opt. Soc. Am. B*, vol. 9, no. 3, pp. 321–331, 1992. (cited on p. 53)

[117] A. Aspect, E. Arimondo, R. Kaiser, N. Vansteenkiste, and C. Cohen-Tannoudji, "Laser cooling below the one-photon recoil energy by velocity-selective coherent population trapping," *Phys. Rev. Lett.*, vol. 61, pp. 826–829, 1988. (cited on p. 54)

[118] M. S. Shahriar, P. R. Hemmer, M. G. Prentiss, P. Marte, J. Mervis, D. P. Katz, N. P. Bigelow, and T. Cai, "Continuous polarization-gradient precooling-assisted velocity-selective coherent population trapping," *Phys. Rev. A*, vol. 48, pp. R4035–R4038, 1993. (cited on p. 54)

[119] G. Grynberg and J.-Y. Courtois, "Proposal for a magneto-optical lattice for trapping atoms in nearly-dark states," *EPL (Europhysics Letters)*, vol. 27, no. 1, p. 41, 1994. (cited on p. 54)

[120] M. Weidemüller, T. Esslinger, M. A. Ol'shanii, A. Hemmerich, and T. W. Hänsch, "A novel scheme for efficient cooling below the photon recoil limit," *EPL (Europhysics Letters)*, vol. 27, no. 2, p. 109, 1994. (cited on p. 54)

[121] K. I. Petsas, J.-Y. Courtois, and G. Grynberg, "Temperature and magnetism of gray optical lattices," *Phys. Rev. A*, vol. 53, pp. 2533–2538, 1996. (cited on p. 54)

[122] A. Hemmerich, M. Weidemüller, T. Esslinger, C. Zimmermann, and T. Hänsch, "Trapping atoms in a dark optical lattice," *Phys. Rev. Lett.*, vol. 75, pp. 37–40, 1995. (cited on pp. 54 and 55)

[123] C. Valentin, M.-C. Gagné, J. Yu, and P. Pillet, "One-dimension sub-Doppler molasses in the presence of static magnetic field," *EPL (Europhysics Letters)*, vol. 17, no. 2, p. 133, 1992. (cited on p. 55)

[124] D. Boiron, C. Triché, D. R. Meacher, P. Verkerk, and G. Grynberg, "Three-dimensional cooling of cesium atoms in four-beam gray optical molasses," *Phys. Rev. A*, vol. 52, pp. R3425–R3428, 1995. (cited on p. 55)

[125] D. Boiron, A. Michaud, P. Lemonde, Y. Castin, C. Salomon, S. Weyers, K. Szymaniec, L. Cognet, and A. Clairon, "Laser cooling of cesium atoms in gray optical molasses down to 1.1 μK," *Phys. Rev. A*, vol. 53, pp. R3734–R3737, 1996. (cited on pp. 55 and 62)

[126] C. Triché, P. Verkerk, and G. Grynberg, "Blue-sisyphus cooling in cesium gray molasses and antidot lattices," *Eur. Phys. J. D*, vol. 5, no. 2, pp. 225–228, 1999. (cited on pp. 55 and 61)

[127] T. Esslinger, H. Ritsch, M. Weidemüller, F. Sander, A. Hemmerich, and T. W. Hänsch, "Purely optical dark lattice," *Opt. Lett.*, vol. 21, no. 13, pp. 991–993, 1996. (cited on p. 55)

[128] S. Rosi, A. Burchianti, S. Conclave, D. S. Naik, G. Roati, C. Fort, and F. Minardi, "Λ-enhanced grey molasses on the D_2 transition of Rubidium-87 atoms," *ArXiv e-prints*, 2017. (cited on pp. 55, 60, and 61)

[129] M. Drewsen, U. Drodofsky, C. Weber, G. Schreiber, and J. Mlynek, "Sisyphus polarization gradient laser cooling of Cr atoms on the J = 3, J'= 2 , 3 and 4 transitions," *Journal of Physics B: Atomic, Molecular and Optical Physics*, vol. 29, no. 23, p. L843, 1996. (cited on p. 55)

[130] H. Stecher, H. Ritsch, P. Zoller, F. Sander, T. Esslinger, and T. W. Hänsch, "All-optical gray lattice for atoms," *Phys. Rev. A*, vol. 55, pp. 545–551, 1997. (cited on p. 55)

[131] V. Elman and A. Hemmerich, "Near-resonant dark optical lattice with increased occupation," *Phys. Rev. A*, vol. 72, p. 043410, 2005. (cited on pp. 55 and 61)

[132] D. R. Fernandes, F. Sievers, N. Kretzschmar, S. Wu, C. Salomon, and F. Chevy, "Sub-doppler laser cooling of fermionic 40 K atoms in three-dimensional gray optical molasses," *EPL (Europhysics Letters)*, vol. 100, no. 6, p. 63001, 2012. (cited on p. 55)

[133] F. Sievers, N. Kretzschmar, D. R. Fernandes, D. Suchet, M. Rabinovic, S. Wu, C. V. Parker, L. Khaykovich, C. Salomon, and F. Chevy, "Simultaneous sub-Doppler laser cooling of fermionic ^{6}Li and ^{40}K on the D_1 line: Theory and experiment," *Phys. Rev. A*, vol. 91, p. 023426, 2015. (cited on pp. 55, 60, 61, and 62)

[134] A. T. Grier, I. Ferrier-Barbut, B. S. Rem, M. Delehaye, L. Khaykovich, F. Chevy, and C. Salomon, "Λ-enhanced sub-Doppler cooling of lithium atoms in D_1 gray molasses," *Phys. Rev. A*, vol. 87, p. 063411, 2013. (cited on pp. 55 and 60)

[135] G. Salomon, L. Fouché, P. Wang, A. Aspect, P. Bouyer, and T. Bourdel, "Gray-molasses cooling of ^{39} K to a high phase-space density," *EPL (Europhysics Letters)*, vol. 104, no. 6, p. 63002, 2013. (cited on pp. 55, 61, and 67)

[136] D. Nath, R. K. Easwaran, G. Rajalakshmi, and C. S. Unnikrishnan, "Quantum-interference-enhanced deep sub-Doppler cooling of ^{39}K atoms in gray molasses," *Phys. Rev. A*, vol. 88, p. 053407, 2013. (cited on pp. 55 and 60)

[137] A. Burchianti, G. Valtolina, J. A. Seman, E. Pace, M. De Pas, M. Inguscio, M. Zaccanti, and G. Roati, "Efficient all-optical production of large ^{6}Li quantum gases using D_1 gray-molasses cooling," *Phys. Rev. A*, vol. 90, p. 043408, 2014. (cited on p. 55)

[138] Q. Bouton, R. Chang, A. L. Hoendervanger, F. Nogrette, A. Aspect, C. I. Westbrook, and D. Clément, "Fast production of Bose-Einstein condensates of metastable helium," *Phys. Rev. A*, vol. 91, p. 061402, 2015. (cited on pp. 55 and 67)

[139] W. D. H. Janik, G.; Nagourney, "Doppler-free optical spectroscopy on the ba+ mono-ion oscillator," *Journal of the Optical Society of America B*, vol. 2, 1985. (cited on p. 60)

[140] U. Fano, "Effects of configuration interaction on intensities and phase shifts," *Phys. Rev.*, vol. 124, pp. 1866–1878, 1961. (cited on p. 60)

[141] B. Lounis and C. Cohen-Tannoudji, "Coherent population trapping and Fano profiles," *J. Phys. II France*, vol. 2, no. 4, pp. 579–592, 1992. (cited on p. 60)

[142] T. Kinoshita, T. Wenger, and D. S. Weiss, "All-optical Bose-Einstein condensation using a compressible crossed dipole trap," *Phys. Rev. A*, vol. 71, p. 011602, 2005. (cited on pp. 67 and 68)

[143] J.-F. Clément, J.-P. Brantut, M. Robert-de Saint-Vincent, R. A. Nyman, A. Aspect, T. Bourdel, and P. Bouyer, "All-optical runaway evaporation to Bose-Einstein condensation," *Phys. Rev. A*, vol. 79, p. 061406, 2009. (cited on pp. 67, 69, and 86)

[144] K. B. Davis, M. O. Mewes, M. R. Andrews, N. J. van Druten, D. S. Durfee, D. M. Kurn, and W. Ketterle, "Bose-Einstein condensation in a gas of sodium atoms," *Phys. Rev. Lett.*, vol. 75, pp. 3969–3973, 1995. (cited on p. 67)

[145] W. Petrich, M. H. Anderson, J. R. Ensher, and E. A. Cornell, "Stable, tightly confining magnetic trap for evaporative cooling of neutral atoms," *Phys. Rev. Lett.*, vol. 74, pp. 3352–3355, 1995. (cited on p. 67)

[146] Y.-J. Lin, A. R. Perry, R. L. Compton, I. B. Spielman, and J. V. Porto, "Rapid production of ^{87}Rb Bose-Einstein condensates in a combined magnetic and optical potential," *Phys. Rev. A*, vol. 79, p. 063631, 2009. (cited on p. 67)

[147] A. S. Flores, H. P. Mishra, W. Vassen, and S. Knoop, "Simple method for producing Bose–Einstein condensates of metastable helium using a single-beam optical dipole trap," *Applied Physics B*, vol. 121, no. 3, pp. 391–399, 2015. (cited on p. 67)

[148] M.-S. Heo, J.-y. Choi, and Y.-i. Shin, "Fast production of large ^{23}Na Bose-Einstein condensates in an optically plugged magnetic quadrupole trap," *Phys. Rev. A*, vol. 83, p. 013622, 2011. (cited on p. 67)

[149] J. P. Brantut, J. F. Clément, M. R. de Saint Vincent, G. Varoquaux, R. A. Nyman, A. Aspect, T. Bourdel, and P. Bouyer, "Light-shift tomography in an optical-dipole trap for neutral atoms," *Phys. Rev. A*, vol. 78, p. 031401, 2008. (cited on p. 69)

[150] W. Wiese, M. W. Smith, and B. M. Miles, *Atomic transition probabilities. Vol. 2: Sodium through Calcium. A critical data compilation.* 1969. (cited on p. 70)

[151] D. A. Steck, "Sodium d line data," *Report, Los Alamos National Laboratory, Los Alamos*, vol. 124, 2000. (cited on p. 74)

[152] S. Stringari, "Collective excitations of a trapped Bose-condensed gas," *Phys. Rev. Lett.*, vol. 77, pp. 2360–2363, Sep 1996. (cited on p. 77)

[153] D. M. Stamper-Kurn, H.-J. Miesner, A. P. Chikkatur, S. Inouye, J. Stenger, and W. Ketterle, "Reversible formation of a Bose-Einstein condensate," *Phys. Rev. Lett.*, vol. 81, pp. 2194–2197, 1998. (cited on pp. 83 and 88)

[154] D. Comparat, A. Fioretti, G. Stern, E. Dimova, B. L. Tolra, and P. Pillet, "Optimized production of large Bose-Einstein condensates," *Phys. Rev. A*, vol. 73, p. 043410, 2006. (cited on pp. 83 and 86)

[155] W. Ketterle and N. van Druten, "Evaporative cooling of atoms," *Advances in Atomic, Molecular, and Optical Physics, edited by B. Bederson and H. Walther*, vol. 37, pp. 181–236, 1996. (cited on pp. 84 and 86)

[156] K. M. O'Hara, M. E. Gehm, S. R. Granade, and J. E. Thomas, "Scaling laws for evaporative cooling in time-dependent optical traps," *Phys. Rev. A*, vol. 64, p. 051403, 2001. (cited on pp. 85 and 86)

[157] A. J. Olson, R. J. Niffenegger, and Y. P. Chen, "Optimizing the efficiency of evaporative cooling in optical dipole traps," *Phys. Rev. A*, vol. 87, p. 053613, May 2013. (cited on p. 86)

[158] D. Heinzen, "Ultracold atomic interactions," in *Proceedings of the International School of Physics-Enrico Fermi*, p. 351, 1999. (cited on p. 86)